

Small-scale encapsulation method for novel drug substances with associated characterization of highly diluted samples

Dissertation

zur Erlangung des Grades
des Doktors der Naturwissenschaften
der Naturwissenschaftlich-Technischen Fakultät
der Universität des Saarlandes

von

Johannes Clemens Büscher

Saarbrücken

2023

Tag des Kolloquiums: 10. November 2023

Dekan: Prof. Dr. Ludger Santen

Berichterstatter: Prof. Dr. Marc Schneider
Prof. Dr. Tobias Kraus

Vorsitz: Prof. Dr. Guido Kickelbick

Akad. Mitarbeiter: Dr. Stefan Boettcher

Die Daten der vorliegenden Dissertation sind im Zeitraum zwischen Januar 2019 und Dezember 2022 am Institut für Biopharmazie und Pharmazeutische Technologie der Universität des Saarlandes unter der Betreuung von Prof. Dr. Marc Schneider (Professor für Biopharmazie und Pharmazeutische Technologie) entstanden.

*In gratefulness and loving memory dedicated to
Jupp Hoppe.*

I. Table of contents

I. Table of contents	- 1 -
II. Abbreviations	- 3 -
III. Summary.....	- 5 -
IV. Zusammenfassung.....	- 6 -
Chapter 1 – General introduction	- 7 -
1.1 Drug delivery	- 8 -
1.2 Novel drug substances and their challenges	- 8 -
1.3 Enhancing bioavailability by formulation development	- 9 -
1.4 Downscaling	- 11 -
1.5 Analytics of highly diluted samples	- 12 -
1.6 Aim of the work.....	- 13 -
1.7 References.....	- 14 -
Chapter 2 – Frequently used methods.....	- 17 -
2.1 Methods	- 18 -
2.1.1 Dynamic light scattering (DLS).....	- 18 -
2.1.2 Zeta potential measurement and laser-doppler anemometry	- 19 -
2.1.3 Lyophilization	- 20 -
2.1.4 Scanning electron microscopy (SEM)	- 21 -
2.1.5 Transmission electron microscopy (TEM)	- 21 -
2.2 References.....	- 22 -
Chapter 3 – Particle formulation	- 24 -
3.1 Introduction: Particle formulation	- 25 -
3.2 Materials.....	- 26 -
3.3 Microfluidic particle formulation	- 27 -
3.3.1 Initial microfluidic setup.....	- 27 -
3.3.1.1 Methods	- 27 -
3.3.1.2 Results and discussion.....	- 30 -
3.3.2 Improved microfluidic setup	- 33 -
3.3.2.1 Methods	- 33 -
3.3.2.2 Results and discussion.....	- 44 -
3.3.3 Further manufactured particle systems based on different polymers using the improved setup.....	- 50 -

3.3.3.1 Methods	- 50 -
3.3.3.2 Results and discussion	- 53 -
3.4 References.....	- 59 -
Chapter 4 – Parameters influencing drug encapsulation	- 62 -
4.1 Introduction: Parameters influencing drug encapsulation	- 63 -
4.2 Materials.....	- 65 -
4.3 Model particle system for optimization studies.....	- 66 -
4.3.1 Particle preparation.....	- 66 -
4.3.1.1 Methods	- 66 -
4.3.1.2 Results and discussion.....	- 68 -
4.3.2 Influence of the stabilizer on the encapsulation efficiency	- 70 -
4.3.2.1 Methods	- 70 -
4.3.2.2 Results and discussion.....	- 77 -
4.4 References.....	- 88 -
Chapter 5 – Particle quantification.....	- 91 -
5.1 Introduction: Particle quantification	- 92 -
5.2 Materials.....	- 94 -
5.3 Particle quantification	- 95 -
5.3.1 Fluorescence microscopy	- 95 -
5.3.1.1 Methods	- 95 -
5.3.1.2 Results and discussion.....	- 111 -
5.3.2 Dark-field microscopy.....	- 120 -
5.3.2.1 Methods	- 120 -
5.3.2.2 Results and discussion.....	- 123 -
5.4 References.....	- 126 -
Chapter 6 – Summary and outlook	- 131 -
6.1 Particle preparation.....	- 132 -
6.2 Improvement of drug loading	- 133 -
6.3 Particle quantification	- 134 -
6.4 References.....	- 135 -
Publication report.....	- 137 -
Acknowledgements	- 138 -
Curriculum vitae	- 139 -

II. Abbreviations

AFM	Atomic force microscopy
ALMA	Allyl methacrylate
ANOVA	Analysis of variance
AUC	Analytical ultracentrifugation
BCS	Biopharmaceutical classification system
CMC	Critical micelle concentration
DCM	Dichloromethane
DEAE	Diethylaminoethyl
DLS	Dynamic light scattering
DM	Dichroic mirror
DNA	Deoxyribonucleic acid
dsRNA	Double-stranded ribonucleic acid
<i>E. coli</i>	<i>Escherichia coli</i>
EmF	Emission filter
ExF	Excitation filter
FITC	Fluorescein isothiocyanate
GP	Gas pycnometry
HLB	Hydrophilic lipophilic balance
LED	Light-emitting diode
MADLS	Multi angle dynamic light scattering
MEK	Methyl ethyl ketone
MMA	Methyl methacrylate
MWCO	Molecular weight cut-off
NA	Numerical aperture
NaDS	Sodium disulfite
NaPS	Sodium persulfate
NTA	Nanoparticle tracking analysis
PBS	Phosphate-buffered saline

PDI	Polydispersity index
PDMS	Polydimethylsiloxane
PLGA	Poly(lactic-co-glycolic acid)
PMMA	Poly(methyl methacrylate)
PVA	Polyvinyl alcohol
PVS	Pressure & vacuum source
P ² CS	Precision pressure control system
RhBMA	Rhodamine B methacrylamide
RNA	Ribonucleic acid
SD	Standard deviation
SDS	Sodium dodecyl sulfate
SEM	Scanning electron microscopy
SPT	Single-particle tracking
TEM	Transmission electron microscopy
TRPS	Tunable resistive pulse sensing

III. Summary

One of the biggest challenges in the development of novel active ingredients is the lack of available drug substances in early stages of development. Nevertheless, in many cases an early decision must be made whether the active ingredient can be delivered to the desired site of action by a suitable carrier system or not. Therefore, it is desirable to manufacture carrier systems in a very small scale avoiding unnecessary material waste. Following this idea, polymer-based nanoparticles were manufactured acting as drug carriers. They were produced using a microfluidic system to keep the required quantities of utilized substances as small as possible. The microfluidic system was especially designed for this application controlling the respective volumetric flow rates of the used liquids by applying air pressure. This allows to tune the desired microfluidic mixing ratio very precisely without any time delay. In addition, the drug loading of produced particles was optimized, with particular attention paid to the type and concentration of utilized stabilizers. By specific adjustments to the mentioned factors, the drug loading could be maximized. Furthermore, particle concentrations of the prepared suspensions were investigated. For this purpose, a microfluidic device was developed precisely determining the number of particles contained by the produced and highly diluted nanosuspensions.

IV. Zusammenfassung

Eines der größten Probleme bei der Etablierung von neuartigen Wirkstoffen ist der Mangel an verfügbareren Substanzen in frühen Entwicklungsabschnitten. Da dennoch häufig in Frühphasen der Entwicklung eine Entscheidung gefällt werden muss, ob sich der Wirkstoff mit Hilfe eines geeigneten Trägersystems an den gewünschten Wirkort transportieren lässt, ist es wünschenswert Trägersysteme im Kleinmaßstab herzustellen. Hierzu wurden polymerbasierte Nanopartikel als Wirkstoffträger verwendet, welche mittels eines mikrofluidischen Systems hergestellt wurden, um die einzusetzenden Substanzmengen so gering wie möglich zu halten. Das dazu verwendete mikrofluidische System wurde speziell für diesen Einsatz entworfen und ist luftdruckgetrieben, wodurch die jeweiligen Volumenströme der verwendeten Flüssigkeiten gesteuert werden. Dadurch kann sehr präzise und ohne zeitliche Verzögerung ein gewünschtes mikrofluidisches Mischungsverhältnis erreicht werden. Außerdem wurde für die hergestellten Partikel die Wirkstoffbeladung optimiert, wobei ein besonderes Augenmerk auf den Typ und die Konzentration der verwendeten Stabilisatoren gelegt wurde. Durch gezielte Anpassungen konnte die Wirkstoffbeladung maximiert werden. Des Weiteren wurden die hergestellten Suspensionen bezüglich ihrer Partikelkonzentration untersucht. Hierfür wurde ein mikrofluidisches Element entwickelt, mit dem sich gerade bei hochverdünnten Nanosuspensionen die Anzahl an enthaltenen Partikeln präzise ermitteln lässt.

Chapter 1

General introduction

1.1 Drug delivery

Administration of drug substances to the human or animal body can be more challenging than assumed. Drug delivery describes in this context the transfer of the drug from the outside of the body to its site of action. This site of action can either be located inside of the body or on surface areas [1–3]. A desired way to reach the highest pharmacodynamic efficacy would be to apply the respective drug directly to its target site [4]. A local and precise administration would mimic the physiological actions of the body where endogenous substances are released in very limited areas and create a direct effect on the surrounding tissues. Since accessibility of those sites is often limited by physiological factors (locations difficult to reach manually) or the influence of different pharmacokinetic aspects an alternative strategy must be considered. In comparison to a local administration which would guarantee an application directly to the site of action a systemic administration sometimes is inevitable.

The simplest imaginable way for a systemic drug delivery would be an oral administration of the pure drug substance. If the substance is absorbed during the passage of the gastrointestinal tract it is distributed in the entire body depending on the physicochemical properties of the substance and accompanying the accessibility of respective body compartments. Since ingesting of pure powder orally complicates handling and bears the risk of dosing mistakes drug substances are preferably administered using tablets or capsules via the identical route. Furthermore, those delivery systems can be tuned regarding their dissolution behavior, for instance enteric coating or coatings for sustained release [5]. In addition to the oral application route a systemic drug delivery can be achieved by inhalation [1,5], rectal application [6], or parenteral application (e.g., injections into the venous system or into tissues like subcutis or muscle [7]). Especially for parenteral application the drug release from the application site into the systemic circulation can be highly influenced by the delivery system. An injected dissolved drug substance leads to a fast distribution whereas a polymer-based implant releasing an incorporated drug substance via diffusion leads to a slow distribution [5]. The selection of the respective delivery system is often guided by the drug substance itself. Here hydrophilicity or lipophilicity and the desired distribution speed are crucial in the selection of an adequate delivery system [5].

1.2 Novel drug substances and their challenges

The research for novel drug substances, either small or large molecules, raises problems of different kinds. Focusing on small molecules, most of them show poor water solubility [8,9] no matter if they are of a synthetic or semi-synthetic origin. This becomes clear having in mind how modern research for active ingredients works. The desired approach includes identifying a certain binding site (e.g., binding pockets of enzymes) and to design a molecule which interacts in the intended way with this specific binding site [8]. Many targeted bindings sites feature very lipophilic

environments for respective substances. Consequently, the active ingredients must match these lipophilic properties for an effective interaction [8].

Due to high lipophilicity a poor water solubility results for many new developed substances. To guarantee a successful drug delivery, carrier systems must be developed to transport these substances into the body and effectively release them into the systemic circulation or the desired site of action. The most critical factors are water solubility and dissolution speed [5]. Without a proper dissolution in the aqueous environment of application sites like the gastrointestinal tract or the injection site, drug substances are hindered to reach their target and cannot fulfill their task. Consequently, drug delivery must provide systems which are available to reduce this problem to a minimum.

Focusing on large molecules represented mostly by peptides or nucleic acids, oral bioavailability is highly limited. Digestive enzymes degrade those molecules during the gastrointestinal passage in high numbers making an effective treatment challenging. Furthermore, due to molecular size the permeation through the intestinal mucosa is limited. To avoid these drawbacks a parenteral application appears more suitable for molecules from this group. Nevertheless, especially nucleic acids like deoxyribonucleic acid (DNA) and ribonucleic acid (RNA) often must reach intracellular targets for silencing other RNAs or delivering their genetic information and transferring it into the desired protein [10,11]. In this case a drug delivery system would be required carrying a highly hydrophilic molecule as DNA or RNA over lipophilic cell membranes and releasing it inside of the cell [11].

Another large problem regarding new developed drug substances is the lack of available substance in early stages of development. Due to this fact, it is not possible to use larger amounts of substances for first formulation experiments. Often, drug substances are vastly expensive according to their small yields in new developed production strains, and especially this fact limits the flexibility in formulation development drastically. Still, it can be necessary to get early information if the chosen drug substance can be delivered to the desired target or not. Concluding, an early formulation development which reduces the required amounts for manufacturing the intended drug delivery system is highly desirable.

1.3 Enhancing bioavailability by formulation development

As mentioned earlier solubility in the gastrointestinal tract and permeability across the intestinal mucosa are important factors characterizing orally administered drug substances. To classify this group of substances the Biopharmaceutical Classification System (BCS) was established. It incorporates four groups (I, II, III, and IV) which are displayed below in Fig. 1.1 [12,13]:

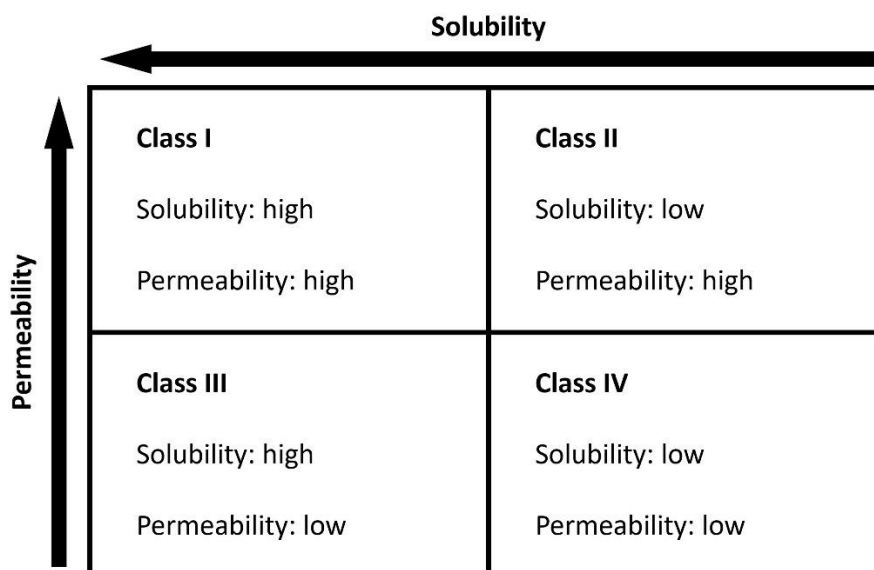


Fig. 1.1. BCS classes and their characteristics.

Class I would be the desired classification for an orally administered active ingredient. High aqueous solubility and intestinal permeability simplify an absorption via this route vastly. Consequently, regarding drug delivery it is the quest to push substances ranked in the remaining classes towards class I by manufacturing superior drug formulations.

To minimize the drawback of low water solubility a popular strategy is to enlarge the surface area of the drug particles. This leads to a higher dissolution speed and a faster drug availability if the substance is removed from the dissolution site quickly. A fast drug removal from the dissolution site is obligatory to prevent reaching the saturation concentration immediately. The higher dissolution speed caused by enlarging the surface area can be explained by the Noyes-Whitney equation [5,14]:

$$\frac{dM}{dt} = \frac{D * A}{h} * (c_s - c_t)$$

Where dM/dt is the dissolution speed (dissolved mass over time), D is the diffusion coefficient of the substance molecules, A is the surface of the substance accessible for the solvent, h is the thickness of the diffusion layer around the solid substance, and c_s and c_t are the saturation concentration and the concentration at a given time in the solvent [5,14].

By reducing the diameter of drug substance particles, the total surface of the substance is increasing which increases the dissolution speed according to Noyes-Whitney.

Additionally, by reducing the particle diameter the saturation concentration is increasing. This behavior can be explained by the modified Kelvin equation, which shows that the particle radius has a direct effect on the saturation concentration [15]:

$$\ln \frac{c_r}{c_s} = \frac{2\gamma V_m}{rRT}$$

Where c_r is the saturation concentration of a substance at a given radius, c_s is the saturation concentration of the same substance at a plane surface, γ is the interfacial tension between the particle to be solved and the solvent, V_m is the molar volume of the dissolved substance, r is the particle radius, R is the gas constant, and T is the absolute temperature [15].

By introducing nanoformulations (major reduction of the particle diameter) both dissolution speed and saturation concentration can be maximized. An option to produce nanoparticles would be to grind pure drug substance particles till they reach a size of a few hundred nanometers [16]. As an alternative, polymer-based nanoparticles can be utilized as carrier systems. By loading drug substance on the particle surfaces via van der Waals or electrostatic interactions substance exposure to the solvent could be increased and with this the dissolution speed [17–19].

Active ingredients showing poor intestinal permeability / oral bioavailability but still being hydrophilic enough for dissolution in aqueous media (e.g., peptides or nucleic acids) can be delivered using polymer-based nanoparticles as well. Especially, by evading to a parenteral drug administration, nanoparticles are applicable. Regarding nucleic acids it can be highly beneficial to incorporate the genetic information into a nanoparticle and to use this particle as a carrier into the respective cell [11,20]. Furthermore, RNA or DNA degradation can be avoided at the application site using a system like this [11,20]. Another scope of application for polymer-based nanoparticles regarding water soluble drugs with low oral bioavailability can be a sustained release drug delivery system [17,18,21]. Here the release rate is depending on the substance solubility in the polymer. The higher the solubility of the active ingredient in the polymer, the slower it will diffuse out of it and the slower the release will be. This behavior will lead to a more sustained release profile. Furthermore, it can be modulated by choosing biodegradable polymers. By the degradation rate and the resulting erosion of the polymer / particle the release rate can be increased if necessary [17,21]. Concluding, the introduced polymer-based formulation strategies represent highly suitable formulations for generating a depot inside of the body.

1.4 Downscaling

Confronting the issue of reduced amounts of available drug substances in early stages of development but still having the need for first formulation experiments, a downscaling of production processes is necessary. By reducing the required amounts of substances to a minimum a microfluidic approach was selected to manufacture the desired drug delivery systems. Batch sizes were reduced to fractions of milligrams enabling a screening for suitable formulation types and strategies without wasting large amounts of expensive drug candidates.

Produced and downscaled drug delivery systems were based on polymeric nanoparticles. Utilizing a microfluidic mixing device, nanoprecipitation was exploited

for producing the mentioned particles [22,23]. Due to nanoprecipitation being a rapid process (driven in this study by mixing of multiple solvents or salt formation) particle manufacturing can be influenced effectively by tuning the mixing conditions inside of the device. An initial microfluidic setup relying on syringe pumps was upgraded to a system relying on air pressure. This improved microfluidic system was designed for an even higher precision in mixing of different solvents for maximum control over the precipitation process.

Produced polymer-based nanoparticles should act as carriers for respective active ingredients. By producing batches of minimal size (few microliters), different formulation candidates should be characterized and evaluated. Following this approach, a promising candidate can be detected in a cost-efficient way and consequently transferred to an upscaled process if necessary.

1.5 Analytics of highly diluted samples

The mentioned formulation candidates consisting of microfluidic produced nanosuspensions occur in small volumes and very low particle concentrations. Therefore, gravimetric measurements focusing on the particle yield are challenging to carry out. Characterizing dried particle masses of about 100 ng and lower by utilizing an appropriate balance requires a significant preparative effort and bears a high error rate as well.

Concluding, an alternative and straightforward characterization method is desirable. Counting of particles is easier to facilitate in the mentioned low concentrations compared to a gravimetric measurement. Consequently, a method for the quantification of particles in real numbers was investigated. This developed method is based on single-particle tracking [24–26]. A microfluidic device made of polydimethylsiloxane (PDMS) was designed for this purpose. Particles should be detected and counted inside of a microfluidic channel with well-known channel dimensions (see Fig. 1.2). By calculating a precise volume of the visualized channel area an average number concentration of visualized particles should be obtained. This approach is straightforward compared to nanoparticle quantification alternatives like multi angle dynamic light scattering (MADLS) [27,28], tunable resistive pulse sensing (TRPS) [29–31], or nanoparticle tracking analysis (NTA) [32,33] and is intended to provide an even higher precision for highly diluted samples. Obtained particle number concentrations combined with measured particle sizes can be utilized for characterizing the different manufactured and highly diluted nanosuspensions in a simple and reliable way.

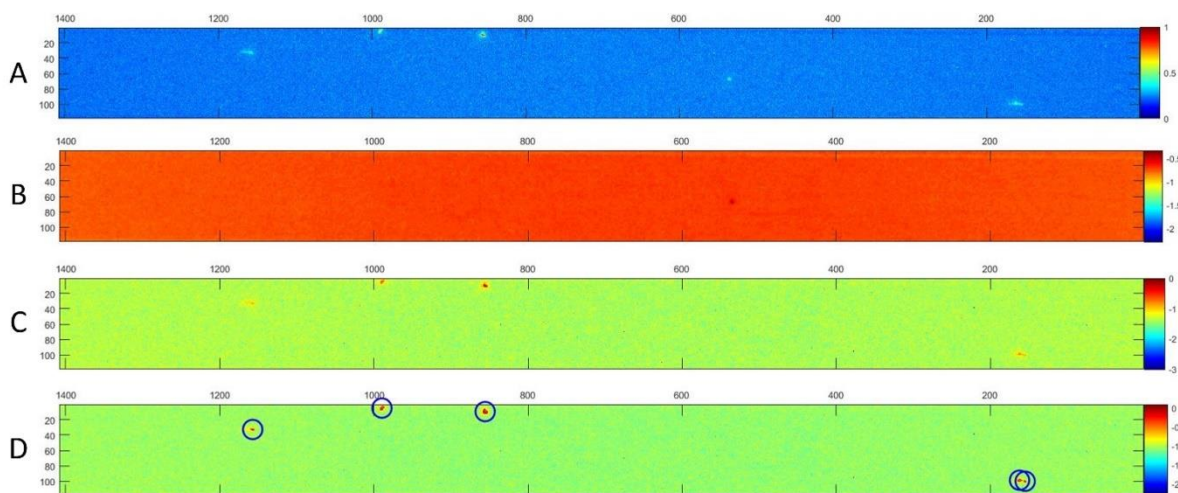


Fig. 1.2. A) Original captured image of particles translated into an intensity distribution of the respective image. B) Image background calculated from a series of captured images. C) Intensity signals from particles after background subtraction. D) Detected particle signals (marked with blue circles) standing out above an intensity threshold. Nonmoving particles / objects are excluded from the detection and are included in the image background (e.g., bright object in image A between pixels 600 and 400 (horizontal axis)).

1.6 Aim of the work

The aim of this thesis is to establish a microfluidic nanoparticle production process which provides a maximum in precision when it comes to particle precipitation and drug loading. This developed microfluidic setup should be able to produce mentioned particles in volumes of few microliters avoiding an unnecessary waste of expensive drug substances. Additionally, it should act as a versatile manufacturing platform being capable of nanoparticle production including a large variety of particle materials. Both very hydrophilic and very lipophilic polymers are to be utilized as particle materials (e.g., hydrophilic: gelatin and different dextrans; lipophilic: poly(lactic-co-glycolic acid) (PLGA)) which should underline the flexibility of the production system. These downscaled formulation experiments should give first impressions about suitable formulations for respective drug substances in early development stages.

Furthermore, drug loading on polymer-based nanoparticles should be investigated. Observations revealed that different types of stabilizers (molecules assembling on particle surfaces to reduce particle aggregation) and respective stabilizer concentrations in the nanosuspension influence the drug loading on produced particles. High stabilizer concentrations resulted in a decrease in drug loading, whereas low concentrations did not appear to affect the loading. Curcumin is intended to act as a model substance for drug loading experiments. A series of formulation experiments including different stabilizer types and stabilizer concentrations should provide precise information about a concentration dependency on the decrease in curcumin loading. Obtained data should be utilized for optimizing the microfluidic production process.

In addition, the produced and highly diluted nanosuspensions should be analyzed regarding their particle concentration in absolute numbers as previously mentioned. As quantification method a novel approach relying on single-particle tracking should be established. An analytical method like this is intended to provide a simple, reliable, and straightforward measurement delivering high precision in particle concentration determination and low costs in analytical effort.

1.7 References

- [1] G. Tiwari, R. Tiwari, B. Sriwastawa, L. Bhati, S. Pandey, P. Pandey, S.K. Bannerjee, Drug delivery systems: An updated review, *Int J Pharm Investig.* 2 (2012) 2–12. <https://doi.org/10.4103/2230-973X.96920>.
- [2] M.S. Alqahtani, M. Kazi, M.A. Alsenaidy, M.Z. Ahmad, *Advances in Oral Drug Delivery*, *Front Pharmacol.* 12 (2021) 62. <https://doi.org/10.3389/FPHAR.2021.618411>.
- [3] A.M. Vargason, A.C. Anselmo, S. Mitragotri, The evolution of commercial drug delivery technologies, *Nat Biomed Eng.* 5 (2021) 951–967. <https://doi.org/10.1038/s41551-021-00698-w>.
- [4] H. Wen, H. Jung, X. Li, Drug Delivery Approaches in Addressing Clinical Pharmacology-Related Issues: Opportunities and Challenges, *AAPS J.* 17 (2015) 1327–1340. <https://doi.org/10.1208/S12248-015-9814-9>.
- [5] A. Fahr, *Voigt Pharmazeutische Technologie*, Voigt Pharmazeutische Technologie. (2022). <https://doi.org/10.52777/9783769277487>.
- [6] T.J. Purohit, S.M. Hanning, Z. Wu, *Advances in rectal drug delivery systems*, *Pharm Dev Technol.* 23 (2018) 942–952. <https://doi.org/10.1080/10837450.2018.1484766>.
- [7] N. Gulati, H. Gupta, Parenteral Drug Delivery: A Review, *Recent Pat Drug Deliv Formul.* 5 (2011) 133–145. <https://doi.org/10.2174/187221111795471391>.
- [8] C.J.H. Porter, N.L. Trevaskis, W.N. Charman, Lipids and lipid-based formulations: optimizing the oral delivery of lipophilic drugs, *Nat Rev Drug Discov.* 6 (2007) 231–248. <https://doi.org/10.1038/nrd2197>.
- [9] K.T. Savjani, A.K. Gajjar, J.K. Savjani, Drug Solubility: Importance and Enhancement Techniques, *ISRN Pharm.* 2012 (2012) 1–10. <https://doi.org/10.5402/2012/195727>.
- [10] D. Baulcombe, RNA silencing, *Trends Biochem Sci.* 30 (2005) 290–293. <https://doi.org/10.1016/j.tibs.2005.04.012>.
- [11] J. Zhao, S. Zhao, J. Ou, J. Zhang, W. Lan, W. Guan, X. Wu, Y. Yan, W. Zhao, J. Wu, J. Chodosh, Q. Zhang, COVID-19: Coronavirus Vaccine Development Updates, *Front Immunol.* 11 (2020) 3435. <https://doi.org/10.3389/FIMMU.2020.602256>.
- [12] J. Cook, W. Addicks, Y.H. Wu, Application of the biopharmaceutical classification system in clinical drug development - An industrial view, *AAPS Journal.* 10 (2008) 306–310. <https://doi.org/10.1208/S12248-008-9036-5>.
- [13] J.E. Polli, B.S. Abrahamsson, M.S. Ku, Use of the Biopharmaceutical Classification System in Early Drug Development, *The AAPS Journal.* 10 (2008) 208–212. <https://doi.org/10.1208/S12248-008-9020-0>.

- [14] A.A. Noyes, W.R. Whitney, The rate of solution of solid substances in their own solutions, *J Am Chem Soc.* 19 (1897) 930–934. <https://doi.org/10.1021/JA02086A003>.
- [15] T. Tadros, Kelvin Equation, *Encyclopedia of Colloid and Interface Science.* (2013) 679–680. https://doi.org/10.1007/978-3-642-20665-8_112.
- [16] L. Peltonen, J. Hirvonen, Pharmaceutical nanocrystals by nanomilling: critical process parameters, particle fracturing and stabilization methods, *Journal of Pharmacy and Pharmacology.* 62 (2010) 1569–1579. <https://doi.org/10.1111/J.2042-7158.2010.01022.X>.
- [17] H.K. Makadia, S.J. Siegel, Poly Lactic-co-Glycolic Acid (PLGA) as biodegradable controlled drug delivery carrier, *Polymers.* 3 (2011) 1377–1397. <https://doi.org/10.3390/polym3031377>.
- [18] D. Bobo, K.J. Robinson, J. Islam, K.J. Thurecht, S.R. Corrie, Nanoparticle-Based Medicines: A Review of FDA-Approved Materials and Clinical Trials to Date, *Pharm Res.* 33 (2016) 2373–2387. <https://doi.org/10.1007/s11095-016-1958-5>.
- [19] B. Begines, T. Ortiz, M. Pérez-Aranda, G. Martínez, M. Merinero, F. Argüelles-Arias, A. Alcudia, Polymeric Nanoparticles for Drug Delivery: Recent Developments and Future Prospects, *Nanomaterials.* 10 (2020) 1403. <https://doi.org/10.3390/NANO10071403>.
- [20] B.N. Aldosari, I.M. Alfagih, A.S. Almurshedi, Lipid Nanoparticles as Delivery Systems for RNA-Based Vaccines, *Pharmaceutics.* 13 (2021) 206. <https://doi.org/10.3390/PHARMACEUTICS13020206>.
- [21] F.Y. Han, K.J. Thurecht, A.K. Whittaker, M.T. Smith, Bioerodable PLGA-based microparticles for producing sustained-release drug formulations and strategies for improving drug loading, *Front Pharmacol.* 7 (2016) 185. <https://doi.org/10.3389/FPHAR.2016.00185>.
- [22] C.J. Martínez Rivas, M. Tarhini, W. Badri, K. Miladi, H. Greige-Gerges, Q.A. Nazari, S.A. Galindo Rodríguez, R.Á. Román, H. Fessi, A. Elaissari, Nanoprecipitation process: From encapsulation to drug delivery, *Int J Pharm.* 532 (2017) 66–81. <https://doi.org/10.1016/J.IJPHARM.2017.08.064>.
- [23] W. Huang, C. Zhang, Tuning the size of poly(lactic-co-glycolic acid) (PLGA) nanoparticles fabricated by nanoprecipitation, *Biotechnol J.* 13 (2018). <https://doi.org/10.1002/BIOT.201700203>.
- [24] C. Manzo, M.F. Garcia-Parajo, A review of progress in single particle tracking: From methods to biophysical insights, *Reports on Progress in Physics.* 78 (2015) 124601. <https://doi.org/10.1088/0034-4885/78/12/124601>.
- [25] K. Forier, A.S. Messiaen, K. Raemdonck, H. Deschout, J. Rejman, F. De Baets, H. Nelis, S.C. De Smedt, J. Demeester, T. Coenye, K. Braeckmans, Transport of nanoparticles in cystic fibrosis sputum and bacterial biofilms by single-particle tracking microscopy, *Nanomedicine.* 8 (2013) 935–949. <https://doi.org/10.2217/nnm.12.129>.
- [26] K. Braeckmans, K. Buyens, W. Bouquet, C. Vervaet, P. Joye, F. De Vos, L. Plawinski, L. Doeuvre, E. Angles-Cano, N.N. Sanders, J. Demeester, S.C. De Smedt, Sizing nanomatter in biological fluids by fluorescence single particle tracking, *Nano Lett.* 10 (2010) 4435–4442. <https://doi.org/10.1021/nl103264u>.
- [27] W.I. Goldberg, Dynamic light scattering, *Am J Phys.* 67 (1999) 1152–1160. <https://doi.org/10.1119/1.19101>.
- [28] J. Lim, S.P. Yeap, H.X. Che, L.S. Chun, Characterization of magnetic nanoparticle by dynamic light scattering, *Nanoscale Res Lett.* 8 (2013) 381. <https://doi.org/https://doi.org/10.1186/1556-276X-8-381>.

- [29] Y. Pei, R. Vogel, C. Minelli, Tunable resistive pulse sensing (TRPS), Characterization of Nanoparticles: Measurement Processes for Nanoparticles. (2020) 117–136. <https://doi.org/10.1016/B978-0-12-814182-3.00009-2>.
- [30] W. Anderson, R. Lane, D. Korbie, M. Trau, Observations of Tunable Resistive Pulse Sensing for Exosome Analysis: Improving System Sensitivity and Stability, *Langmuir*. 31 (2015) 6577–6587. <https://doi.org/10.1021/ACS.LANGMUIR.5B01402>.
- [31] E. Weatherall, G.R. Willmott, Applications of tunable resistive pulse sensing, *Analyst*. 140 (2015) 3318–3334. <https://doi.org/10.1039/C4AN02270J>.
- [32] V. Filipe, A. Hawe, W. Jiskoot, Critical evaluation of nanoparticle tracking analysis (NTA) by NanoSight for the measurement of nanoparticles and protein aggregates, *Pharm Res*. 27 (2010) 796–810. <https://doi.org/10.1007/s11095-010-0073-2>.
- [33] P. Kramberger, M. Ciringer, A. Strancar, M. Peterka, Evaluation of nanoparticle tracking analysis for total virus particle determination, *Virology*. 9 (2012) 1–10. <https://doi.org/10.1186/1743-422X-9-265>.

Chapter 2

Frequently used methods

2.1 Methods

2.1.1 Dynamic light scattering (DLS)

The measurement of particle size distribution using the Zetasizer Ultra is relying on dynamic light scattering (also called photon correlation spectroscopy) [1,2]. During the measurement a laser beam is directed at the cuvette containing the sample. Particles in the dispersion to be analyzed scatter the introduced light in every direction [2]. Whereby it must be noted that the intensity of scattered light differs in angle according to the incident light [1]. Due to Brownian motion nanoparticles are moving in the dispersion which leads to a constant change in particle positioning. With respect to particle positions in relation to each other scattered light is influenced by constructive and destructive interference. Changes in interference lead to dimming or brightening up the overall scattered light depending on the scattering direction. Scattered light hitting the photodetector inside the device is consequently fluctuating in intensity due to changing interference behavior caused by particle motion. The faster the particles are moving, the faster the detected light is fluctuating in intensity. From the Stokes-Einstein equation a connection between particle diameter and diffusion speed can be drawn [3,4]:

$$d_H = \frac{kT}{3\pi\eta D}$$

Where d_H is the hydrodynamic particle diameter, k is the Boltzmann constant, T the absolute temperature, η the dynamic viscosity of the dispersant, and D the diffusion coefficient of the particle [3,4].

As it is shown the diffusion coefficient is directly dependent of the particle diameter. To obtain the diffusion coefficient the Zetasizer relies on an autocorrelation function which describes the change of the captured interference light over time by comparing a series of different timepoints. The faster the correlation decreases (which means that the captured image is changing faster over time compared to previous images) the higher is the diffusion speed of the particles and accordingly the smaller is the particle diameter. It is essential for this measurement that all other types of particle movement overlaying diffusion like sedimentation or floating are excluded [4].

Furthermore, this measurement is just applicable to spherical particles and due to relying on scattered light the refractive index and absorption coefficient of the particle material must be known for a precise calculation [1,2]. Depending on temperature, dynamic viscosity, refractive indices, and absorption coefficients the measurement delivers a distribution curve of the hydrodynamic diameter of respective particles. This hydrodynamic diameter is composed of the geometrical particle diameter plus a shell of dispersant molecules arranged around the particle including a cloud of ions which interacts with it and is carried along while the particle is moving due to Brownian motion [5,6]. Consequently, it is important to know that the obtained hydrodynamic diameter is larger compared to the geometrical particle diameter of analyzed spherical particles.

2.1.2 Zeta potential measurement and laser-doppler anemometry

Laser-doppler anemometry, also known as laser-doppler velocimetry, is an analytical method for determining particle velocity in fluids. This method is based on two laser beams crossing each other in the dispersion to be analyzed. In the overlap area both beams generate an interference pattern originated from constructive and destructive interference [7]. To be precise the second beam is generated by separating it from the original beam using a beam splitter [8]. A particle located in the beam intersection is scattering light which can be captured by a detector. In case of particle movement, it inevitably passes regions providing higher or lower light intensity due to the interference pattern. Consequently, particle movement is resulting in a rhythmical change of scattered light intensity which increases with the particle velocity. By capturing the scattered light and analyzing the intensity fluctuation speed the particle velocity can be calculated [7]. For zeta potential measurements the particle acceleration is caused by applying an electric field to the sample resulting in electrophoresis. As it is shown below the electrophoretic mobility of the particle can be calculated by dividing the particle velocity by the applied electric field [5]:

$$\mu_e = \frac{v}{E}$$

Where μ_e is the electrophoretic mobility, v is the measured particle velocity, and E is the applied field strength.

Furthermore, the Henry equation points out how the calculated electrophoretic mobility is related to the zeta potential [5]:

$$\mu_e = \frac{2 * \varepsilon * \zeta * f(kA)}{3 * \eta}$$

Where μ_e is the electrophoretic mobility, ε is the dielectric constant of the dispersant, ζ is the zeta potential, $f(kA)$ is the function of the ratio of particle radius to double layer thickness, and η is the dynamic viscosity [5].

Utilizing the Henry equation, the measured particle velocity can be used for the zeta potential calculation of the detected particles.

The zeta potential corresponds to the remaining potential at the shear plane for counter ions of the considered particle [5,9]. A particle in dispersion attracts ions interacting with the particle. Ions (of both negative and positive charging) forming a double layer which is directly attached to the particle surface built of the inner and outer Helmholtz layer. This double layer is followed by a diffuse layer of solvated ions decreasing in concentration over distance from the particle surface. Accelerating the particle itself leads to tearing of a part of the diffuse layer at a slipping plane [5,9]. Following the potential change by distancing from the particle surface the zeta potential corresponds to the remaining potential at the mentioned slipping plane [5,9]. Here it must be noticed

that the level of the zeta potential is directly influenced by the surface potential of the particle and the Stern potential occurring at the outer Helmholtz layer. Nevertheless, the zeta potential is still ranging below both mentioned potentials caused by the decreasing ion concentration in the diffuse layer [9].

2.1.3 Lyophilization

Lyophilization, also known as freeze drying, is used in this study to remove dispersant from the manufactured nanosuspensions to obtain a powder suitable for a mass balance. To go more into detail, samples were frozen at -80°C which is symbolized in Fig. 2.1 by following the arrow to the left. Subsequently, the air pressure was reduced to 0.200 mbar. This was done by attaching the sample to an Alpha 4-3 LCS Basic (Christ, Osterode, Germany). By the drastic reduction of pressure, the dispersant (in most cases water) is removed via sublimation (symbolized by the downward directed arrow in Fig. 2.1). In the state of reduced temperature and pressure the dispersant is directly changing its state of aggregation from solid to gaseous (and not from solid to liquid) as it can be concluded from the phase diagram of water (Fig. 2.1) [9].

In general, lyophilization is a very gentle process towards the substances to be dried due to the exclusion of high drying energies introduced into the system. This is very beneficial for fragile components (e.g., dyes or drug substances) towards oxidation processes and fluorescence bleaching [10].

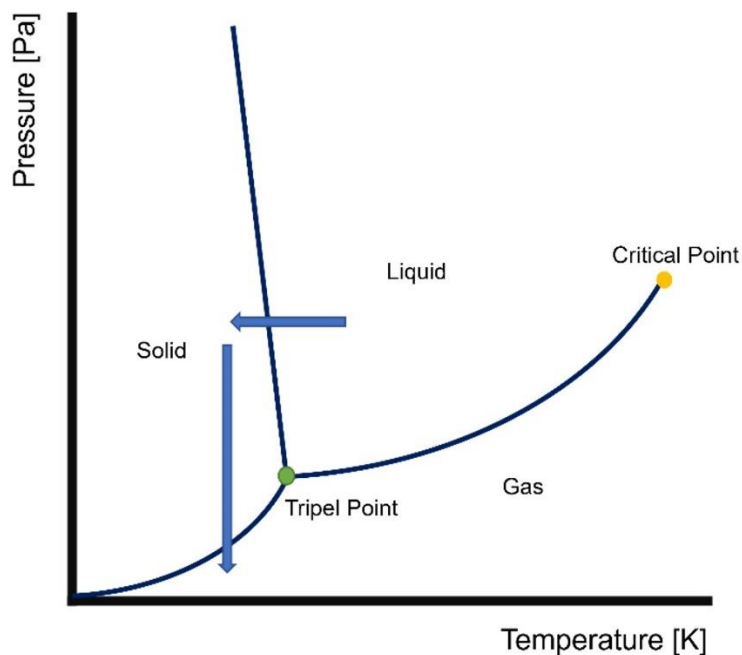


Fig. 2.1. Phase diagram of water. The lyophilization process is symbolized by arrows. The horizontal arrow displays the freezing of the sample. The vertical arrow displays the drying process caused by subliming frozen water into the gas phase by pressure reduction.

2.1.4 Scanning electron microscopy (SEM)

Particles in size ranges below the resolution limit of a conventional light microscope cannot be characterized this way [11,12]. Since nanoparticles should be visualized in this study an alternative visualization method had to be used. SEM is well suited for visualization of particles in a size range around 100 nm [13] (as they are produced in this study). A visualization of such small particles can be guaranteed by utilizing an electron beam instead of light. The great benefit of an electron beam is the much shorter wavelength of electrons (approximately 0.02 – 0.05 nm [14]) making an interaction with particles possible. Image generation relies on an electron beam which is scanning over the sample. This electron beam is generated by an electron source and focused by a system of lenses on a single spot on the sample. The irradiated electron beam induces an emission of secondary electrons from the sample. Secondary electrons are captured and analyzed by a detector and transferred into topographic information of the sample surface. An entire image is built by scanning the focused electron beam over the selected sample surface [15,16].

A drawback of SEM imaging is the destructive behavior towards fragile samples. By longer irradiation of respective sample regions weak materials are destroyed and deformed making imaging of the original topography impossible.

Furthermore, some materials do not provide a strong emission of secondary electrons or being charged by the irradiated electron beam due to low material conductivity which both leads to low image quality. To overcome this drawback many samples are sputtered with a metal layer of a few nanometers consisting of gold or platinum. This thin and well conducting layer conserves the topography of the sample and shows a stronger emission of secondary electrons which leads to improved image quality [16].

2.1.5 Transmission electron microscopy (TEM)

For an even higher precision in imaging of nanoparticles transmission electron microscopy (TEM) was used [17]. Especially for characterization of very small particles this was very beneficial. TEM relies on an electron beam which irradiates a sample and is passing through it. The fraction of the electron beam which could pass through the sample and was not scattered by atoms in the beam path is captured. Capturing an electron beam which is passing through a sample allows to characterize besides the particle morphology also inner structures of the respective particles [18]. To ensure this an electron beam of high intensity is required. TEM electron beams are up to ten times more powerful compared to the SEM beams (TEM: ~200 kV, SEM: ~20 kV) [15–17]. Fractions of the beam which are not scattered or absorbed by the sample are magnified by a system of lenses and captured by a camera. The high intensity of the generated electron beam allows a much higher resolution compared to SEM which is

exploited in this study for comparably small particle systems. Furthermore, TEM allows to visualize particles covered under materials such as residues from particle production. This is highly beneficial for samples which could not be purified perfectly and still show layers of stabilizer on top of the particles. The strength of TEM is simultaneously its disadvantage. A strong electron beam with the potential of imaging particles with a high resolution can easily damage particles if they are built from weak materials.

2.2 References

- [1] W.I. Goldberg, Dynamic light scattering, *Am J Phys.* 67 (1999) 1152–1160. <https://doi.org/10.1119/1.19101>.
- [2] J. Lim, S.P. Yeap, H.X. Che, L.S. Chun, Characterization of magnetic nanoparticle by dynamic light scattering, *Nanoscale Res Lett.* 8 (2013) 381. [https://doi.org/https://doi.org/10.1186/1556-276X-8-381](https://doi.org/10.1186/1556-276X-8-381).
- [3] A. Einstein, Über die von der molekularkinetischen Theorie der Wärme geforderte Bewegung von in ruhenden Flüssigkeiten suspendierten Teilchen, *Ann Phys.* 322 (1905) 549–560. <https://doi.org/10.1002/ANDP.19053220806>.
- [4] C. Cruickshank, The Stokes-Einstein law for diffusion in solution, *Proceedings of the Royal Society of London. Series A, Containing Papers of a Mathematical and Physical Character.* 106 (1924) 724–749. <https://doi.org/10.1098/RSPA.1924.0100>.
- [5] S. Bhattacharjee, DLS and zeta potential – What they are and what they are not?, *Journal of Controlled Release.* 235 (2016) 337–351. <https://doi.org/10.1016/J.JCONREL.2016.06.017>.
- [6] B. Demeler, T.L. Nguyen, G.E. Gorbet, V. Schirf, E.H. Brookes, P. Mulvaney, A.O. El-Ballouli, J. Pan, O.M. Bakr, A.K. Demeler, B.I. Hernandez Uribe, N. Bhattarai, R.L. Whetten, Characterization of size, anisotropy, and density heterogeneity of nanoparticles by sedimentation velocity, *Anal Chem.* 86 (2014) 7688–7695. <https://doi.org/10.1021/ac501722r>.
- [7] J.X.J. Zhang, K. Hoshino, Optical Transducers: Optical Molecular Sensors and Optical Spectroscopy, *Molecular Sensors and Nanodevices.* (2014) 233–320. <https://doi.org/10.1016/B978-1-4557-7631-3.00005-3>.
- [8] C.P. Wang, Laser Doppler velocimetry, *J Quant Spectrosc Radiat Transf.* 40 (1988) 309–319. [https://doi.org/10.1016/0022-4073\(88\)90122-7](https://doi.org/10.1016/0022-4073(88)90122-7).
- [9] A. Fahr, Voigt Pharmazeutische Technologie, Voigt Pharmazeutische Technologie. (2022). <https://doi.org/10.52777/9783769277487>.
- [10] J. Jankun, M. Wyganowska-Swiatkowska, K. Dettlaff, A. Jelinska, A. Surdacka, D. Watróbska-Swietlikowska, E. Skrzypczak-Jankun, Determining whether curcumin degradation/condensation is actually bioactivation (Review), *Int J Mol Med.* 37 (2016) 1151–1158. <https://doi.org/10.3892/ijmm.2016.2524>.
- [11] H. Heinzelmann, D.W. Pohl, Scanning near-field optical microscopy, *Applied Physics A.* 59 (1994) 89–101. <https://doi.org/10.17305/bjbs.2008.3000>.

- [12] Rayleigh, XXXI. Investigations in optics, with special reference to the spectroscope, The London, Edinburgh, and Dublin Philosophical Magazine and Journal of Science. 8 (1879) 261–274. <https://doi.org/10.1080/14786447908639684>.
- [13] D. Primavessy, N. Günday Türeli, M. Schneider, Influence of different stabilizers on the encapsulation of desmopressin acetate into PLGA nanoparticles, *European Journal of Pharmaceutics and Biopharmaceutics*. 118 (2017) 48–55. <https://doi.org/10.1016/j.ejpb.2016.12.003>.
- [14] Y. Wang, J.A. Pan, H. Wu, D. V. Talapin, Direct Wavelength-Selective Optical and Electron-Beam Lithography of Functional Inorganic Nanomaterials, *ACS Nano*. 13 (2019) 13917–13931. <https://doi.org/10.1021/ACS.NANO.9B05491>.
- [15] A. Dubes, H. Parrot-Lopez, W. Abdelwahed, G. Degobert, H. Fessi, P. Shahgaldian, A.W. Coleman, Scanning electron microscopy and atomic force microscopy imaging of solid lipid nanoparticles derived from amphiphilic cyclodextrins, *European Journal of Pharmaceutics and Biopharmaceutics*. 55 (2003) 279–282. [https://doi.org/10.1016/S0939-6411\(03\)00020-1](https://doi.org/10.1016/S0939-6411(03)00020-1).
- [16] S.L. Marusin, Sample preparation — the key to SEM studies of failed concrete, *Cem Concr Compos*. 17 (1995) 311–318. [https://doi.org/10.1016/0958-9465\(95\)00020-D](https://doi.org/10.1016/0958-9465(95)00020-D).
- [17] S.B. Rice, C. Chan, S.C. Brown, P. Eschbach, L. Han, D.S. Ensor, A.B. Stefaniak, J. Bonevich, A.E. Vladár, A.R.H. Walker, J. Zheng, C. Starnes, A. Stromberg, J. Ye, E.A. Grulke, Particle size distributions by transmission electron microscopy: an interlaboratory comparison case study, *Metrologia*. 50 (2013) 663–678. <https://doi.org/10.1088/0026-1394/50/6/663>.
- [18] A.K. Boehm, E. Ionescu, M. Koch, M. Gallei, Combining Soft Polysilazanes with Melt-Shear Organization of Core–Shell Particles: On the Road to Polymer-Templated Porous Ceramics, *Molecules*. 24 (2019) 3553. <https://doi.org/10.3390/MOLECULES24193553>.

Chapter 3

Particle formulation

Contributions to the chapter:

Methodology, experimental design, sample preparation, data analysis, and result interpretations of all experimental data were done by the author of the thesis.

The procedure of pressure calculation for exact microfluidic mixing was developed by Oliver Brieger, Lab for Measurement Technology, Saarland University, Saarbrücken, Germany.

Double-stranded RNA was provided by Marcello Pirritano, Molecular Cell Biology and Microbiology, Wuppertal University, Wuppertal, Germany.

Loading of manufactured nanoparticles on *E. coli* and associated characterization was performed by Kristela Shehu, INM-Leibniz Institute for New Materials, Saarbrücken, Germany.

3.1 Introduction: Particle formulation

Specific problems arise during the development of novel drug substances and drug formulations. Focusing on rare substances (natural or biotechnological products) in early development phases, when available drug mass is limited, undesired waste of substance must be prevented. This complicates the pre-formulation procedure and limits applicability of standard formulation techniques. A reasonable reduction of batch sizes regarding drug formulation was already introduced to literature by Sanofi [1].

It was intended to reduce required substance amounts, both excipients and drug substances, to a minimum. To realize this approach particles were produced using microfluidic systems. A syringe pump-based system was overhauled for establishing an air pressure driven system. This system should work in higher accuracy regarding response time and flow rate ratio while handling very reduced volumes. To guarantee this high precision the built-up air pressure had to be translated correctly into a volumetric flow rate. Based on the Hagen-Poiseuille equation [2] and by applying this equation to all relevant tubes in the system a flow rate calculation could be carried out. By combining all volumetric flow rates in one equation describing the entire microfluidic system a direct relation between applied air pressure at different tubes and the desired flow rate ratio of the fluids inside of the system could be extracted.

Utilizing the established microfluidic system nanoparticles based on different polymers were produced. As particle materials, both lipophilic and hydrophilic polymers were selected to demonstrate the flexibility of the system. The chosen ones were poly(lactic-co-glycolic acid) (PLGA), gelatin, diethylaminoethyl-dextran (DEAE-dextran), and dextran sulfate. By the diversity of applicable polymers, the ability of the introduced setup to serve as a robust platform technology was confirmed. Nanoparticles based on PLGA, or gelatin were produced using precipitation methods relying on the mixing of different solvents and non-solvents resulting either in highly hydrophilic (gelatin) or highly lipophilic (PLGA) particle collectives [3–6]. By developing manufacturing procedures for both particle types a formulation platform for both hydrophilic and lipophilic substances in highly reduced batch sizes was introduced.

Furthermore, particle systems based on more than one polymer forming the particle core were added as a formulation alternative to the previously mentioned particle systems. Relying on complex coacervation [7] DEAE-dextran and dextran sulfate were used to form nanoparticles under controlled conditions using the microfluidic system. By changing the polymer ratio during particle manufacturing, it was investigated if a shift in polymer proportions inside of the particle has an influence on the overall particle charge. For obtaining a surrogate parameter for particle charge and electrostatic repulsion between particles zeta potential measurements [8] were carried out characterizing the produced samples. A strong positive or negative zeta potential would indicate a desired electrostatic stabilization of the particle suspension [9,10] and the possibility to load drugs by exploiting electrostatic interactions on the respective particle.

All mentioned and developed drug delivery systems share the idea of reducing the overall amount of required drug substances and excipients to the lowest possible level. If a promising formulation (manufactured utilizing microfluidics) was found, the possibility arises to scale up the process for manufacturing larger amounts of formulation. This could either be done by scaling up the utilized volumes and masses to benchtop requirements or by parallelizing the microfluidic production and increasing the throughput this way (so-called numbering up).

As a model drug substance to be delivered double-stranded RNA (dsRNA) was selected. For delivering dsRNA into microorganisms to induce RNA interference a delivery system was developed utilizing electrostatic interaction [11]. The microorganism to be addressed was *Paramecium tetraurelia*. To incorporate dsRNA into nanoparticles positively charged DEAE-dextran was mixed with the negative charged nucleic acid leading to complex coacervation. Referring to the size of resulting particles they were considered being too small for an effective phagocytosis. Consequently, particles were manufactured under conditions leading to a positive particle charge and subsequently loaded via electrostatic interaction on negative charged surfaces of *E. coli* bacteria. *E. coli* with attached particles represented a larger delivery system well suited for phagocytosis by *Paramecium* and exploiting the benefit of bacteria being a generic nutritional component for *Paramecium*.

3.2 Materials

PLGA (Resomer RG 503H) was obtained from Evonik Industries AG, Essen, Germany. Acetonitrile was purchased from Fisher Scientific GmbH, Schwerte, Germany. The purification system Millipore, Milli-Q Synthesis, Merck, Darmstadt, Germany provided pure water. Poloxamer 188 was purchased from AppliChem GmbH, Darmstadt, Germany. Ethyl acetate and acetone were obtained from Th. Geyer GmbH & Co. KG, Renningen, Germany. Curcumin, Gelatin from bovine skin (Type B), Cobalt(II) nitrate hexahydrate, and ammonium thiocyanate were obtained from Sigma Aldrich, Taufkirchen, Germany. Dextran sulfate 10 HS and diethylaminoethyl-dextran (DEAE-dextran) 20 were obtained from TdB Labs, Uppsala, Sweden. Phosphate-buffered saline (PBS) was produced in-house using sodium chloride (99.5%) and potassium dihydrogen phosphate obtained from Grüssing GmbH, Filsum, Germany, potassium chloride from Caesar & Loretz GmbH, Hilden, Germany, and disodium hydrogen phosphate from Merck, Darmstadt, Germany.

3.3 Microfluidic particle formulation

3.3.1 Initial microfluidic setup

3.3.1.1 Methods

Microfluidic nanoprecipitation

Microfluidic manufacturing of nanoparticles was carried out by using a microfluidic mixing chip (CapTite Interconnect Cross, LabSmith, Inc., Livermore, CA, USA). To be precise this chip acted like a cross shape interconnect between four capillaries (see Fig. 3.1). By feeding different solutions containing particle material over three inlet capillaries (Z-FSS-100365, Postnova Analytics GmbH, Landsberg, Germany) (Material: Fused silica, inner diameter = 100 μm , outer diameter = 360 μm) into the chip a nanoprecipitation was induced while mixing the different solvents. The resulting particle dispersion was led out over the outlet capillary to be yielded.

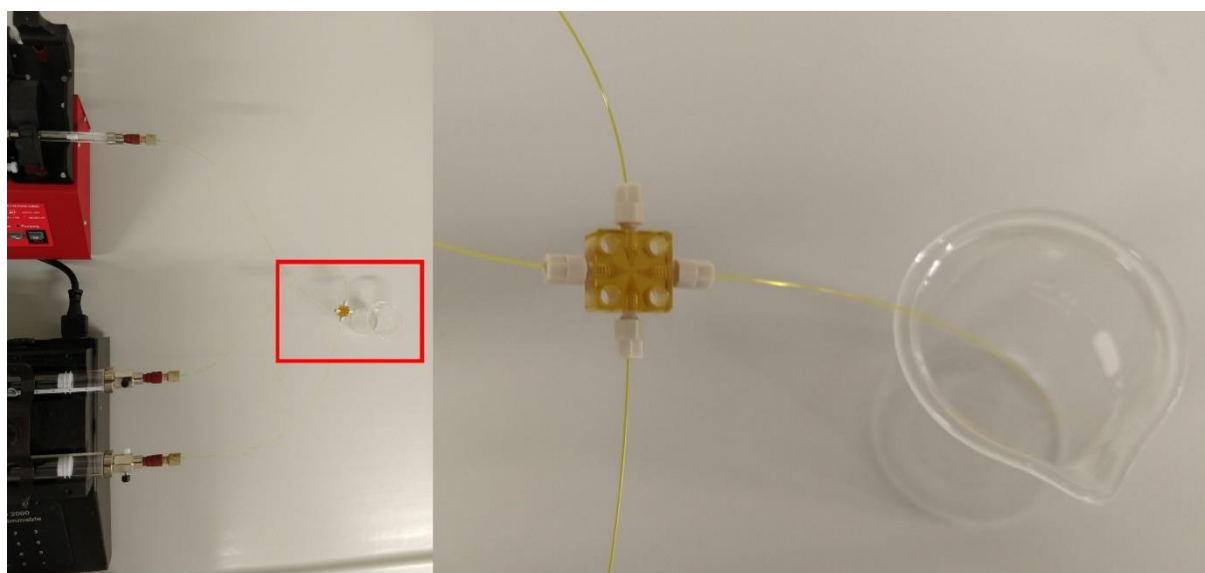


Fig. 3.1. First microfluidic setup for preparation of nanoparticles by nanoprecipitation. Left: Two syringe pumps feeding liquids over glass capillaries into the microfluidic chip. The black pump feeds liquids from the sides into the chip. The red pump feeds through the middle into the chip. Right: Magnification from the red rectangle on the left. Capillaries entering the chip and leading fluids to the reaction chamber for particle production. The final particle suspension leaves the chip over the capillary at the right-hand side and is collected in a vessel.

As an example, for illustrating the microfluidic nanoprecipitation process PLGA (Fig. 3.2) particles were chosen. Their manufacturing process regarding benchtop nanoprecipitation is well described in literature [12–14] and straight-forward to execute. Therefore, a direct transfer to microfluidics appears to be feasible. Besides, PLGA particles are used in many different fields [3,4,13–15] making them interesting as a platform particle system.

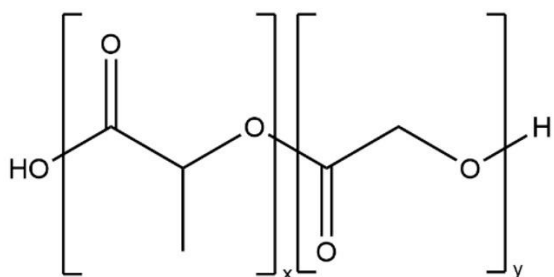


Fig. 3.2. Structure of poly(lactic-co-glycolic acid) (PLGA).

As it is shown schematically in Fig. 3.3 an aqueous solution of poloxamer 188 in water (1 mg mL^{-1}) was pumped from both sides into the mixing zone. Additionally, an organic solution of PLGA dissolved in acetonitrile (3 mg mL^{-1}) was fed over the center into the microfluidic chip. Both solutions were loaded in syringes and fed into the chip using syringe pumps. The organic solution was loaded in a 1 mL SGE glass syringe by Trajan Scientific and Medical, Ringwood, Australia and the utilized pump was made by World Precision Instruments, Sarasota, FL, USA (model name: "Aladdin"). The aqueous solution was loaded in a 10 mL SGE glass syringe by Trajan Scientific and Medical and pumped by a PHD 2000 by Harvard Apparatus, Holliston, MA, USA. Feeding rates for the pumps were set to the following values: $20 \text{ } \mu\text{L min}^{-1}$ (organic) and $2 \times 100 \text{ } \mu\text{L min}^{-1}$ (aqueous). These settings resulted in a flow rate ratio of 1 : 10 with one part of the organic phase and ten parts of the aqueous phase.

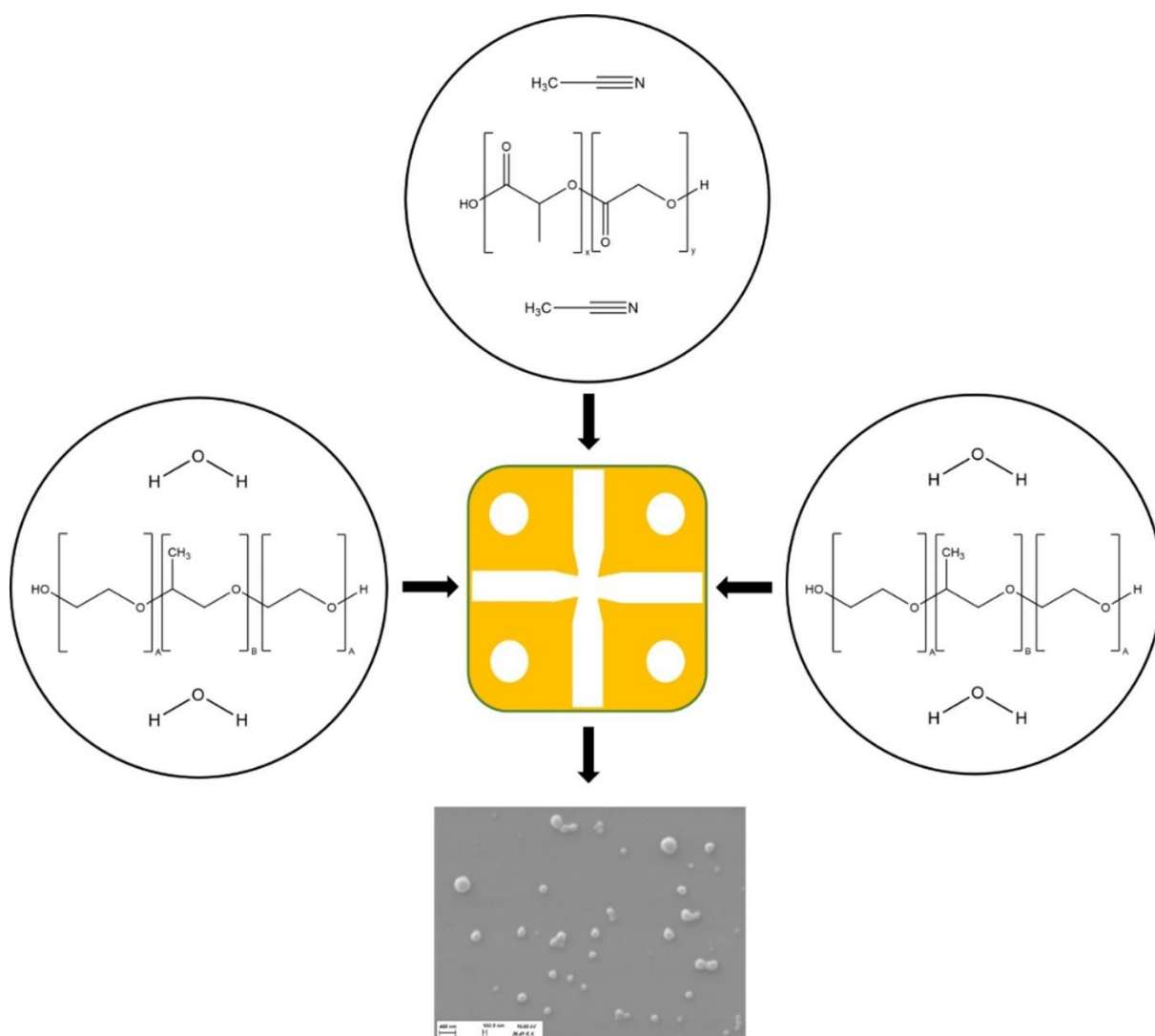


Fig. 3.3. Schematic overview of the microfluidic chip. Poloxamer 188 dissolved in water is pumped from the sides into the mixing zone while PLGA dissolved in acetonitrile is pumped via a central inlet into the chip. The produced particles are collected from the outlet.

Intentionally, acetonitrile and water were chosen regarding their miscibility [16]. While mixing both solutions a single phase results which is hydrophilic due to the relatively low amount of contained organic solvent. PLGA – soluble in acetonitrile – is precipitating in the resulting phase due to the drastically reduced solubility [17]. By increasing the hydrophilicity of the entire system PLGA is forced into supersaturation being a very unstable thermodynamic condition. Subsequently, a nucleation process occurs driven by molecules in supersaturated areas which are associating and forming first nuclei to introduce more thermodynamic stability to the system. This process persists till the critical supersaturation concentration is reached [17]. Nuclei grow further by adding more and more molecules from the system to the emerging cores. This growth stops when the equilibrium saturation concentration is reached for remaining molecules in the dispersant [17].

The precipitation is a fast process which facilitates particle production while both solvents are still mixing (in the cross shaped section of the chip and early regions of the outlet capillary) [3,18]. While forming PLGA nanoparticles in the mixing zone stabilizer molecules – in this case poloxamer 188 – provided by the aqueous solution attach to the particle surface. Molecules like this prevent particle aggregation by steric repulsive forces and conserve a homogeneous nanosuspension [10,19]. The resulting nanosuspension was pumped out over the outlet capillary and was collected.

Particle characterization

Produced PLGA nanoparticles were analyzed regarding their size distribution using the Zetasizer Ultra by Malvern Panalytical GmbH, Kassel, Germany. The size measurement is based on dynamic light scattering (DLS). For sample preparation 100 μL of the produced suspension were diluted with 900 μL Milli-Q water in a sample cuvette. After this dilution step the sample was ready for analysis.

3.3.1.2 Results and discussion

Characteristics of the produced nanosuspension

PLGA nanoparticles could be produced successfully utilizing the mentioned microfluidic system. The produced particle suspension appeared homogeneous and did not show any visible agglomerates. Zetasizer data showed a z-average of 146 nm and a PDI of 0.145 which matched the desired size range for a PLGA particle suspension produced by nanoprecipitation (comparable particle systems show particle sizes (z-average) < 300 nm) [17]. Furthermore, the intensity curve in Fig. 3.4 shows the absence of larger agglomerates in the micrometer range. Especially in this distribution curve larger particles would be visible due to their high scattering intensity in comparison to smaller particles [20]. The curve depicting the particle number shows that most of the particles are in diameter range closely below 100 nm and just a smaller section shows a larger diameter than 100 nm. This set of data matches exactly what was expected regarding particle size.

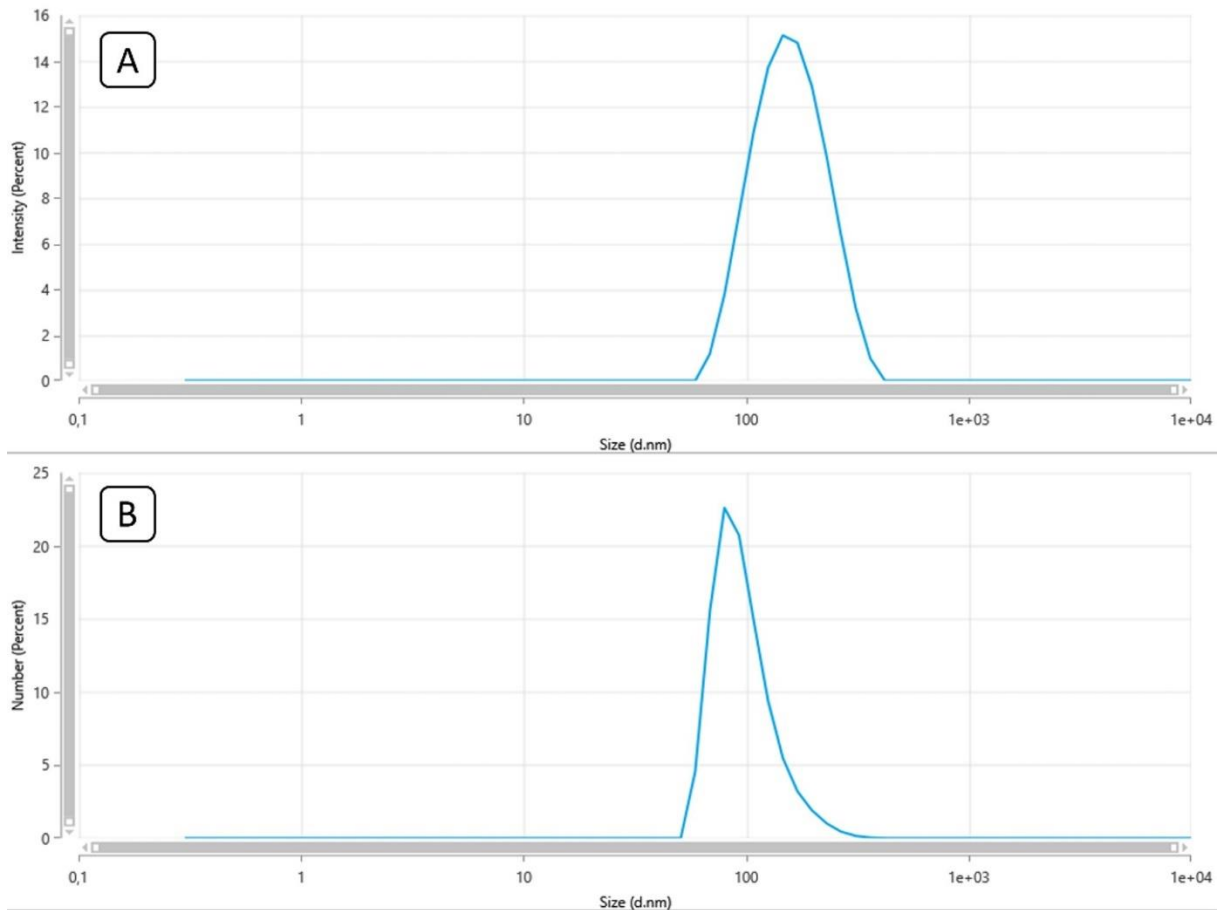


Fig. 3.4. A) Particle size intensity distribution of PLGA nanoparticles showing the particle size with the highest scattering intensity. B) Particle size number distribution of the same particles showing the particle size which occurs most frequently.

Drawbacks of the setup

Due to the nature of the process and the direct precipitation of particle material while the different fluids are brought together precipitated material may stick to the borders of the chip. Consequently, the amount of deposited material is decisive whether this becomes an issue or not. Larger amounts of material cumulating over time can block single capillaries or the entire chip. Fig. 3.5 displays this problem. For easier visualization of interfaces, the images were captured using dark-field microscopy [21,22]. For more detailed information regarding dark-field imaging see chapter five. While A is showing the chip in empty state, B is showing successful particle manufacturing. By feeding the organic phase from the right side and the aqueous phase from the top and the bottom side into the microfluidic chip a stable jet is resulting as desired for a proper mixing of the phases and subsequently a proper precipitation process. C displays agglomerates of particle material deposited on the borders of the microfluidic chip. Those agglomerates disturb the flow and the mixing of both phases and can influence the precipitation process negatively. D shows a completely blocked chip. Large agglomerates of particle material blocked the outlet channel making particle production impossible.

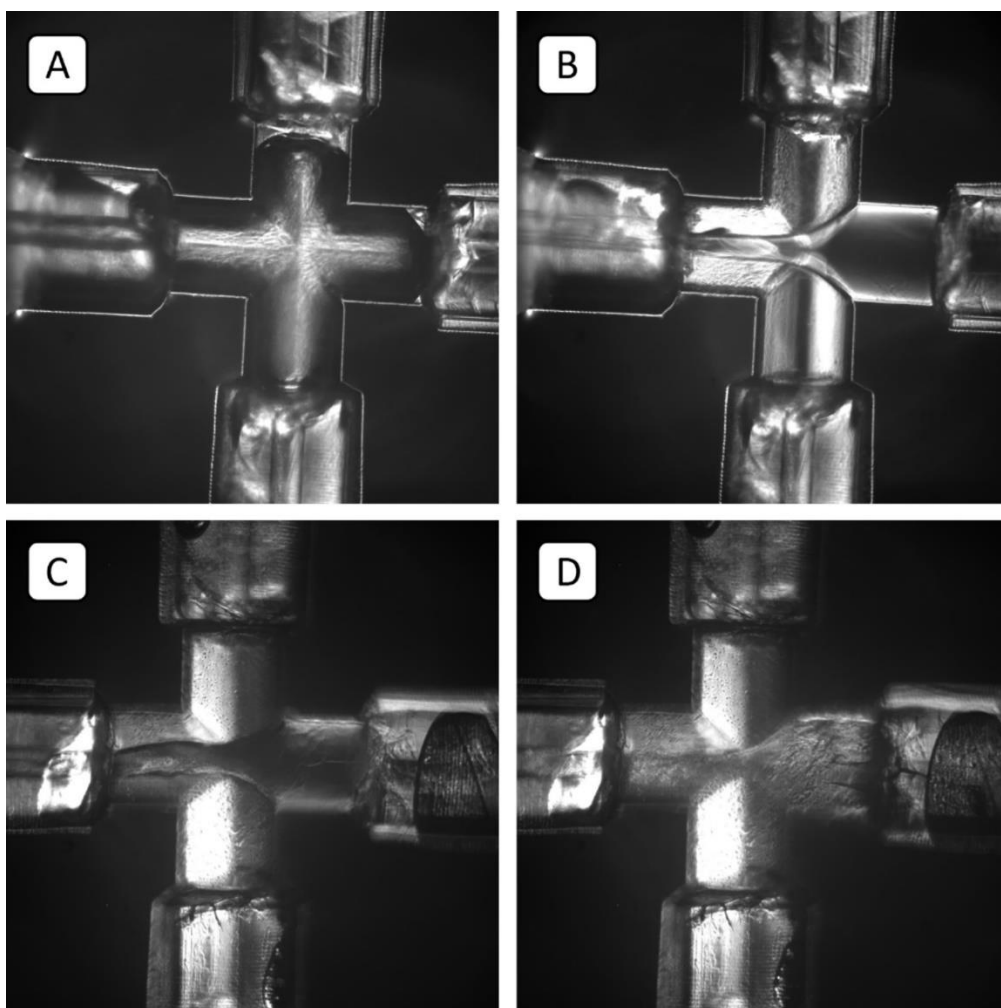


Fig. 3.5. Dark-field visualization of the microfluidic chip's mixing chamber in four different states. A) Empty chip. No liquids inside. B) Chip during the precipitation process showing a stable jet. C) Chip during the precipitation process without a stable jet due to precipitates sticking to the borders (precipitates appear as blurry objects "inside" of the jet due to the two-dimensional imaging). D) Due to larger agglomerates the outlet channel is completely blocked. No further production of particles is possible.

A relevant problem is that blocking of a single inlet capillary cannot be detected during particle production. In the worst case the production process is carried out under wrong mixing conditions over longer production times leading to incorrect dosing, low particle quality, or no particle production at all. It is desirable to detect agglomerates inside of the chip during the process making it possible to dissolve them by flushing with solvent.

Furthermore, the setup using both syringe pumps is not capable of rapid changes in flow rate ratios. Due to high frictions between piston and glass walls and material tension which is consequently built up while pumping (especially for the 15 mL glass syringes) changes in mechanical pumping speed are not directly translated to the resulting flow from the respective syringe. This prevents rapid adjusting the desired flow rate ratio. As an example, reaching the expected flow rate ratio right from the

beginning of the precipitation process can be named. It takes a certain time (few seconds up to a minute) till all desired volumetric flow rates directed into the chip are reached. This can be checked visually using a light microscope while starting the production process. An indicator for a stable flow rate ratio is a consistent shape of the jet. In addition, pulsing solvent into the mixing zone to dissolve larger aggregates is not possible due to the slow reaction time of the system. Consequently, a system translating changes in pumping settings directly to the desired flow rate ratio is desirable.

Ideas for improvement of the setup

It was highly desired to improve the existing setup by adding the opportunity to visualize the precipitation process onstream. A light microscope installed into the existing setup would be beneficial for this reason. Additionally, a pumping system improving control over the flow rate ratio and translating changes in setting directly to a change in flow rate without a delay would be beneficial as well. The ability to dissolve and discard onstream detected aggregates inside of the utilized microfluidic chip by pulsing solvent into it would make the entire system much more flexible and reliable compared to the initial microfluidic setup.

3.3.2 Improved microfluidic setup

3.3.2.1 Methods

Microfluidic nanoprecipitation

The improved microfluidic setup relied on the same microfluidic chip as the initial one (CapTite Interconnect Cross from LabSmith). In contrast to the initial setup the used capillary system was shortened. Still using the same capillary type (fused silica capillaries with an inner diameter of 100 μm) the single capillaries are shortened to roughly 5 cm (the length was remeasured for every single particle production) and attached to a tubing system consisting of polyethylene tubes as it is shown in Fig. 3.6 C. This shortening vastly reduced the fluidic resistance allowing to utilize a pump applying air pressure in a maximum of 1 bar above atmospheric pressure for pumping fluids through the capillaries. The used pump consisted of a pressure source (PVS from Biophysical Tools GmbH, Wettin-Löbejün, Germany) and a pressure controller (P²CS from Biophysical Tools) (Fig. 3.6 A) distributing the built-up air pressure to different glass vials containing the liquids for particle manufacturing. By applying air pressure to the respective vials, liquids inside are pumped out over the tubing to the capillaries leading to the microfluidic chip (see Fig. 3.6 B). The mixing process inside of the chip remains as it was already described for the initial setup.

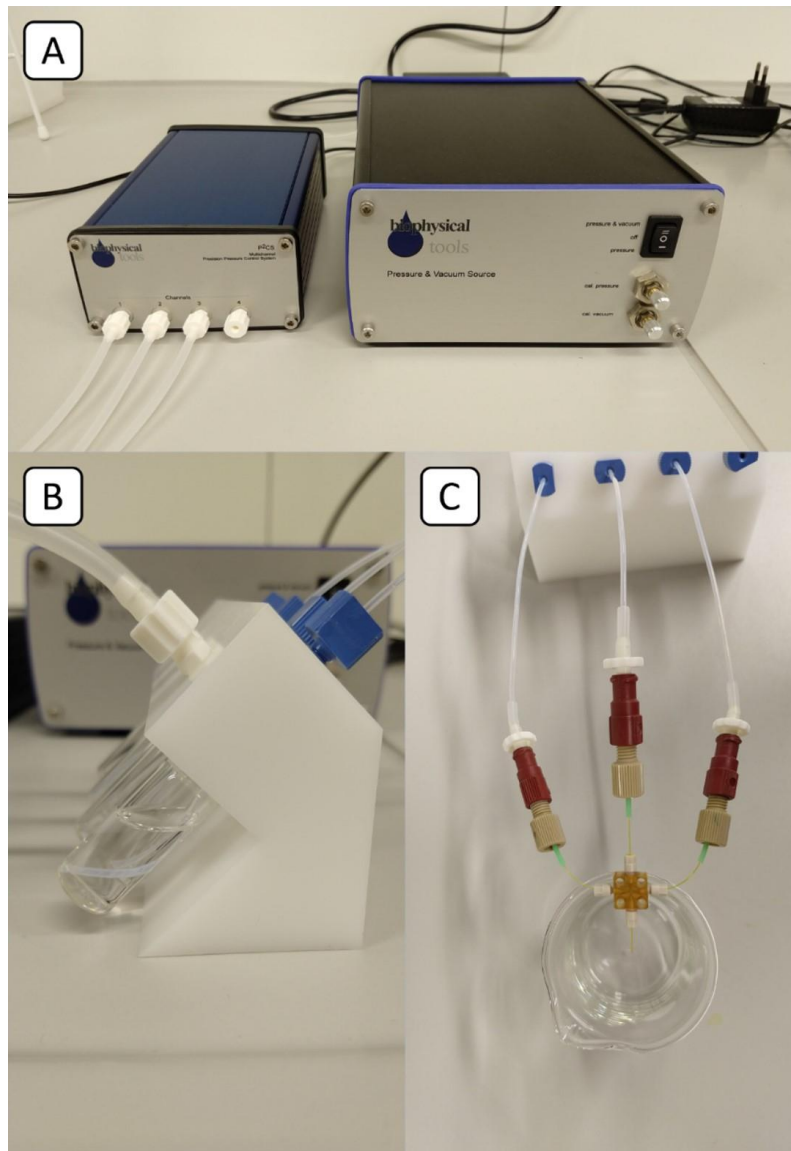


Fig. 3.6. Overhauled microfluidic setup for preparation of nanoparticles by nanoprecipitation. A) Pressure source for generating air pressure (max. pressure: 1000 mbar) and pressure controller for distributing the pressure over four different channels, if needed. B) Glass vials containing the liquids to be mixed. The flow rate out of the vials is controlled by the applied air pressure. C) Tubing system, which leads to the capillaries and subsequently to the microfluidic chip. The produced nanosuspension leaves the chip over a short outlet capillary and is collected in a vessel.

By adding a light microscope to the setup, supervision of the mixing process during particle manufacturing was made possible. The used microscope was a BH-2 from Olympus/Evident, Hamburg, Germany equipped with an air-objective DPlan 10 (Olympus/Evident) with a numerical aperture (NA) of 0.25. By placing the microfluidic chip in the focus of the objective the production process could be visualized at any time. The entire setup including the microscope is shown in Fig. 3.7.

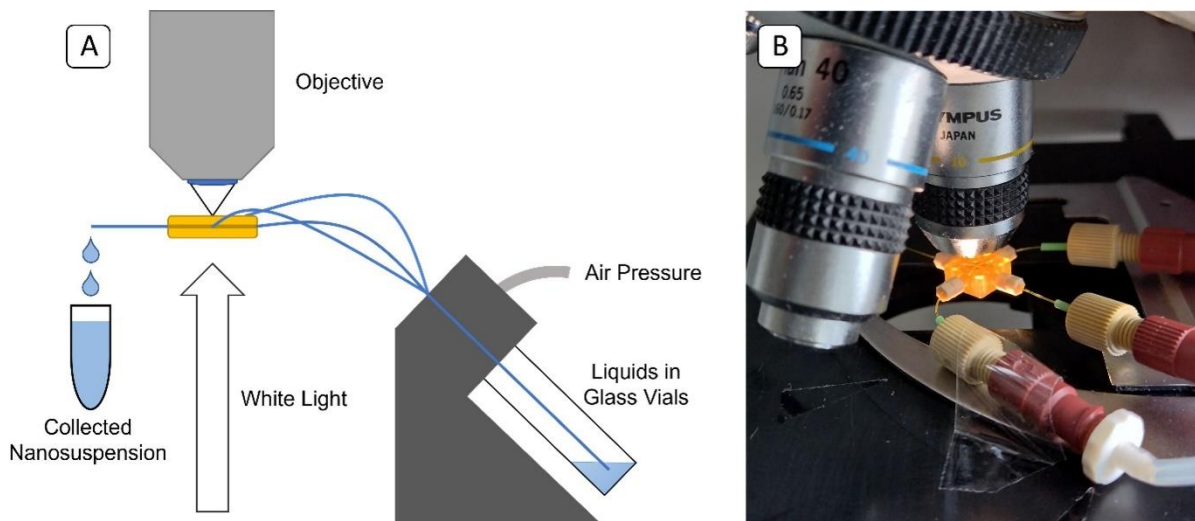


Fig. 3.7. Upgrade for the microfluidic setup for onstream monitoring of the precipitation process inside of the microfluidic chip. A) Schematic overview showing the microfluidic chip (orange) with three attached inlet capillaries (blue), one attached outlet capillary (blue), the light source, and the objective of a light microscope. B) Illuminated microfluidic chip with attached capillary system in the focus of the objective for imaging the mixing process.

Once again as a model particle system PLGA nanoparticles were manufactured using this improved system. Solutions for particle manufacturing were kept identical to the mentioned production utilizing the initial setup. The organic solution of PLGA dissolved in acetonitrile (3 mg mL^{-1}) was fed over the center into the mixing zone whereas the aqueous solution of poloxamer 188 in water (1 mg mL^{-1}) was pumped from both sides into the microfluidic chip. By applying a fixed pressure of 250 mbar to the aqueous solution the corresponding pressure to be applied on the organic solution was calculated. To achieve an organic solvent content of 10% for the final suspension a calculation was performed using a MATLAB (MathWorks, Natick, United States) script. The calculation procedure in detail is shown in the next subsections. The final nanosuspension was yielded from the outlet capillary. Afterwards, the suspension was purified using the Centrisart system (Sartorius Stedim Lab Ltd., Stonehouse, UK) and further analyzed. Purification and sample preparation are described in subsections below.

Calculation of the flow rate ratio

To achieve a precise flow rate ratio with the microfluidic chip applied air pressures must be chosen correctly. The greatest obstacle were the different viscosities of the fluids to be mixed. Relying on the Hagen-Poiseuille equation [2] the applied pressure on the organic phase (lipophilic and pumped into the center of the chip) to achieve a certain flow rate ratio was calculated while the pressure on the aqueous phase (hydrophilic and pumped from the sides) was considered as fixed.

The Hagen-Poiseuille equation was applied for all four capillaries [2].

$$Q = \frac{\pi \cdot R^4 \cdot \Delta p}{8 \cdot \eta \cdot L}$$

Where Q is the volumetric flow rate, R is the inner radius of the capillary, Δp is the pressure difference between the beginning and the end of the capillary, L is the length of the capillary, and η is the dynamic viscosity.

While calculating using the Hagen-Poiseuille equation a pressure difference between the inlet and the outlet of the capillary must be known. The three inlet capillaries show a pressure difference between applied air pressures and the prevailing pressure (p_M see Fig. 3.8) at the mixing point of the chip. For the outlet capillary the pressure difference occurs between the prevailing pressure at the mixing point and the atmospheric pressure at the outlet. Due to a not measurable pressure at the mixing point caused by limitations of the setup this pressure had to be expressed by using the remaining variables.

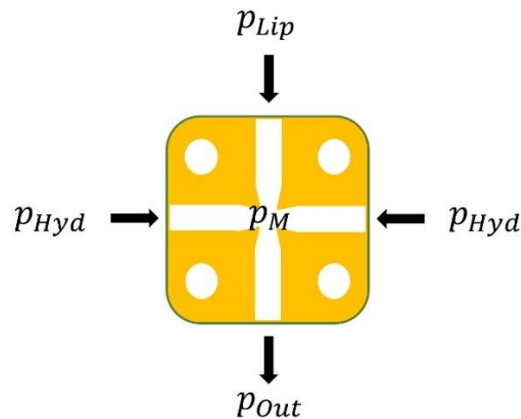


Fig. 3.8. Schematic overview of the microfluidic chip with applied and occurring pressures. (Lip = lipophilic inlet, Hyd = hydrophilic inlet, M = middle of the chip, Out = outlet of the chip)

Having in mind that the inner capillary radius, fluid viscosity, and capillary length were either known or already measured they were expressed as a single factor as it is done in the following simplified equations.

For both capillaries leading from the sides into the chip and containing the hydrophilic / aqueous phase, the volumetric flow rate was described using the following equation:

$$Q_{Hyd} = \frac{\pi \cdot R_{Hyd}^4}{8 \cdot \eta_{Hyd} \cdot L_{Hyd}} \cdot (p_{Hyd} - p_M) = A \cdot (p_{Hyd} - p_M)$$

Where p_{Hyd} is the pressure applied on the hydrophilic phase by the pump and p_M is the occurring pressure in the middle of the chip.

For the capillary feeding the lipophilic / organic phase into the chip, the volumetric flow rate was described using the following equation:

$$Q_{Lip} = \frac{\pi \cdot R_{Lip}^4}{8 \cdot \eta_{Lip} \cdot L_{Lip}} \cdot (p_{Lip} - p_M) = B \cdot (p_{Lip} - p_M)$$

Where p_{Lip} is the pressure applied on the lipophilic phase by the pump and p_M is the occurring pressure in the middle of the chip.

For the outlet capillary leaving the chip, the volumetric flow rate was described using the following equation:

$$Q_{out} = \frac{\pi \cdot R_{out}^4}{8 \cdot \eta_{out} \cdot L_{out}} \cdot (p_M - p_{out}) = C \cdot (p_M - p_{out})$$

Where p_{out} is the atmospheric pressure and p_M is the occurring pressure in the middle of the chip.

All volumetric flow rates leading into the chip corresponded to the volumetric flow leaving the chip. This is summarized by the following equation:

$$Q_{out} = 2 \cdot Q_{Hyd} + Q_{Lip}$$

By expressing the volumetric flow rates through the corresponding pressure differences multiplied by the respective factor the following equation results:

$$C \cdot (p_M - p_{out}) = 2 \cdot A \cdot (p_{Hyd} - p_M) + B \cdot (p_{Lip} - p_M)$$

And by rearranging this equation the unknown pressure in the middle of the chip (p_M) can be expressed as follows:

$$p_M = \frac{(C \cdot p_{out} + 2 \cdot A \cdot p_{Hyd} + B \cdot p_{Lip})}{2 \cdot A + B + C}$$

Expressing p_M by a second equation was done in the following to equalize both equations for the elimination of p_M . Besides, the flow rate ratio between lipophilic and hydrophilic phase was included in the second equation. This ratio is a critical factor for the microfluidic production of nanoparticles and must be known for a precise particle production and drug loading.

The second rearranging to p_M is shown below:

$$Q_{out} = 2 \cdot Q_{Hyd} + Q_{Lip}$$

$$\frac{Q_{out}}{2 \cdot Q_{Hyd}} = 1 + \frac{Q_{Lip}}{2 \cdot Q_{Hyd}} = 1 + Ratio$$

$$\frac{Q_{out}}{2 \cdot Q_{Hyd}} - 1 = Ratio$$

Here volumetric flow rates were expressed again by the corresponding pressure differences multiplied by the respective factor:

$$\frac{C \cdot (p_M - p_{out})}{2 \cdot A \cdot (p_{Hyd} - p_M)} - 1 = Ratio$$

$$p_M = \frac{C \cdot p_{out} + 2 \cdot A \cdot p_{Hyd} \cdot (1 + Ratio)}{C + 2 \cdot A \cdot (1 + Ratio)}$$

By equalizing both equations resolved to p_M and eliminating p_M in this way an equation was obtained for the calculation of the pressure to be applied on the lipophilic phase. This pressure calculation is dependent of an already selected pressure for the hydrophilic phase and is directly influenced by the desired flow rate ratio of both phases:

$$p_{Lip} = \frac{E \cdot (C \cdot p_{out} + 2 \cdot A \cdot p_{Hyd} \cdot (1 + Ratio))}{B \cdot (C + 2 \cdot A \cdot (1 + Ratio))} - \frac{D}{B}$$

For simplification of the equation factors D and E were introduced in addition to the previously mentioned factors A , B , and C :

$$D = C \cdot p_{out} + 2 \cdot A \cdot p_{Hyd}$$

$$E = 2 \cdot A + B + C$$

The pressure to be applied on the lipophilic/organic solution for reaching a desired flow rate ratio inside of the chip could be calculated by feeding the equation with all known variables. All capillaries showed the same inner diameter of 100 μm and the respective capillary length was measured manually for each microfluidic production. The viscosities of all utilized fluids were measured using a micro capillary viscosimeter as it is shown in the following subsection. By choosing a pressure to be applied on the hydrophilic/aqueous solution and the desired flow rate ratio the corresponding pressure for the organic phase could be calculated. The tubing system leading all fluids to the capillary system was excluded from the calculation. The reason for this is the inner diameter of the tubing, which is more than ten times larger than the inner diameter of the capillaries. Since the radius is included in the Hagen-Poiseuille equation to the power of four the fluidic resistance of this tubing was considered as not significant.

Viscosity and density measurements

For a precise pressure calculation, viscosities of all fluids in the system must be known. All solutions brought into the chip and as well the particle suspensions leaving the chip were analyzed using a micro capillary viscosimeter (Ubbelohde type) from Xylem Analytics Germany GmbH, Weilheim, Germany. Since all mentioned fluids were considered as Newtonian fluids, this viscosimeter type was suited for analysis. To obtain viscosities of the mentioned fluids a 15 mL sample was separated from the prepared solutions and analyzed using the viscosimeter. Regarding the particle

suspension in the outlet channel a 15 mL sample was benchtop preprepared. The preparation was carried out by loading one of both solutions in a disposable syringe and feeding it over roughly 30 seconds under stirring into the other solution. By analogy with the microfluidic production the solution loaded into the syringe represents the solution pumped into the chip via the central inlet. The resulting dispersion was identically analyzed compared to all other fluids.

Viscosity measurements were carried out by measuring the time it takes for a certain volume to pass the capillary section of the viscosimeter. After filling the measuring device with the respective fluid, the required time for the liquid surface was measured to travel from marking A to marking B (see Fig. 3.9). The biggest advantage of this Ubbelohde type is the additional venting tube which guarantees a connection between the surrounding air and the vented space under the capillary section. This provides atmospheric pressure under and above the capillary which is excluding errors caused by the hydrostatic pressure of liquid in the entire system.

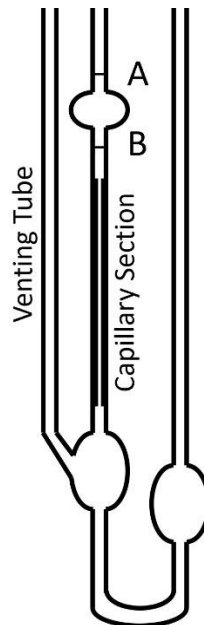


Fig. 3.9. Ubbelohde micro capillary viscosimeter

By measuring the mentioned time, the kinematic viscosity could be obtained:

$$\nu = K * t$$

Where ν is the kinematic viscosity, K is a device constant (for the utilized viscosimeter = $0.009983 \text{ mm}^2 \text{ s}^{-2}$), and t is the required time for the fluid surface in the measurement tube to travel from marking A to marking B.

To calculate the dynamic viscosity the density of respective fluids must be known. Density determination of all analyzed fluids was performed by filling 10 mL of the already mentioned samples into a volumetric flask and measuring the weight of it.

Dividing the measured mass by the volume results in the density which directly could be used for the calculation of the dynamic viscosity:

$$\eta = \nu * \rho$$

Where η is the dynamic viscosity, ν is the kinematic viscosity, and ρ is the density of the fluid.

Particle purification of small particle samples

To minimize particle loss and to keep particle yields as high as possible the Centrisart system was utilized for particle purification. The used version was equipped with a polyethersulfone membrane showing a molecular weight cut-off at 300,000 Dalton. In comparison to conventional purification methods like centrifuging particles into a pellet which can be manually separated from the supernatant [23] the Centrisart system is separating particles from the dispersant by filtration. As visualized in Fig. 3.10 the system consists of two tubes. An outer tube which acts as a container for the nanosuspension to be purified and an inner tube which is sealed with a filter membrane at the bottom. For purification up to 2.5 mL of the manufactured nanosuspension (shown in orange, Fig. 3.10) were filled into the outer tube and the inner tube was placed on the suspension. By applying centrifugal forces of 200 g for 120 minutes at 20°C the inner tube was pushed against the nanosuspension. While nanoparticles were blocked the dispersant was passing the membrane using much lower centrifugal forces than in conventional purification. This led to a higher concentration of nanoparticles between the outer and inner tube (shown in dark orange, Fig. 3.10) while dispersant was separated into the inner tube (shown in blue, Fig. 3.10). The idea was to yield as much particles as possible from highly diluted nanosuspensions and to discard non encapsulated drug substance with redundant dispersant. Centrifugal forces were intentionally set very low to keep particles from aggregating by reducing the tendency to form a pellet. In addition, no higher centrifugal force was required to move the inner tube towards the bottom due to a significantly larger weight of the tube compared to single nanoparticles. Consequently, centrifugation times were kept high to assure a sufficient time frame for the inner tube to travel to the bottom of the outer tube. After the separation process the inner tube containing most of the dispersant was taken out and the concentrated particle suspension could be yielded.

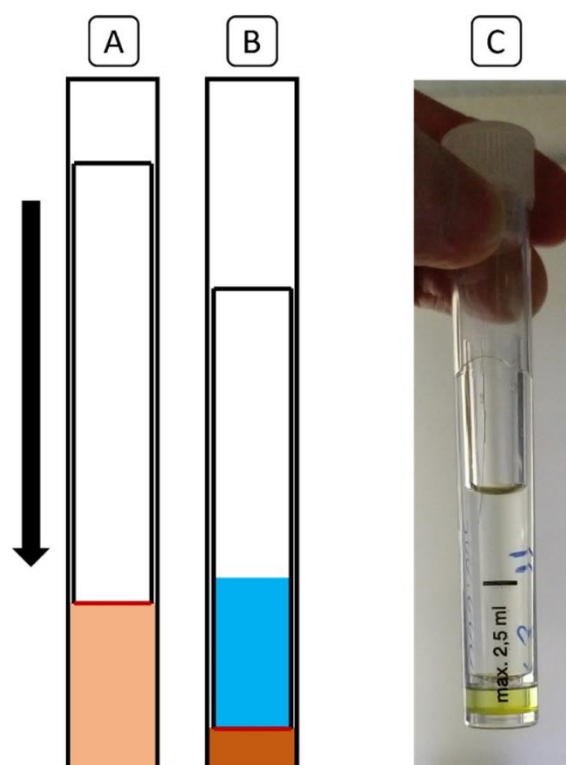


Fig. 3.10. Schematic overview of the Centrisart purification system consisting of an outer and an inner tube. The inner tube provides a filter membrane at the bottom (red). A) Centrisart with loaded particle suspension (orange) before centrifugation. B) Centrisart after centrifugation with purified and concentrated particle suspension (dark orange) and separated dispersant in the inner tube (blue). C) Image of a used Centrisart system. The concentrated and yellow colored particle suspension (curcumin loading for better visualization) is trapped between the tubes. The inner tube contains the color free dispersant.

Particle retention efficiency of the purification system

To ensure that produced particles do not pass the membrane of the inner tube during the purification, produced PLGA nanoparticles were loaded with curcumin and their fluorescence signal was measured in the filtrate. Curcumin (shown in Fig. 3.11) was selected due to its already described successful loading on PLGA particles [4] and its fluorescent behavior [24,25], which ensures a simple and sensitive fluorescence-based quantification of loaded particles.

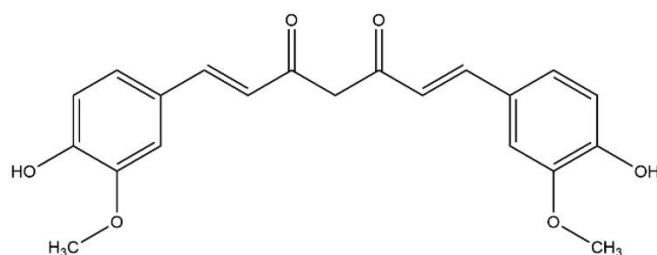


Fig. 3.11. Structure of curcumin (keto form).

For calibration a new PLGA nanoparticle suspension was produced as a triplicate using the improved microfluidic system as previously described. The final suspension showed a particle material content of 0.6 mg mL^{-1} including a curcumin content of $10 \text{ }\mu\text{g}$ curcumin per 1 mg PLGA. Poloxamer 188 was used as a stabilizer in a concentration of 0.25 mg mL^{-1} in the final dispersion. From the produced suspensions a dilution series was prepared. Suspensions in this series contained 100%, 75%, 50%, 25%, 10% and 1% of particle material. The dilutions were analyzed regarding fluorescence intensity using a plate reader (Infinite M200, Tecan Deutschland GmbH, Crailsheim, Germany) at an excitation wavelength of 430 nm and an emission wavelength of 515 nm. Those wavelengths were obtained by capturing respective spectra of pure curcumin in acetonitrile. For more detailed information about absorption and emission spectra of curcumin see chapter four.

To quantify the amount of particles passing the filter membrane, the previously used suspension for calibration was again prepared as a triplicate. All three suspension were purified using Centriscarts at $5,000 \text{ g}$ for 30 minutes at 20°C . The centrifugation conditions were intentionally increased (compared to previously selected purification conditions: 200g , 120 min) to stress the system and to force particles into passing the membrane by increasing the pressure of the inner tube on the suspension. By measuring the fluorescence intensity of the original produced suspension and the resulting filtrate after purification a ratio in percent could be calculated how much material passed the membrane.

Quantification of the remaining stabilizer

The quantification of poloxamer 188 in the filtrate of the purified particle suspension was carried out as already described in literature [26]. 0.24 g of cobalt(II) nitrate hexahydrate and 1.00 g ammonium thiocyanate were dissolved in 5 mL Milli-Q water. By dissolving both chemicals in water a red and water soluble tetrathiocyanatocobaltate(II) complex is forming. Addition of poloxamer 188 to this solution leads to a stronger complex formed by the oxygen atoms of poloxamer with cobalt(II) ions which is colored in blue. The new formed complexes are not soluble in water and are subsequently precipitating. For calibration a dilution series of poloxamer 188 in Milli-Q water was prepared containing concentrations of 3 mg mL^{-1} , 2 mg mL^{-1} , 1.5 mg mL^{-1} , 1 mg mL^{-1} , 0.5 mg mL^{-1} , 0.25 mg mL^{-1} , 0.1 mg mL^{-1} and 0.05 mg mL^{-1} . Samples to be analyzed originated from the same suspensions which already were produced to check for particle retention efficiency as described previously. The samples were taken from the original produced suspension and the filtrate after purification (both triplicates). By dividing the poloxamer 188 content in the filtrate by the content in the original suspension a ratio in percent could be calculated displaying how much poloxamer 188 passed the membrane. Each 0.3 mL taken from the calibration solutions and all samples were mixed with 0.15 mL of cobalt(II) nitrate hexahydrate / ammonium thiocyanate solution in an Eppendorf reaction tube and

centrifuged at 3,000 g for 3 minutes at 20°C. The precipitate was washed several times with 0.3 mL ethyl acetate till the organic supernatant appeared colorless (the tetrathiocyanatocobaltate(II) complex appears blue in ethyl acetate) (see Fig. 3.12). While separating ethyl acetate in each washing step from the pellet, water still being present in the reaction tube is taken away step by step. The washed pellet consisting of the cobalt(II) poloxamer 188 complex was dried by evaporating remaining ethyl acetate on the laboratory bench. After one hour of drying the pellet was dissolved in 1.5 mL acetone and the resulting solution was quantified using the plate reader. The absorption of the complex in acetone was measured at 624 nm [26].



Fig. 3.12. Blue colored cobalt(II) poloxamer 188 complex as precipitate at the bottom of the reaction tubes. Free tetrathiocyanatocobaltate(II) is coloring the aqueous phase red and the ethyl acetate phase blue.

Particle characterization

Particle size was analyzed using the Zetasizer Ultra. Sample preparation was carried out by diluting 100 μL of the produced suspension with 900 μL Milli-Q water in a sample cuvette.

Furthermore, a scanning electron microscopy (SEM) sample was prepared by fixing a piece of a silica wafer on a SEM sample holder via a carbon disc. The purified nanosuspension was drop-casted on the surface of the silica wafer. After roughly 20 seconds of incubation at room temperature the liquid was removed to leave particles on the silica surface. Exploiting capillary forces the droplet was dried by removing it with a tissue.

This suspension was exceptionally purified using a conventional centrifugation method to remove as much stabilizer as possible. As preliminary experiments showed, a single Centrisart purification run trapped certain amounts of stabilizer in the yielded suspension making SEM imaging difficult due to particles covered completely by stabilizer in dried state. To avoid multiple Centrisart runs for complete stabilizer removal a conventional centrifugation-based purification appeared more suitable. A

larger particle loss during centrifugation was accepted for exploiting the benefit of a simple and effective stabilizer removal. Particles were centrifuged into a pellet at 10,000 g for 30 minutes at 20°C using a Multifuge X1R from Thermo Scientific, Waltham, Massachusetts, USA. The supernatant was discarded, and the yielded pellet was redispersed in 5 mL Milli-Q water by vortexing and ultra-sonification using an Elmasonic P from Elma Schmidbauer GmbH, Singen, Germany.

SEM images were captured using an EVO HD15 by Zeiss, Jena, Germany, after the sample was gold sputtered [27].

3.3.2.2 Results and discussion

Microfluidic nanoprecipitation

PLGA nanoparticles could be produced successfully utilizing the improved microfluidic system. Again, the particle suspension appeared homogeneous and did not show any visible agglomerates. Zetasizer data showed a z-average of 167 nm and a PDI of 0.131 which is well comparable with the initial setup (z-average = 146 nm, PDI = 0.145). Furthermore, obtained SEM images confirmed the particle size predicted by the Zetasizer except for few larger particles (see Fig. 3.13), which are nevertheless typical for these particle systems [3,28,29].

A great advantage of the setup is the possibility to change pumping speeds rapidly. By adjusting the pressure, the feeding rate immediately changes. This was highly beneficial for washing out agglomerates inside of the chip or capillaries and furthermore very helpful while starting the precipitation process. Right from the start the desired flow rates can be applied to the microfluidic chip making a production of particles possible without time delay. This could be checked visually by following the air escaping from the tubing system and observing the instant formation of a stable jet inside of the mixing zone. In contrast, the initial setup always needed a certain time till the flow rates leveled at the desired value (stable and not changing jet). This waste of material and time could be drastically reduced by introducing the improved setup.

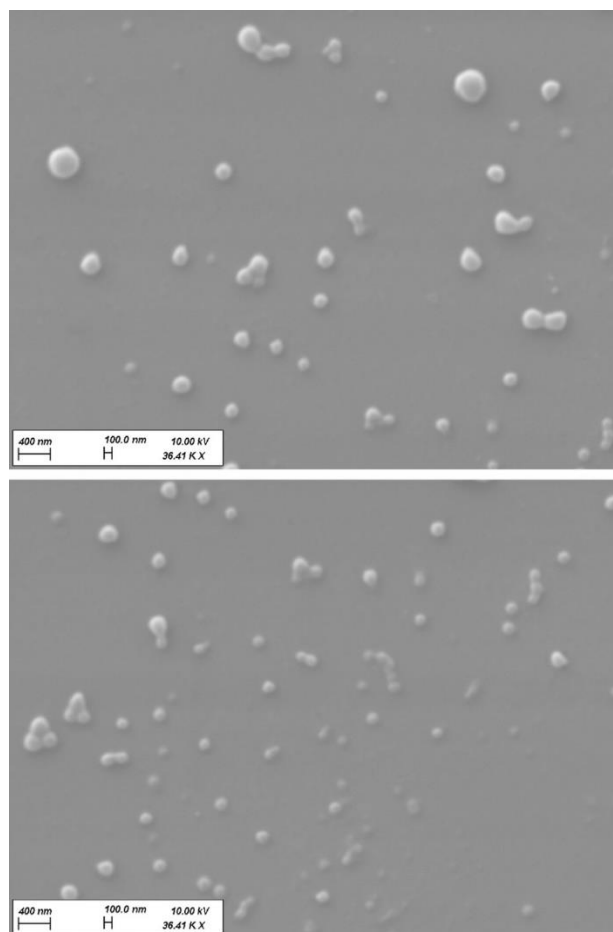


Fig. 3.13. SEM micrographs of PLGA particles produced by the microfluidic system.

Precision of the ratio calculation

Investigating the pressure to be applied on the organic phase in relation to a fixed pressure value applied on the aqueous phase leads to the observation that the flow of the organic phase is reversing by reducing the applied pressure below a certain threshold. Concluding, this behavior occurs when the applied pressure falls below the pressure in the mixing zone (p_M). For visualization the relation between the proportion of organic phase to the mixing process and respective applied pressure was plotted using MATLAB and shown in Fig. 3.14. Image A indicates a flow rate of zero (red circle) regarding the organic phase into the mixing area by applying the corresponding pressure. Subsequently, a negative value indicates a reverse flow of the organic phase. This behavior was exploited for measuring the precision of the calculation.

By producing the model particle system based on PLGA and curcumin which was previously used to check for particle retention efficiency and removal of stabilizer from the suspension a fixed pressure of 1000 mbar was applied to the non-colored aqueous phase. Including the measured capillary lengths and obtained viscosity values into the calculation a pressure of 450 mbar was identified for the yellow-colored organic phase to achieve a flow rate of exactly zero with no contribution to the mixing process. Yet, the resulting mixture showed a very faint yellow due to contained curcumin (see

Fig. 3.14 B). This very light coloring was attributed either to a remaining very little flow or diffusion of curcumin from the capillary end into the mixing zone. Applying a pressure of 440 mbar to the organic phase resulted in a yielded fluid which was not colored indicating a reverse flow for the organic phase and no contribution to the mixing process (see Fig. 3.14 B). By increasing the pressure to 460 mbar the yielded suspension was strongly colored in yellow indicating a contribution of organic phase to the mixing process.

This outcome could reproduce what was calculated before to a precision down to 10 mbar ensuring that the pressure calculation can be utilized for further particle productions in different desired flow rate ratios.

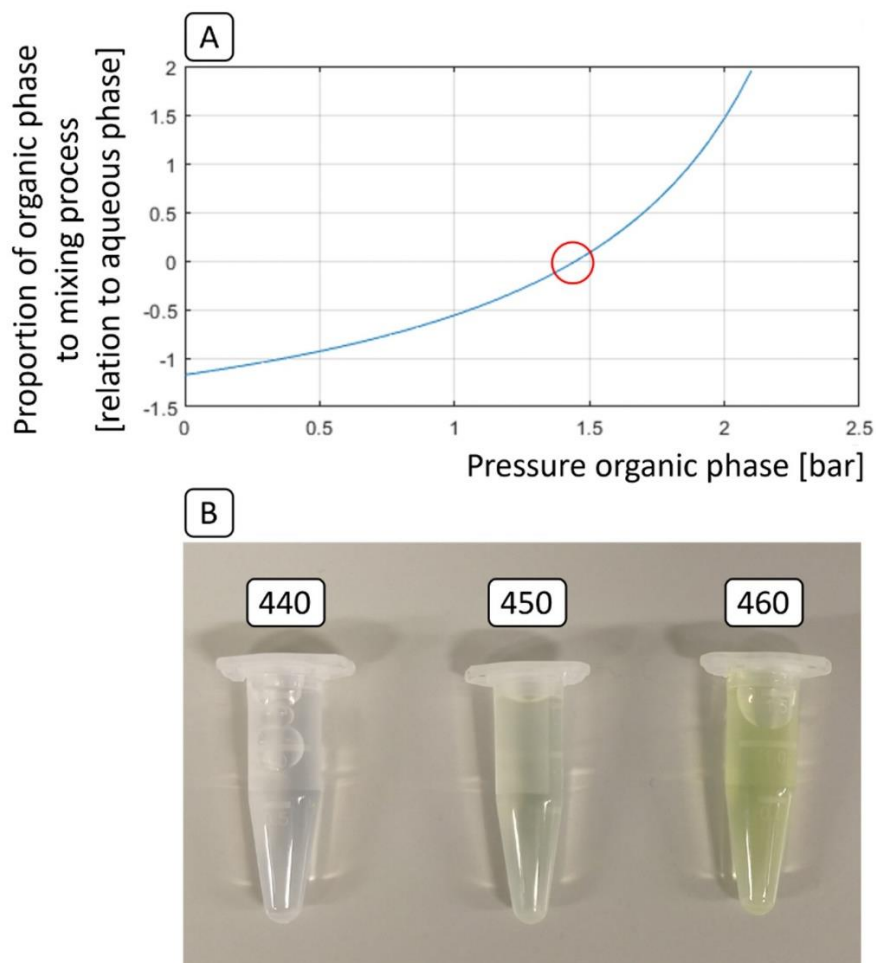


Fig. 3.14. A) Equilibrium pressure calculated by MATLAB to apply 450 mbar on the organic (acetonitrile) phase for withstanding the pressure of the aqueous phase (1000 mbar) without getting pushed back. This results in no contribution of organic phase to the mixing process. B) Applied 450 mbar to the organic and yellow-colored phase results in a slightly yellow colored mixture. Applied 440 mbar to the organic phase showed now yellow coloring at all due to a reverse flow in the acetonitrile capillary and with this no PLGA and curcumin contribution to the mixture. Applied 460 mbar to the organic phase showed a strongly yellow colored mixture resulting from contribution of organic phase to the mixing process.

Onstream supervision of the production process

By adding a microscope to the setup, the mixing process inside of the microfluidic chip could be monitored during the precipitation process. As shown in Fig. 3.15 a jet consisting of the organic phase (center) fed into the aqueous phase (left and right) is occurring. Any changes in mixing behavior like jet instabilities, jet shifting to the left or right, or entire blocking of capillaries could be detected immediately. Relying on a fast detection interfering aggregates of particle material can be dissolved directly by pulsing solvent into the mixing area.

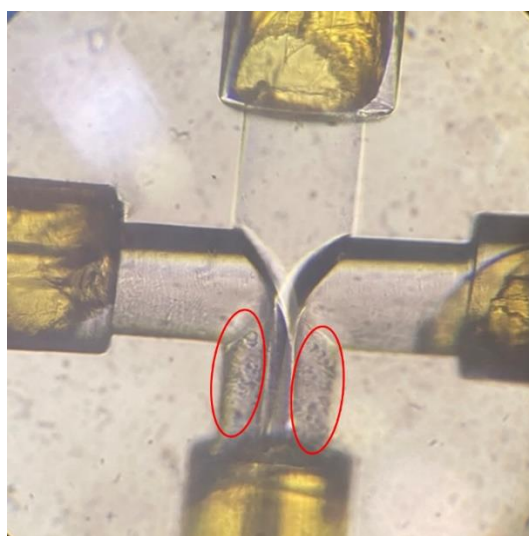


Fig. 3.15. Example for onstream monitoring of the precipitation process in the microfluidic chip. The jet appears stable, but first precipitates start to stick to the outlet channel borders (visible dark objects in the lower part of the cross-shaped area marked in red).

Particle purification using the Centrisart system

Particle purification based on the Centrisart system was carried out successfully. By applying relatively low centrifugal forces (200 g) to the system aggregation tendencies of particles could be reduced effectively. In most of the performed purification runs no pellet was formed at the bottom of the outer tube. If a pellet was forming, it was easy to redisperse by vortexing the sample. This is highly beneficial for the purification of sticky particles which cannot be purified using conventional centrifugation methods [30]. A sample volume of 2.5 mL loaded into the Centrisart system resulted in 100 to 200 μL concentrated nanosuspension after the centrifugation process. Dispersant could pass through the membrane and was collected successfully in the inner tube. The ability to reduce the volume of the particle suspension during purification is especially suited for highly diluted nanosuspensions how they are often produced by microfluidic systems. A PLGA content of 3 mg mL^{-1} in the organic phase for microfluidic nanoprecipitation as it is described previously is much lower compared to concentrations used for benchtop produced PLGA nanosuspensions ($10 - 15 \text{ mg mL}^{-1}$) [28,29].

Particle retention efficiency and permeation of the stabilizer during purification

Intensity measurements of the calibration series of curcumin loaded PLGA particles revealed that just dilutions containing 25%, 10% and 1% showed a linear behavior between fluorescence intensity and particle content (see Fig. 3.16). From this linearity a calibration function could be extracted:

$$\text{particle content [\%]} = \frac{\text{intensity} + 257.79}{631.39}$$

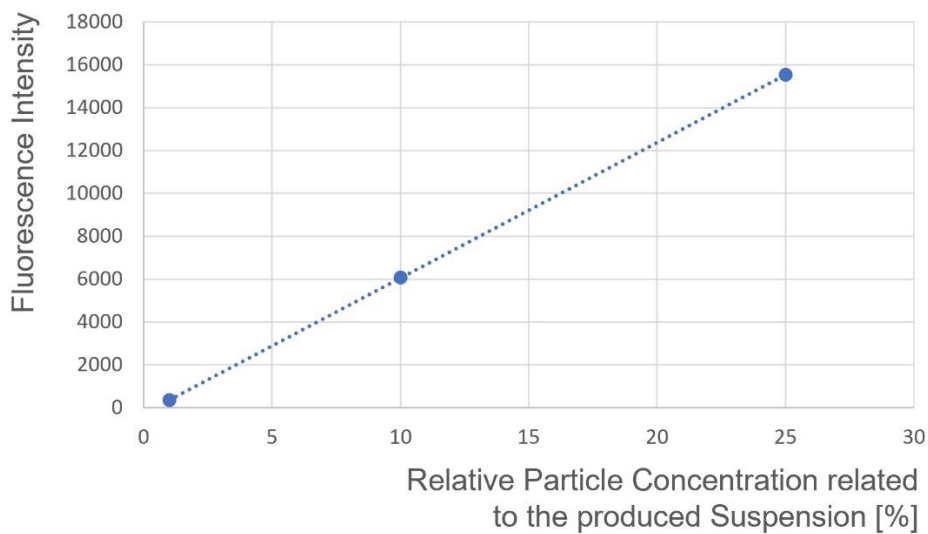


Fig. 3.16. Calibration for the investigation of particle retention efficiency of the Centrisart purification system. Suspensions containing 25%, 10% and 1% of the original suspension follow a linear decrease in fluorescence intensity. Concentrations larger than 25% lack a linear correlation. (Error bars are too small for visualization in the graph). $R^2 = 1$

After purification of three identical (to the calibration suspensions) manufactured samples the measured fluorescence intensity of the filtrate was divided by the intensity of the non-purified suspension. This resulted in a percentage of particles passing the membrane. This procedure was done to normalize the intensity of the filtrate to the intensity of the original suspension to equalize intensity fluctuations between the produced samples. The average particle content passing the membrane during Centrisart purification was $0.73 \pm 0.18\%$ ($99.27 \pm 0.18\%$ could not pass the membrane). Due to this neglectable particle loss Centrisart purification could be considered as a very effective purification method when it comes to keep particle yields as high as possible. Even if the measured filtrate intensity was caused by free curcumin this would indicate an even lower particle leakage through the membrane further increasing the filtration effectivity.

However, it was also investigated if poloxamer 188 as a stabilizer could pass the membrane while centrifugation.

Fig. 3.17 displays all absorption values of analyzed poloxamer 188 concentrations of the calibration series showing a linearity as desired. From this linear behavior a calibration function was extracted:

$$c = \frac{\text{absorption} - 0.0178}{0.346}$$

Where c is the poloxamer 188 concentration in mg mL^{-1} .

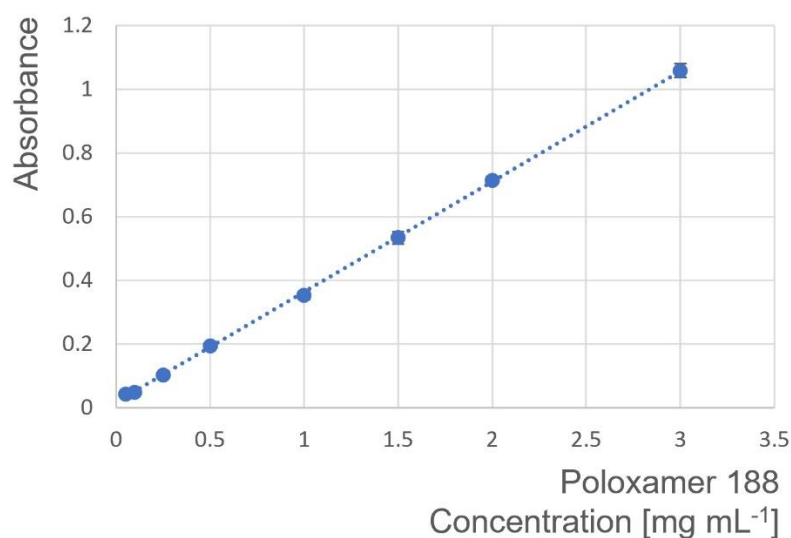


Fig. 3.17. Calibration for poloxamer 188 quantification based on the absorption of the formed cobalt(II) poloxamer 188 complex. $R^2 = 0.99$.

Absorption values of samples taken from the filtrates and from the original produced suspensions were measured. By dividing the filtrate value by the original suspension value, the percentage of poloxamer 188 passing the membrane was calculated. After particle purification the filtrates contained a **$76.86 \pm 16.32\%$** of the original poloxamer 188 concentration.

It can be concluded that larger amounts of the stabilizer could pass through the membrane. Nevertheless, the Centrisart purification process was holding back a certain amount of roughly 25% in the yielded sample. However, the purification process utilizing Centrisarts could be repeated for a single sample if it is necessary to remove most of the stabilizer molecules from the dispersion.

3.3.3 Further manufactured particle systems based on different polymers using the improved setup

3.3.3.1 Methods

Microfluidic manufacturing of gelatin nanoparticles

Gelatin nanoparticles were considered as an interesting platform particle system. They can be utilized as a carrier for a huge variety of drug substances (doxorubicin, clotrimazole, ciclosporin, and many more) [6]. Especially when it comes to macromolecules gelatin particles are vastly suited for this purpose [31]. Consequently, a production using microfluidics could enhance their applicability further.

For microfluidic particle preparation using the improved setup two solutions were prepared. The first solution contained gelatin dissolved in Milli-Q water (1 mg mL^{-1}) as particle material. The second solution contained poloxamer 188 dissolved in acetone (1 mg mL^{-1}) as a stabilizer. Microfluidic gelatin particle manufacturing relied on nanoprecipitation whereas aqueous and organic phases are switched in their roles in this preparation. Acetone as the organic and lipophilic phase represents the nonsolvent for gelatin as a hydrophilic particle material. By changing the roles of solvent and non-solvent during precipitation the orientation of aqueous and organic phase was switched inside of the chip as well. Consequently, the organic phase was fed into the chip from the sides and the aqueous one from the central position. The precipitation followed the same physical principles as described previously (see particle manufacturing using the initial microfluidic setup) and was carried out exactly as described earlier for the improved microfluidic setup. Mixing of both solutions resulted this time in a very lipophilic phase caused by the flow rate ratio of 10% aqueous phase and 90% organic phase. In this lipophilic phase gelatin was not soluble anymore and precipitated as nanoparticles.

Preliminary benchtop manufacturing of composite nanoparticles based on DEAE dextran and dextran sulfate

As an alternative to the previously shown PLGA or gelatin-based systems nanoparticles based on DEAE-dextran and dextran sulfate were investigated. This particle production was based on complex coacervation which can be considered as a special type of nanoprecipitation [7]. Complex coacervation relies on polymers presenting oppositely charged functional groups (amino functions in DEAE-dextran and sulfate groups in dextran sulfate) [7]. The single polymers are soluble in a selected solvent if they are separated from each other. By bringing them together oppositely charged functional groups start to form ion pairs which leads to an equalization of the charges and a significant loss in water solubility. Due to the decreased solubility the polymers start to precipitate in nanoparticles [7].

It was intended to influence the zeta potential of the particles either to a positive or negative charge by varying the polymer ratio in the particle. The positive charging of amino functions in DEAE-dextran and the negative charging of sulfate groups in dextran sulfate were exploited for this purpose. With this a system should be established which is suited for carrying more hydrophilic molecules and especially molecules presenting one or more charges. Tuning the zeta potential should ensure a drug loading via electrostatic interactions.

For preliminary benchtop experiments solutions of DEAE-dextran in Milli-Q water (1.9 mg mL⁻¹, 2.1 mg mL⁻¹, 2.3 mg mL⁻¹, 2.5 mg mL⁻¹, 2.7 mg mL⁻¹) and dextran sulfate in Milli-Q water (1 mg mL⁻¹) were prepared. The mentioned DEAE-dextran concentrations were selected by a rough estimation of the quantity of functional groups (amino groups versus sulfate groups) and their equalization in numbers. Each concentration of DEAE-dextran was mixed with the dextran sulfate solution by mixing 1 mL of both.

Microfluidic manufacturing of composite nanoparticles based on DEAE dextran and dextran sulfate

Based on the mentioned preliminary experiments composite nanoparticles were produced using the improved microfluidic setup. A negative zeta potential was intended for this particle batch. DEAE-dextran and dextran sulfate were dissolved in Milli-Q water to a concentration of 1 mg mL⁻¹. Since both solutions were aqueous and both containing particle material the decision which solution was pumped from the sides into the chip was based on the polymer amount to be fed into the chip (previously the solution containing particle material was fed over the center into the chip). Relying on the mentioned preliminary experiments a negative zeta potential should be achieved by mixing 2 parts DEAE-dextran and 1 part dextran sulfate. Since both solutions showed a polymer concentration of 1 mg mL⁻¹ a larger volume of the DEAE-dextran solution was required compared to dextran sulfate which resulted in the decision to feed DEAE-dextran from the sides into the microfluidic chip. The precipitation process with respective viscosity measurements and pressure calculation was carried out as previously described for PLGA and gelatin particles.

Manufacturing of composite nanoparticles based on DEAE dextran and double-stranded RNA (dsRNA)

Based on the previously obtained data the developed composite nanoparticle system was utilized for the delivery of double-stranded ribonucleic acid (dsRNA). The principle of complex coacervation was used again by keeping DEAE-dextran and switching from dextran sulfate to dsRNA. Instead of the negatively charged sulfate groups of dextran sulfate the negatively charged phosphate groups of the dsRNA backbone were used for ion pair formation with the positively charged amino functions of DEAE-dextran [11]. DEAE-dextran was kept intentionally due to its transfecting properties [32]. The mixing

ratio was kept identical to the precursor particle system at 2 parts DEAE-dextran and 1 part dsRNA. Aqueous solutions of both were prepared to a concentration of 0.5 mg mL^{-1} for DEAE-dextran and 1 mg mL^{-1} for the dsRNA. Achieving a mass ratio of 2 parts DEAE-dextran and 1 part dsRNA a volume ratio of 4 parts DEAE-dextran and 1 part dsRNA was used for particle preparation. Due to required nanosuspension volumes of several mL the precipitation process was carried out benchtop wise instead of utilizing microfluidics to economize the production time.

Formulation of a delivery system for the transfection of *Paramecium tetraurelia*

Manufacturing of dsRNA / DEAE-dextran composite nanoparticles was carried out for developing a delivery system transferring dsRNA into *Paramecium* to induce an RNA interference targeting different mRNAs in the microorganism for down-regulation of specific genes. However, a drawback of the system was the low particle size. Zetasizer data could show a stable nanosuspension in a size range of $\sim 100 \text{ nm}$. This size was not suited for an effective uptake by *Paramecium* [33].

Therefore, bacteria were used as a carrier. Manufactured particles were loaded on the outer membranes of *E. coli* (Bacterial strain: *Escherichia coli* DSM 498b, drug sensitive) which resulted in a delivery system providing the desired size. Relying on the positive charge of manufactured dsRNA / DEAE-dextran particles they were fixed electrostatically on the negative charged bacterial surfaces [34]. The assumed negative charge of the used *E. coli* strand was confirmed by a zeta potential measurement with the Zetasizer Ultra (knowing that bacteria do not show a suitable size range for this measurement). By loading the particles on bacteria, a delivery system should be created being considered as typical food by *Paramecium* [35]. With this the physiological uptake of nutrients into *Paramecium* was exploited for delivering dsRNA into the cell.

The samples for transfection were produced by washing the bacterial strain two times in phosphate buffered saline (PBS) and collecting the bacteria by centrifugation. $50 \mu\text{L}$ of the produced particle suspension were mixed with 1 mL of the bacterial suspension and incubated for 30 min at 37°C under shaking (180 rpm).

Simultaneously, to the sample containing the previously mentioned composite particles a second sample was produced identically containing fluorescein isothiocyanate (FITC)-tagged dsRNA for particle visualization on bacteria.

Characterization of the produced particle systems

Particle size measurements were carried out by using the Zetasizer Ultra and transmission electron microscopy (TEM).

Zetasizer sample preparations for different particle suspensions are summarized in the following. $100 \mu\text{L}$ of the gelatin nanoparticle suspension were diluted with $900 \mu\text{L}$

acetone inside of a quartz cuvette. 100 μL of all five benchtop manufactured nanosuspensions based on DEAE-dextran and dextran sulfate were mixed with 900 μL of Milli-Q water and filled in a measurement cell suited for zeta potential measurements. The sample preparation for microfluidic manufactured nanosuspensions based on DEAE-dextran and dextran sulfate was carried out identical compared to the benchtop produced suspensions. 50 μL of the nanosuspension based on DEAE-dextran and dsRNA were diluted with 600 μL of Milli-Q water and transferred to a zeta potential measurement cell. All prepared samples in different cuvettes were analyzed in backscatter mode.

For gelatin particles, microfluidic produced DEAE-dextran / dextran sulfate particles, and DEAE-dextran / dsRNA particles TEM samples were prepared. The sample preparation was identical for all. Undiluted particle suspension was drop casted on carbon coated copper grids. Liquid components of the dispersion evaporated over a short time while leaving a layer of particles on the grid. Additional staining was not required for particle visualization. TEM micrographs were recorded using a JEOL JEM-2100 in bright-field mode with a slow-scan charge-coupled device camera Gatan Orius SC1000. Operating voltage was set to 200 kV.

Zeta potential measurements were carried out for all DEAE-dextran / dextran sulfate particle suspensions, for DEAE-dextran / dsRNA particles, and for *E. coli* bacteria. The dilutions already used for size measurements were characterized again using the Zetasizer Ultra focusing on zeta potential. *E. coli* bacteria were characterized by diluting 100 μL of the bacterial suspension with 900 μL Milli-Q water and analyzing this dilution in a zeta potential measurement cell. Measuring the zeta potential relies on laser-doppler anemometry as it is explained in chapter two.

Bacteria (*E. coli*) with attached FITC-tagged DEAE-dextran / dsRNA particles were characterized by fluorescence and bright-field microscopy. For this visualization 10 μL were separated from the suspension and transferred to a microscope slide. The utilized microscope was a BZ810 from Keyence Deutschland GmbH, Neu-Isenburg, Germany.

3.3.3.2 Results and discussion

Microfluidic manufactured gelatin nanoparticles

The microfluidic manufacturing of gelatin nanoparticles was carried out successfully. Zetasizer data showed a z-average of 118 nm and a PDI of 0.182 which can be considered as a very well defined and monodisperse gelatin nanoparticle collective in the desired size range. Those data could be confirmed by the obtained TEM micrographs shown in Fig. 3.18. The displayed particles appear in a size range matching the predicted size by the Zetasizer Ultra. TEM images show larger amounts of grey sprinkles around the gelatin particles shown in black / dark grey. This is caused by remaining stabilizer (poloxamer 188) in the sample due to no preceding purification

of the particles. It can be concluded that the improved microfluidic system is well usable to produce gelatin nanoparticles as the desired platform particle system.

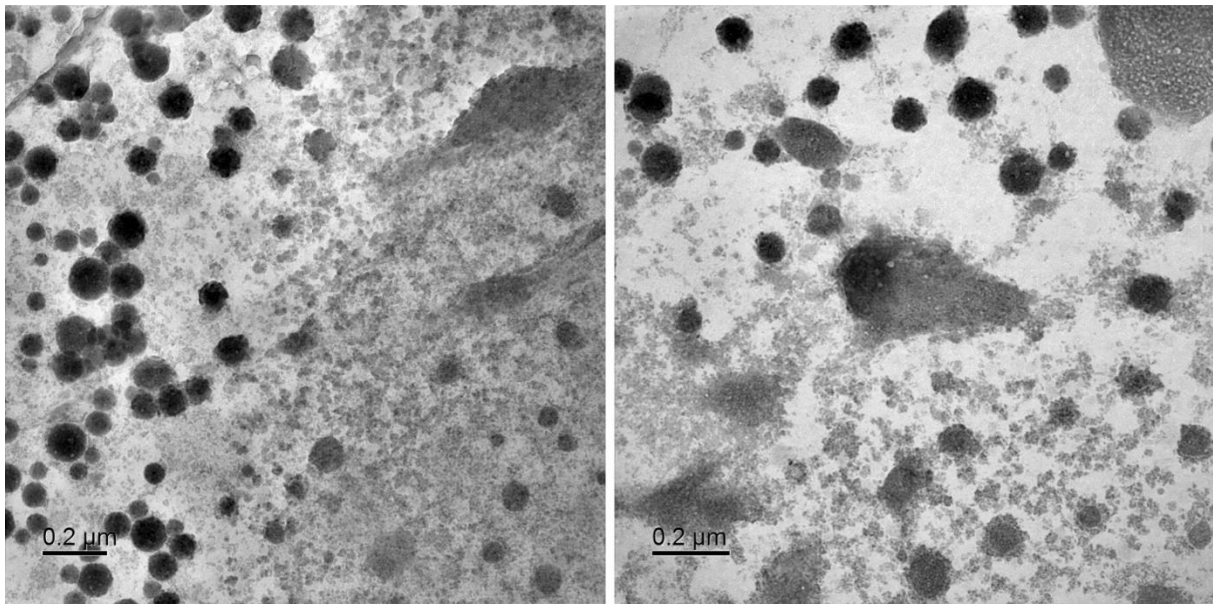


Fig. 3.18. TEM micrographs of gelatin nanoparticles produced with the microfluidic setup. Gelatin particles appear as black dots. Grey sprinkles and shades are caused by non-removed stabilizer (poloxamer 188).

Preliminary benchtop manufactured composite nanoparticles based on DEAE dextran and dextran sulfate

The benchtop production of DEAE-dextran / dextran sulfate composite nanoparticles in different mixing ratios led to nanosuspensions showing different stabilities. Since, the samples “- -” and “+ +” resulted in stable nanosuspensions the ratios “-“, “0”, and “+” (see table 3.1) were less stable (see Fig. 3.19). A lower stability was identified by a high turbidity and some larger visible agglomerates. The stable suspensions appeared clearer and showed opalescence as it would be expected from a colloidal dispersion [2]. Zetasizer data verified this visual assumption. Particle sizes, PDI, and respective zeta potential are shown in table 3.1. Furthermore, samples “- -” and “+ +” showed identical z-average values after one week which was not the case for the other suspensions which showed a large increase in particle size within this period.

Table 3.1 Zetasizer data of the produced composite nanoparticle suspensions based on different polymer mixing ratios.

Sample icon	- -	-	0	+	+ +
DEAE-dextran	1.9 mg/mL	2.1 mg/mL	2.3 mg/mL	2.5 mg/mL	2.7 mg/mL
Dextran sulfate	1 mg/mL	1 mg/mL	1 mg/mL	1 mg/mL	1 mg/mL
Z-average	151	256	17.600 μm	190 nm	146 nm
PDI	0.104	0.053	0.852	0.052	0.106
Zeta potential	-26 mV	-20 mV	-2 mV	+18 mV	+23 mV



Fig. 3.19. Visual appearance of the produced DEAE-dextran / dextran sulfate composite nanosuspensions. “+ +” indicates the highest measured zeta potential (2.7 mg mL⁻¹ DEAE-dextran) and “- -” the lowest (1.9 mg mL⁻¹ DEAE-dextran). The colloidal stability is decreasing the closer the zeta potential is moved towards zero. An unstable nanosuspension is indicated by a much higher turbidity (see the central vial).

A lower stability of suspensions “-“, “0“, and “+” could be explained by the respective zeta potentials. By bringing the zeta potential value closer to zero repulsive forces based on electrostatics decrease vastly which results in a strong increase in agglomeration tendency. A zeta potential of roughly +25 mV or -25 mV seems to be necessary for stabilizing the suspension electrostatically. Concluding that, a ratio of 1.9 parts DEAE-dextran to 1 part dextran sulfate and 2.7 parts DEAE-dextran to 1 part dextran sulfate led to benchtop produced particles in desired size ranges (~150 nm) which were electrostatically stabilized and could be used as a platform particle system for delivering hydrophilic drugs.

Microfluidic manufactured composite nanoparticles based on DEAE dextran and dextran sulfate

Based on the preliminary benchtop experiments the manufacturing of composite DEAE-dextran / dextran sulfate nanoparticles was transferred to the improved

microfluidic setup. As previously predicted a ratio of 2 parts DEAE-dextran and 1 part dextran sulfate should result in negatively charged particles. The microfluidic production of those particles was carried out successfully and could reproduce this trend. A zeta potential of -35 mV could be measured for this particle collective as well as a z-average of 161 nm and a PDI of 0.195. Particle sizes predicted by the Zetasizer Ultra could be confirmed by the TEM micrographs of the manufactured particles in Fig. 3.20. Concluding, the developed particle system as a platform particle system for delivering hydrophilic drugs could be transferred to microfluidic manufacturing without any drawbacks while delivering a well-defined and homogeneous particle suspension in the desired size range.

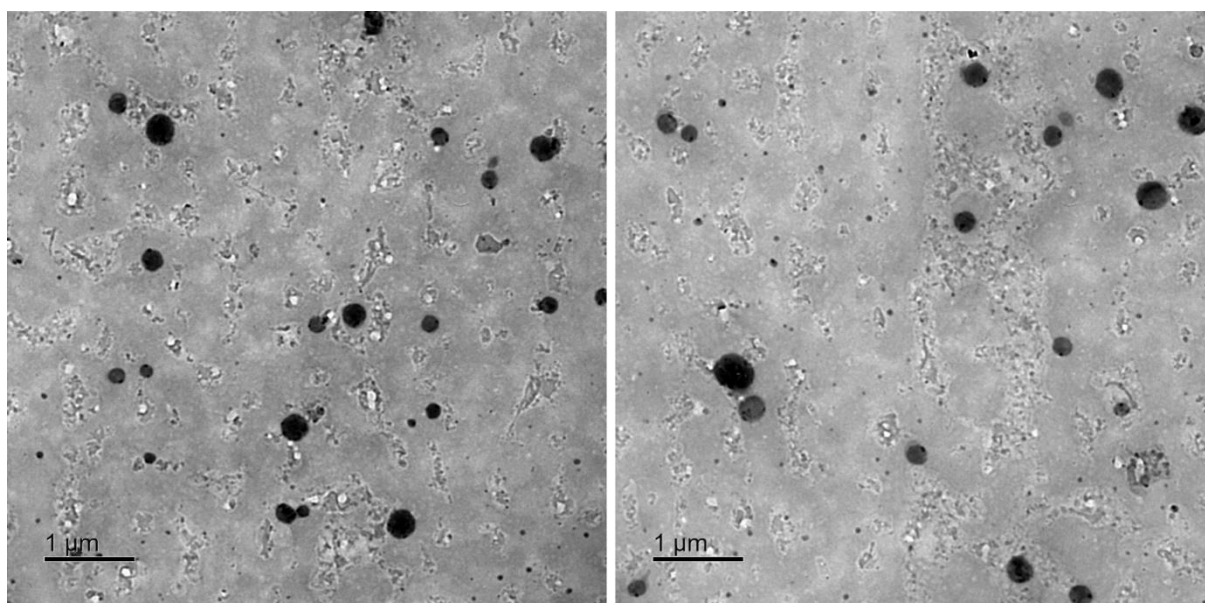


Fig. 3.20. TEM micrographs of DEAE-dextran / dextran sulfate composite nanoparticles produced with the microfluidic setup.

Composite nanoparticles based on DEAE dextran and double-stranded RNA (dsRNA)

Utilizing the previously introduced platform particle system consisting of dextran-based composite nanoparticles this system was exploited for the delivery of dsRNA. By changing previously used dextran sulfate to dsRNA the genetic material was directly incorporated into the particles by electrostatic interactions. A ratio of 2 parts DEAE-dextran and 1 part dsRNA led to positively charged particles within a stable nanosuspension (monitored over one week: no size increase) showing a zeta potential of +9 mV. A z-average value of the particles measured by the Zetasizer Ultra was found to be 115 nm while showing a PDI of 0.162. The particle size could be verified by TEM micrographs shown in Fig. 3.21.

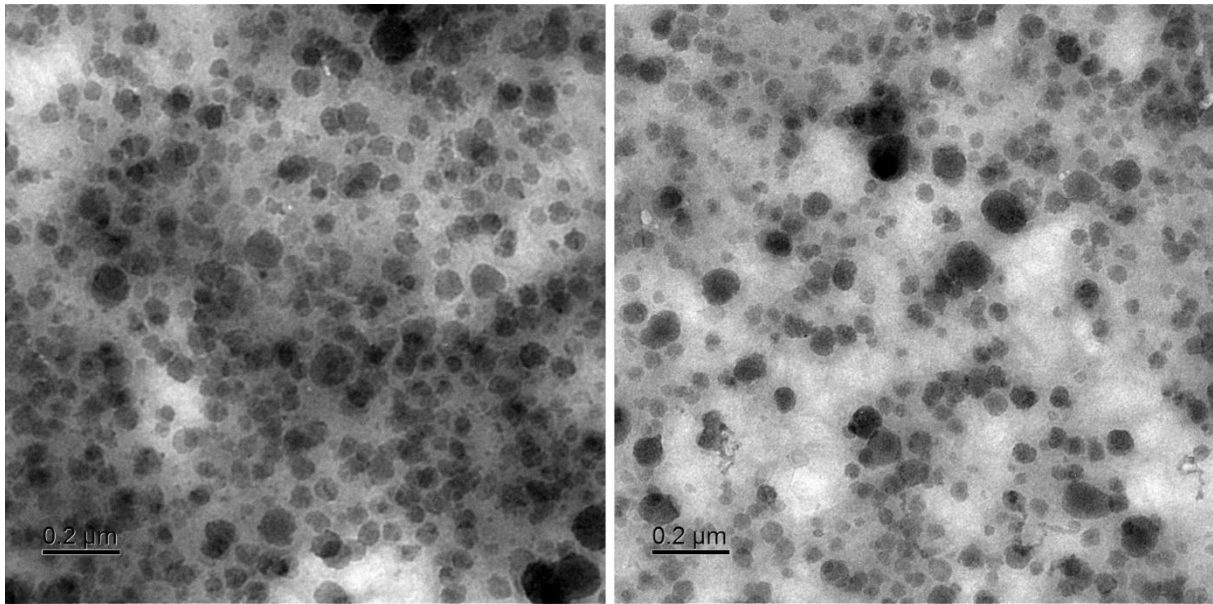


Fig. 3.21. TEM micrographs of DEAE-dextran / dsRNA composite nanoparticles produced with the microfluidic setup. Grey shades are caused by non-removed and excess DEAE-dextran. It was used during the precipitation in excess guaranteeing a positive particle charge. Surplus DEAE-dextran in the sample is not considered as an issue being a transfection agent and showing the potential for enhancing the dsRNA uptake [32].

Concluding this data, the particle production could be considered successful. Nevertheless, particles show small sizes which are not suitable for the uptake by *Paramecium*. Due to this fact the produced particles were loaded on larger carriers for a sufficient transfection of the microorganisms.

***E. coli*-based delivery system including composite nanoparticles**

By incubating the produced nanoparticles based on DEAE-dextran and dsRNA with *E. coli* the negative surface charge of the bacteria attracted the positively charged particles (+9 mV) leading to particle assembly on the bacteria. This behavior could be shown in Fig. 3.22. A zeta potential measurement of the utilized *E. coli* strand resulted in -14 mV. This value supports the literature-based assumption of negatively charged bacterial surfaces [34] well knowing that measured bacteria are not perfectly suited for the measurement device due to their size. Nevertheless, this result still provides a reference to the real surface charge being sufficient for estimating a positive or negative charge at all. Fig. 3.22 localizes the used bacteria in bright-field mode. By combining bright-field mode and fluorescence mode FITC-tagged particles can be colocalized directly on the bacteria by detecting the emitted fluorescence signal. This proved that the electrostatic interaction between particles and *E. coli* could be effectively exploited for loading the particles on bacteria to form a larger delivery system. Aiming for the ideal case the loaded bacteria could be considered as food by *Paramecium* which would even enhance the cellular uptake. Concluding, the

successful preparation of the desired dsRNA delivery system based on particles loaded on bacteria as a larger carrier could be shown.

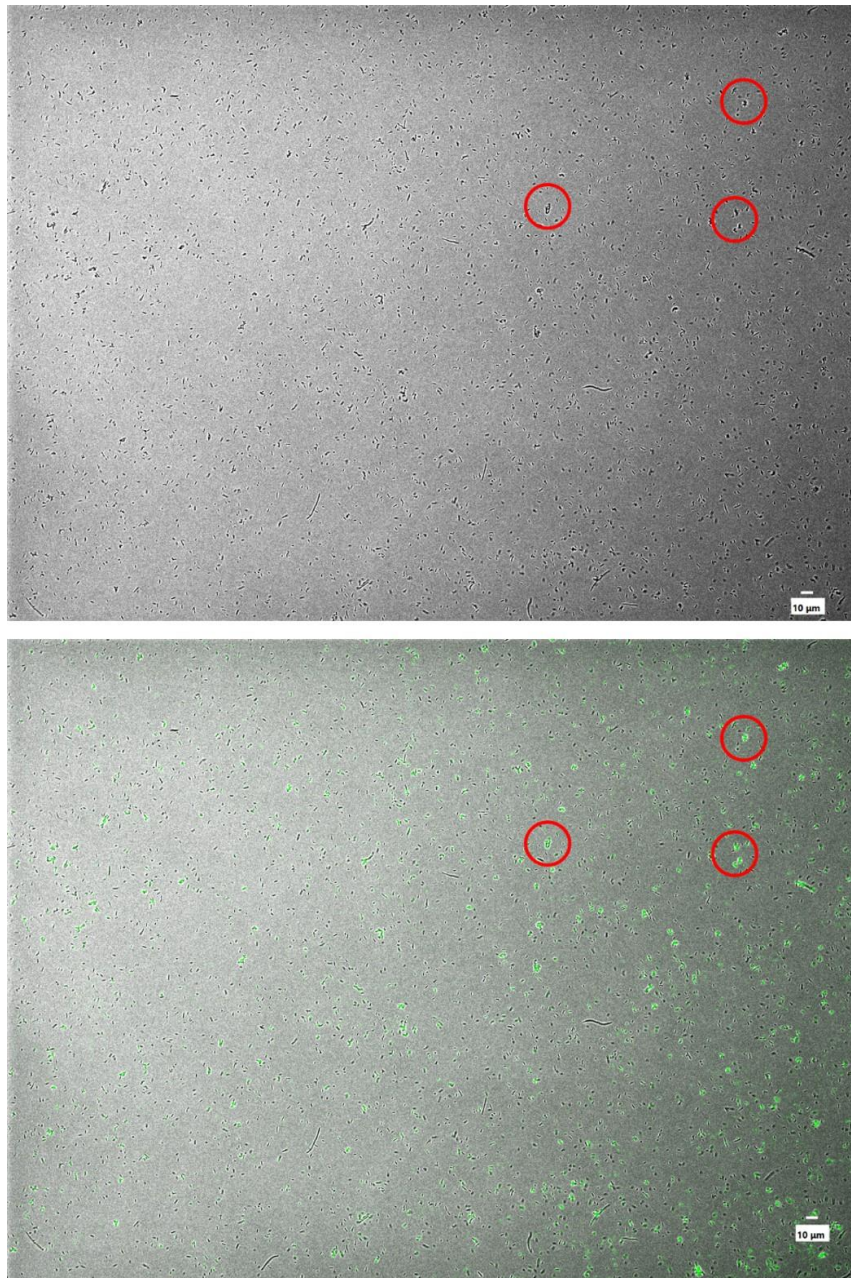


Fig. 3.22. Top: *E. coli* with attached and FITC-tagged particles visualized in bright-field mode. Bottom: Bright-field mode combined with fluorescence mode. Particles appear as green dots attached to bacterial surfaces. Red circles are giving examples for identical areas of the sample with and without additional fluorescence mode.

Yet, it must be mentioned that preliminary experiments could show that a stable nanosuspension of composite DEAE-dextran / dsRNA nanoparticles starts agglomerating immediately after the addition of PBS (bacteria were suspended in PBS). Consequently, it was assumed that the particle system forms aggregates during

the attachment process on bacterial surfaces. Nevertheless, the distribution of the particles' fluorescence to many bacteria is obvious. Since *Paramecium* take up larger objects it is questionable if this agglomeration is a drawback at all. Adsorbed particles as well as bacteria-sized agglomerates might be well internalized by *Paramecium*. The attachment to the bacteria does not appear to be hindered by the agglomeration which ensures the quality of the intended delivery system.

Evaluation of the data

It could be shown that different types of nanoparticulate systems could be produced utilizing the improved microfluidic system. All systems could be produced successfully and in desired size ranges making them great platform systems for further improvement and specialization in drug delivery. Especially, the DEAE-dextran / dextran sulfate-based system could be exploited for developing a delivery system for dsRNA by overhauling the already established formulation to the desired requirements. This dsRNA delivery system was a great example for investigating a suitable formulation using microfluidics for keeping batches small and material waste low and subsequently scaling up to benchtop manufacturing for producing larger amounts of the required system. All data show that the improved microfluidic system can be used to produce a large variety of nanoparticle systems and is a very robust method especially when it comes to guaranteeing very precise flow rate ratios during the precipitation process resulting in particle formation with low polydispersity. By ensuring precise flow rate ratios the charge of composite particles could be tuned very precisely to the respective requirements.

3.4 References

- [1] S. Balbach, C. Korn, Pharmaceutical evaluation of early development candidates “the 100 mg-approach,” *Int J Pharm.* 275 (2004) 1–12. <https://doi.org/10.1016/J.IJPHARM.2004.01.034>.
- [2] A. Fahr, Voigt Pharmazeutische Technologie, Voigt Pharmazeutische Technologie. (2022). <https://doi.org/10.52777/9783769277487>.
- [3] N. Lababidi, V. Sigal, A. Koenneke, K. Schwarzkopf, A. Manz, M. Schneider, Microfluidics as tool to prepare size-tunable PLGA nanoparticles with high curcumin encapsulation for efficient mucus penetration, *Beilstein Journal of Nanotechnology.* 10 (2019) 2280–2293. <https://doi.org/10.3762/BJNANO.10.220>.
- [4] N. Lababidi, C.V. Montefusco-Pereira, C. de Souza Carvalho-Wodarz, C.M. Lehr, M. Schneider, Spray-dried multidrug particles for pulmonary co-delivery of antibiotics with N-acetylcysteine and curcumin-loaded PLGA-nanoparticles, *European Journal of Pharmaceutics and Biopharmaceutics.* 157 (2020) 200–210. <https://doi.org/10.1016/J.EJPB.2020.10.010>.
- [5] A.V. Weiss, T. Fischer, J. Iturri, R. Benitez, J.L. Toca-Herrera, M. Schneider, Mechanical properties of gelatin nanoparticles in dependency of crosslinking time and storage, *Colloids Surf B Biointerfaces.* 175 (2019) 713–720. <https://doi.org/10.1016/J.COLSURFB.2018.12.005>.

- [6] N. Sahoo, R.K. Sahoo, N. Biswas, A. Guha, K. Kuotsu, Recent advancement of gelatin nanoparticles in drug and vaccine delivery, *Int J Biol Macromol.* 81 (2015) 317–331. <https://doi.org/10.1016/J.IJBIOMAC.2015.08.006>.
- [7] C.E. Sing, S.L. Perry, Recent progress in the science of complex coacervation, *Soft Matter.* 16 (2020) 2885–2914. <https://doi.org/10.1039/D0SM00001A>.
- [8] S. Bhattacharjee, DLS and zeta potential – What they are and what they are not?, *Journal of Controlled Release.* 235 (2016) 337–351. <https://doi.org/10.1016/J.JCONREL.2016.06.017>.
- [9] J. Hierrezuelo, A. Sadeghpour, I. Szilagyi, A. Vaccaro, M. Borkovec, Electrostatic stabilization of charged colloidal particles with adsorbed polyelectrolytes of opposite charge, *Langmuir.* 26 (2010) 15109–15111. <https://doi.org/10.1021/LA102912U>.
- [10] A.R. Studart, E. Amstad, L.J. Gauckler, Colloidal stabilization of nanoparticles in concentrated suspensions, *Langmuir.* 23 (2007) 1081–1090. <https://doi.org/10.1021/LA062042S>.
- [11] C. Siewert, H. Haas, T. Nawroth, A. Ziller, S.S. Nogueira, M.A. Schroer, C.E. Blanchet, D.I. Svergun, A. Radulescu, F. Bates, Y. Huesemann, M.P. Radsak, U. Sahin, P. Langguth, Investigation of charge ratio variation in mRNA – DEAE-dextran polyplex delivery systems, *Biomaterials.* 192 (2019) 612–620. <https://doi.org/10.1016/J.BIOMATERIALS.2018.10.020>.
- [12] H.K. Makadia, S.J. Siegel, Poly Lactic-co-Glycolic Acid (PLGA) as biodegradable controlled drug delivery carrier, *Polymers.* 3 (2011) 1377–1397. <https://doi.org/10.3390/polym3031377>.
- [13] J.A. Loureiro, M.C. Pereira, PLGA Based Drug Carrier and Pharmaceutical Applications: The Most Recent Advances, *Pharmaceutics.* 12 (2020) 903. <https://doi.org/10.3390/PHARMACEUTICS12090903>.
- [14] F. Danhier, E. Ansorena, J.M. Silva, R. Coco, A. le Breton, V. Pr at, PLGA-based nanoparticles: An overview of biomedical applications, *Journal of Controlled Release.* 161 (2012) 505–522. <https://doi.org/10.1016/J.JCONREL.2012.01.043>.
- [15] K.K. Chereddy, V.L. Payen, V. Pr at, PLGA: From a classic drug carrier to a novel therapeutic activity contributor, *Journal of Controlled Release.* 289 (2018) 10–13. <https://doi.org/10.1016/J.JCONREL.2018.09.017>.
- [16] W. Huang, C. Zhang, Tuning the size of poly(lactic-co-glycolic acid) (PLGA) nanoparticles fabricated by nanoprecipitation, *Biotechnol J.* 13 (2018). <https://doi.org/10.1002/BIOT.201700203>.
- [17] C.J. Mart nez Rivas, M. Tarhini, W. Badri, K. Miladi, H. Greige-Gerges, Q.A. Nazari, S.A. Galindo Rodr guez, R. . Rom n, H. Fessi, A. Elaissari, Nanoprecipitation process: From encapsulation to drug delivery, *Int J Pharm.* 532 (2017) 66–81. <https://doi.org/10.1016/J.IJPHARM.2017.08.064>.
- [18] S. Ding, N. Anton, T.F. Vandamme, C.A. Serra, Microfluidic nanoprecipitation systems for preparing pure drug or polymeric drug loaded nanoparticles: an overview, *Expert Opin Drug Deliv.* 13 (2016) 1447–1460. <https://doi.org/10.1080/17425247.2016.1193151>.
- [19] C. Lourenco, M. Teixeira, S. Sim es, R. Gaspar, Steric stabilization of nanoparticles: Size and surface properties, *Int J Pharm.* 138 (1996) 1–12. [https://doi.org/10.1016/0378-5173\(96\)04486-9](https://doi.org/10.1016/0378-5173(96)04486-9).
- [20] R.B. Miles, W.R. Lempert, J.N. Forkey, Laser Rayleigh scattering, *Meas Sci Technol.* 12 (2001) R33. <https://doi.org/10.1088/0957-0233/12/5/201>.
- [21] P.F. Gao, G. Lei, C.Z. Huang, Dark-Field Microscopy: Recent Advances in Accurate Analysis and Emerging Applications, *Anal Chem.* 93 (2021) 4707–4726. <https://doi.org/10.1021/ACS.ANALCHEM.0C04390>.

- [22] Min Hu, Carolina Novo, Alison Funston, Haining Wang, Hristina Staleva, Shengli Zou, Paul Mulvaney, Younan Xia, G. V. Hartland, Dark-field microscopy studies of single metal nanoparticles : understanding the factors that influence the linewidth of the localized surface plasmon resonance, *J Mater Chem.* 18 (2008) 1949–1960. <https://doi.org/10.1039/B714759G>.
- [23] D. Primavessy, N. Günday Türeli, M. Schneider, Influence of different stabilizers on the encapsulation of desmopressin acetate into PLGA nanoparticles, *European Journal of Pharmaceutics and Biopharmaceutics.* 118 (2017) 48–55. <https://doi.org/10.1016/j.ejpb.2016.12.003>.
- [24] R.R. Kotha, D.L. Luthria, Curcumin: Biological, Pharmaceutical, Nutraceutical, and Analytical Aspects, *Molecules.* 24 (2019) 2930. <https://doi.org/10.3390/MOLECULES24162930>.
- [25] C.F. Chignell, P. Bilskj, K.J. Reszka, A.G. Motten, R.H. Sik, T.A. Dahl, Spectral and Photochemical Properties of Curcumin, *Photochem Photobiol.* 59 (1994) 295–302. <https://doi.org/10.1111/J.1751-1097.1994.TB05037.X>.
- [26] Y. Mao, M.J. Thompson, Q. Wang, E.W. Tsai, Quantitation of poloxamers in pharmaceutical formulations using size exclusion chromatography and colorimetric methods, *J Pharm Biomed Anal.* 35 (2004) 1127–1142. <https://doi.org/10.1016/J.JPBA.2004.04.010>.
- [27] S.L. Marusin, Sample preparation — the key to SEM studies of failed concrete, *Cem Concr Compos.* 17 (1995) 311–318. [https://doi.org/10.1016/0958-9465\(95\)00020-D](https://doi.org/10.1016/0958-9465(95)00020-D).
- [28] J.M. Barichello, M. Morishita, K. Takayama, T. Nagai, Encapsulation of Hydrophilic and Lipophilic Drugs in PLGA Nanoparticles by the Nanoprecipitation Method, *Drug Dev Ind Pharm.* 25 (1999) 471–476. <https://doi.org/10.1081/DDC-100102197>.
- [29] T. Govender, S. Stolnik, M.C. Garnett, L. Illum, S.S. Davis, PLGA nanoparticles prepared by nanoprecipitation: drug loading and release studies of a water soluble drug, *Journal of Controlled Release.* 57 (1999) 171–185. [https://doi.org/10.1016/S0168-3659\(98\)00116-3](https://doi.org/10.1016/S0168-3659(98)00116-3).
- [30] N. Nafee, M. Schneider, U.F. Schaefer, C.M. Lehr, Relevance of the colloidal stability of chitosan/PLGA nanoparticles on their cytotoxicity profile, *Int J Pharm.* 381 (2009) 130–139. <https://doi.org/10.1016/J.IJPHARM.2009.04.049>.
- [31] A. Baseer, A. Koenneke, J. Zapp, S.A. Khan, M. Schneider, Design and Characterization of Surface-Crosslinked Gelatin Nanoparticles for the Delivery of Hydrophilic Macromolecular Drugs, *Macromol Chem Phys.* 220 (2019) 1900260. <https://doi.org/10.1002/MACP.201900260>.
- [32] T. Gulick, Transfection Using DEAE-Dextran, *Curr Protoc Mol Biol.* 40 (2001) 9.2.1-9.2.10. <https://doi.org/10.1002/0471142727.MB0902S40>.
- [33] T. Fenchel, Suspension feeding in ciliated protozoa: Functional response and particle size selection, *Microb Ecol.* 6 (1980) 1–11. <https://doi.org/10.1007/BF02020370>.
- [34] W.W. Wilson, M.M. Wade, S.C. Holman, F.R. Champlin, Status of methods for assessing bacterial cell surface charge properties based on zeta potential measurements, *J Microbiol Methods.* 43 (2001) 153–164. [https://doi.org/10.1016/S0167-7012\(00\)00224-4](https://doi.org/10.1016/S0167-7012(00)00224-4).
- [35] I. Barna, D.S. Weis, The utilization of bacteria as food for *Paramecium bursaria.*, *Trans Am Microsc Soc.* 92 (1973) 434–440. <https://doi.org/10.2307/3225247>.

Chapter 4

Parameters influencing drug encapsulation

Contributions to the chapter:

Methodology, experimental design, data analysis, calculations, and result interpretations of all experimental data were done by the author of the thesis.

Particle preparation, characterization, and drug loading quantification measurements were performed by Taha Al Ani.

4.1 Introduction: Parameters influencing drug encapsulation

Focusing on drug encapsulation in polymer-based nanoparticles it is desirable to keep the overall drug loading as high as possible. For the sake of an effective therapy the ratio between drug and carrier should be as high as possible to carry much drug substance with low amounts of polymer. It is reasonable to reduce the amount of carrier substance due to reducing the overall amount of needed formulation and to exclude side effects caused by the carrier as much as possible [1]. For instance, keeping the overall needed amount of drug formulation small can become advantageous with regard to inhalable formulations. Here the inhalable amounts are limited preventing irritations of the respiratory tract while inhalation of dry powders [2].

Preliminary experiments indicated that the choice of the stabilizing agent providing a homogeneous nanosuspension and preventing agglomeration seems to highly influence the encapsulated amount of drug substance in the particle during the production process (see Fig. 4.1).

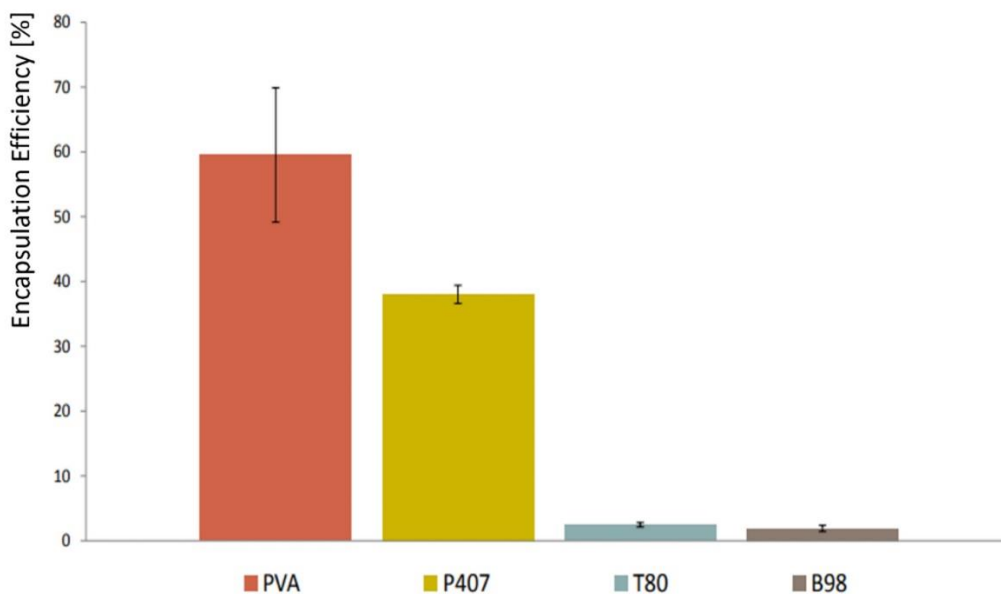


Fig. 4.1. Preliminary loading experiments show the different encapsulation efficiency of curcumin in PLGA nanoparticles for four different stabilizers: Polyvinyl alcohol (PVA), poloxamer 407 (P407), Tween 80 (T80) and Brij 98 (B98). Each mass concentration: 1 mg mL⁻¹.

As drug substance curcumin was used. Curcumin is a great model substance due to its physicochemical properties. It is highly lipophilic ($\log P = 3.6$ [3]) which makes it well comparable to many recently developed drug substances and it is fluorescent making it easy to detect and to quantify [4,5]. Furthermore, its lipophilic properties are in line

with the physicochemical properties of poly(lactic-co-glycolic acid) (PLGA) used as particle material. Dissolution of the drug in the polymer solution should be feasible [6].

PLGA as particle material was selected regarding its widespread use [7–10] and its biodegradability (see. Fig. 4.2) [6,11]. Very low toxicity making PLGA very popular for a wide use in many different fields [9,11]. Besides, nanoparticle manufacturing based on PLGA is extensively described in literature [6–8,11] and is straight-forward making it very suitable for a larger number of encapsulation experiments resulting in many different formulations for comparison.

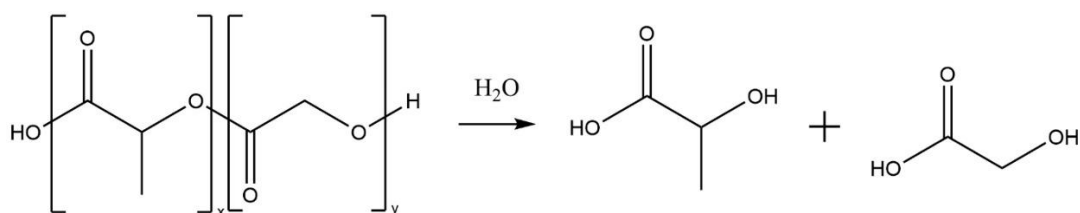


Fig. 4.2. Degradation of PLGA to lactic acid and glycolic acid.

For further investigation regarding the encapsulation of curcumin into PLGA nanoparticles different stabilizers were chosen. Different parameters with a potential influence on the overall drug loading were screened. The focus was on the type of the stabilizer, hydrophilic lipophilic balance (HLB) value of the respective stabilizer [12–14], and stabilizer concentration.

For a fast production of nanosuspensions and to analyze the influence of the respective stabilizer particles were benchtop manufactured by a nanoprecipitation method [15]. This appears contradictory to the previous chapter focusing on a microfluidic particle manufacturing for keeping the batches as small as possible but is highly necessary in this chapter conserving a high throughput for a straight-forward production of many different formulation samples. To quantify the curcumin loading particles were precipitated and purified by centrifugation steps. Afterwards, the curcumin-loaded particles were dissolved, and the curcumin amount was quantified by fluorescence measurements.

Finally, the release of curcumin from the produced PLGA nanoparticles was investigated to collect information about the localization of the substance in the particle (burst release from the surface or sustained release from the inside) which can be influenced by the stabilizer as well. The question is if the stabilizer can enhance the drug loading as described for double emulsions. As mechanism for the impact the interaction of the drug with the stabilizer or a simple accumulation of drug on the particle surface might be considered (Fig. 4.3) [16].

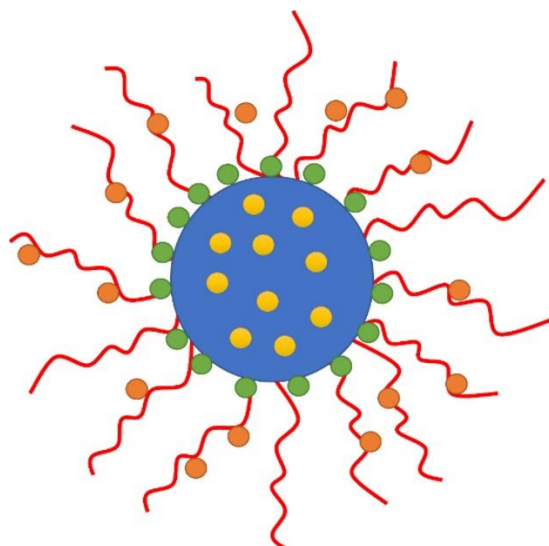


Fig. 4.3. Schematic image of a nanoparticle (blue circle) with attached stabilizer (red lines), drug substance dispersed inside of the particle material (yellow dots), drug substance loaded on the surface of the particle (green dots), and drug substance interacting with the stabilizer molecules (orange dots).

4.2 Materials

PLGA (Resomer RG 503H) was purchased from Evonik Industries AG, Essen, Germany. Acetonitrile was obtained from Fisher Scientific GmbH, Schwerte, Germany. The purification system Millipore, Milli-Q Synthesis, Merck, Darmstadt, Germany provided pure water. Curcumin, Span 20, 40, 60, 80, and 85, Tween 85, and Brij 93 were purchased from Sigma Aldrich, Taufkirchen, Germany. Poly(vinyl alcohol) (PVA) (Mowiol 4-88) was obtained from Kuraray Europe GmbH, Hattersheim am Main, Germany. Tween 80 and poloxamer 407 were purchased from Caesar & Loretz GmbH, Hilden, Germany. Brij 98 was purchased from Fisher Scientific GmbH, Schwerte, Germany. Pluronic (Poloxamer) PE 10100, PE 6200, PE 4300, PE 9400, and PE 10500 were purchased from BASF SE, Ludwigshafen, Germany. Poloxamer 188 was obtained from AppliChem GmbH, Darmstadt, Germany. Phosphate-buffered saline (PBS) was produced in-house containing sodium chloride, potassium dihydrogen phosphate, potassium chloride, and disodium hydrogen phosphate. Sodium chloride (99.5%) and potassium dihydrogen phosphate were obtained from Grüssing GmbH, Filsum, Germany. Potassium chloride was purchased from Caesar & Loretz GmbH, Hilden, Germany, and disodium hydrogen phosphate was obtained from Merck, Darmstadt, Germany.

4.3 Model particle system for optimization studies

4.3.1 Particle preparation

4.3.1.1 Methods

Benchtop particle preparation

As preliminary work for benchtop nanoprecipitation the organic and aqueous phases were produced first. The organic phase was prepared by dissolving PLGA and curcumin together in acetonitrile to a concentration of 16.89 mg mL^{-1} for PLGA and $0.0167 \text{ mg mL}^{-1}$ for curcumin. These values resulted from dissolving 250 mg PLGA in 15 mL acetonitrile and mixing 14.75 mL of this solution with 0.25 mL of a curcumin solution (1 mg mL^{-1}). The aqueous phase was produced by dissolving a stabilizer in Milli-Q water. Stabilizer type and concentration were changed from experiment to experiment. A typical example would be an aqueous PVA solution in a concentration of 5 mg mL^{-1} . Different from nanoprecipitation carried out by microfluidics as already described in chapter three, here both phases were mixed benchtop using a magnetic stirrer (see Fig. 4.4) and injecting the organic phase in the aqueous phase using a syringe pump (Legato 210, kdScientific, Holliston, Massachusetts, USA). 1.5 mL of the organic phase were pumped into 10 mL aqueous phase holding a feeding rate of 0.5 mL min^{-1} . Since water and acetonitrile can be dissolved in each other a new aqueous phase is resulting during the mixing process. The relatively small volume of acetonitrile does not influence the overall hydrophilicity to a greater extent. As already described in chapter three PLGA and curcumin show a low solubility in the resulting phase and precipitate in the form of nanoparticles with stabilizer molecules on the surface. During this precipitation curcumin accumulating inside of PLGA nanoparticles is highly desired.



Fig. 4.4. Preparation of PLGA nanoparticles using a syringe pump.

Particle purification

Manufactured nanoparticles were purified for separating non-assembled particle material and non-loaded drug substance from final particles. This was carried out by using a centrifugation-based purification method. The used centrifuge was a Multifuge X1R from Thermo Scientific, Waltham, Massachusetts, USA. After preliminary experiments suitable centrifugation settings were found and applied to all forthcoming particle purifications. For purification 10 mL of Milli-Q water were added to the respective sample. The diluted nanosuspension was transferred into a 50 mL Falcon Tube (Cellstar Tubes, Greiner Bio-One GmbH, Frickenhausen, Germany) and centrifuged at 4000 g for 15 min at 20°C. The supernatant was discarded, and the pellet was redispersed in 10 mL Milli-Q water by shaking, vortexing, and if necessary ultrasonic treatment for a few seconds (Elmasonic P from Elma Schmidbauer GmbH, Singen, Germany). Subsequently, the nanosuspension was centrifuged once more at 3000 g for 10 min at 20°C. Again, the supernatant was discarded, and the obtained pellet was redispersed in 1 mL Milli-Q water by shaking, vortexing, and short ultrasonic treatment if necessary. Finally, the resulting nanosuspension was suited for further analytical steps.

Particle characterization

In terms of particle size and particle size distribution analytical investigations were carried out including scanning electron microscopy (SEM) and dynamic light scattering (DLS). The physically background and explanation of the respective methods are

already highlighted in chapter two. SEM is a straight-forward way to measure the geometrical diameter of particles [17].

Preparation of SEM samples was carried out by fixing a fragment of a silica wafer via a carbon disc on a SEM sample holder. Subsequently, the purified nanosuspension was drop-casted on the surface of the silica wafer. After an incubation of roughly 20 seconds at room temperature the liquid was removed by a tissue touching the suspension droplet (exploiting capillary forces) to leave particles on the silica surface. SEM images were captured using an EVO HD15 by Zeiss, Jena, Germany, after the sample was gold sputtered [18].

DLS sample preparation was carried out by diluting 5 μL of the purified nanosuspension with 995 μL of Milli-Q water and transferring this diluted nanosuspension into a polystyrene cuvette. DLS measurements were performed by using the Zetasizer Ultra from Malvern Panalytical GmbH, Kassel, Germany.

4.3.1.2 Results and discussion

Benchtop nanoprecipitation for curcumin loaded PLGA particles was performed successfully. The resulting nanosuspensions appeared homogeneous without visible agglomerates. During the particle purification process while applying harsh centrifugation conditions (10,000 g, 30 min) a non-redispersible pellet occurred for some samples. Optimization of the purification process by lowering the centrifugal forces as earlier described (4,000 g, 15 min, and 3,000 g, 10 min) led to redispersible pellets. A drawback of this optimization was a lower particle yield. The supernatant showed a much higher turbidity compared to samples with harsher centrifugation conditions. Obviously, many particles were not forced into the pellet under the adjusted conditions and were discarded with the supernatant. The Stokes' law serves for explanation.

$$v = \frac{2}{9} * \frac{r^2 * (\rho_P - \rho_D) * g}{\eta}$$

Where v is the sedimentation velocity, r is the radius of the particle, ρ_P is the density of the particle, ρ_D is the density of the dispersant, g is the gravitational field strength, and η is the dynamic viscosity [14].

Obviously, by reducing centrifugal force and centrifugation time (3,000 g, 10 min) especially smaller particles are not collected in the pellet as it can be concluded from r and g in the equation and the resulting reduced sinking velocity in addition to the reduced sedimentation time which was provided for the particle to pass the Falcon tube to its bottom.

Nevertheless, this does not affect the purpose of the experiment. Focusing on drug loading in further experiments the overall particle yields are not crucial. The key question is how much drug substance is incorporated in the collected particles. And

the ability to manufacture and purify particles in a simple and straightforward manner is of greater significance.

According to captured SEM micrographs obtained particles appear in the desired size range. Most of the particles are ranging between 100 nm and 200 nm and just few particles showing a diameter up to ~500 nm (see Fig. 4.5).

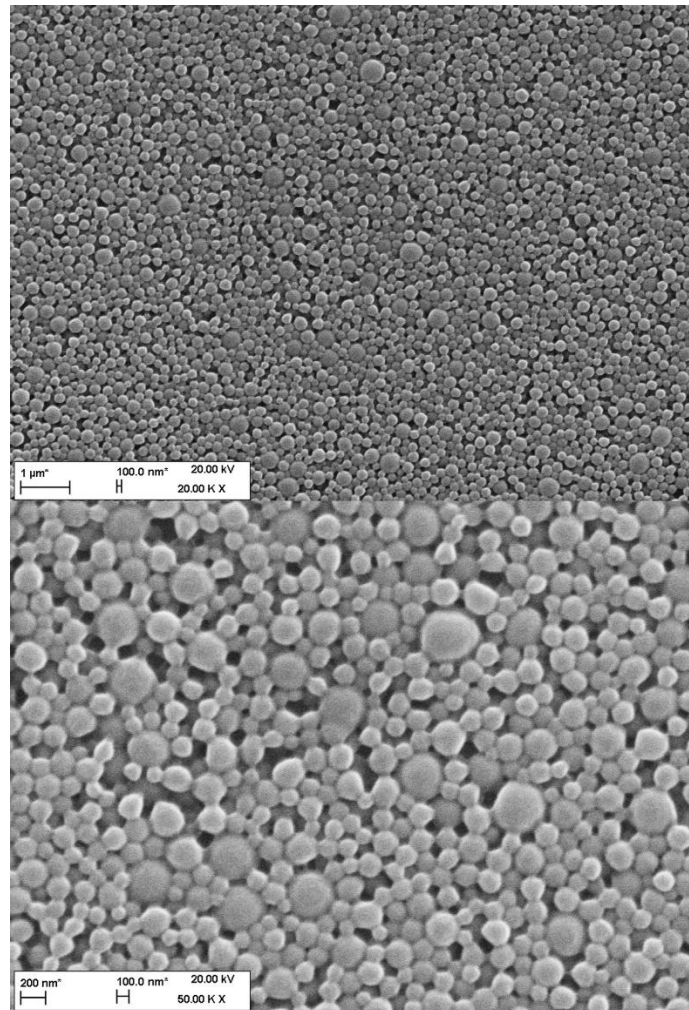


Fig. 4.5. SEM micrographs of curcumin loaded PLGA nanoparticles. The shown particle collective is a representative sample in the series of following drug loading experiments.

These results were supported by DLS data displaying a peak maximum around 200 nm in the intensity distribution. The number distribution shows a slight shift to smaller particle sizes which perfectly fits to the SEM obtained particle sizes keeping in mind that larger particles have a higher impact on the scattering intensity leading to a more prominent proportion in the distribution [19], whereas in the number distribution the quantity of particles in respective size ranges is the deciding factor (Fig. 4.6). SEM micrographs displayed a higher quantity of smaller particles compared to larger particles. This could be confirmed in the DLS number distribution.

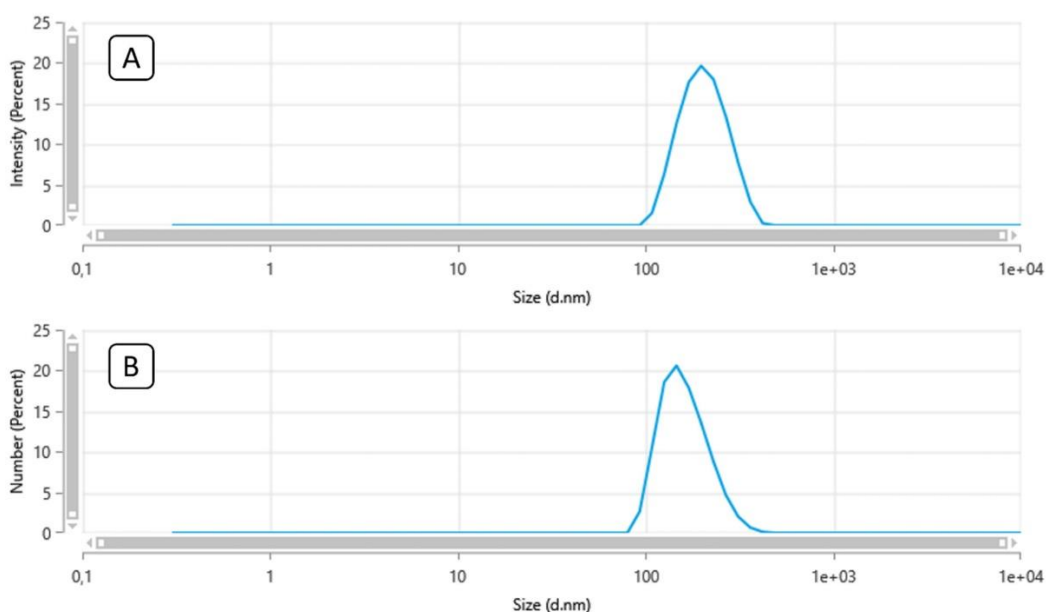


Fig. 4.6. A) Particle size intensity distribution of curcumin loaded PLGA nanoparticles. It is clearly visible that the suspension contains no larger agglomerates. Otherwise, they would appear in the intensity distribution. B) Particle size number distribution of the same particles showing the particle size which occurs most frequently.

4.3.2 Influence of the stabilizer on the encapsulation efficiency

4.3.2.1 Methods

Selection of the stabilizers

Investigating the influence of different stabilizers on drug encapsulation into nanoparticles different representatives were considered for particle production. Considered stabilizers originated from the following groups: Span, Tween, Brij, PVA, and poloxamer. The respective candidates from the groups with their structural formulas are displayed in figures 4.7, 4.8, 4.9, 4.10 and 4.11. An exact knowledge of the molecular structure of the respective stabilizers is crucial for a precise HLB calculation.

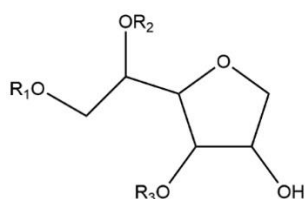


Fig. 4.7. Basic structure of Span. R₁, R₂, and R₃ are differing between the types. **Span 85**: R₁, R₂, R₃ = oleic acid; **Span 80**: R₁ = oleic acid, R₂, R₃ = H; **Span 60**: R₁ = stearic acid, R₂, R₃ = H; **Span 40**: R₁ = palmitic acid, R₂, R₃ = H; **Span 20**: R₁ = lauric acid, R₂, R₃ = H.

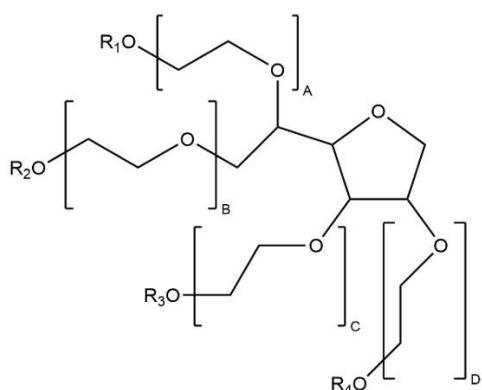


Fig. 4.8. Basic structure of Tween. **Tween 80**: 20 units in total for blocks A, B, C, and D and one oleic acid per molecule at one of R₁, R₂, R₃, or R₄; **Tween 85**: 20 units in total for blocks A, B, C, and D and three oleic acids per molecule at R₁, R₂, R₃, or R₄.

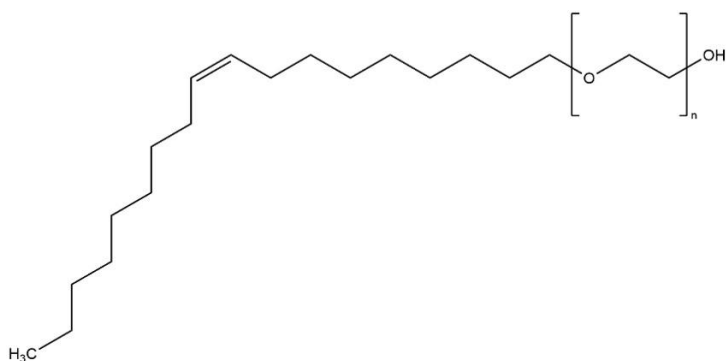


Fig. 4.9. Basic structure of Brij. The number of ethylene oxide units varies between the types. **Brij 93**: n = 2; **Brij 98**: n = 20.

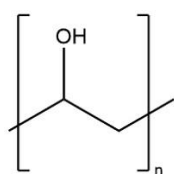


Fig. 4.10. Basic Structure of **PVA** (Mowiol 4-88): n ~ 700.

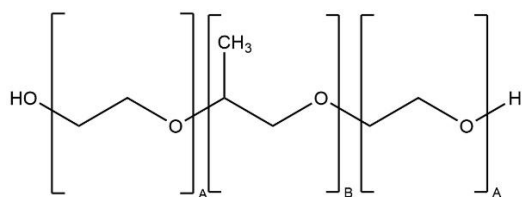


Fig. 4.11. Basic Structure of poloxamer. Number of units in A and B blocks for different investigated poloxamers: **PE 10100**: A = 8, B = 56; **PE 6200**: A = 10, B = 30; **PE 4300**: A = 10, B = 19; **PE 9400**: A = 31, B = 47; **Poloxamer 407**: A = 26, B = 30; **PE 10500**: A = 74, B = 56; **Poloxamer 188**: A = 159, B = 30.

It was intended to select stabilizers spread over the HLB scale [12–14,20] as wide as possible. This way, the influence of the HLB value among others on drug encapsulation can be investigated. The HLB value represents the hydrophilic and lipophilic portions of the molecule according to molecular weight giving information about how well the stabilizer is soluble in the respective phase and in terms of an emulsion which phase will result as the outer or inner phase [12–14].

Ionic stabilizers were excluded on purpose. Intentionally, electrostatic interactions representing another variable to influence the particle system should be excluded.

HLB calculation

For considered stabilizers (previously shown) not all HLB values were available in literature. Accordingly, they were obtained by using the Davies' method for calculation. Griffin's method [13,14] was not used intentionally due to a limitation in higher values to a maximum of 20 whereby some of the selected stabilizers are highly hydrophilic excluding them naturally from the Griffin scale. A great benefit of the method by Davies is the ability to classify highly hydrophilic stabilizers. The method relies on group numbers which are affiliated to functional groups in the molecule (see table 4.1). This leads to a very nuanced distribution over a wide spectrum not just relying on the ratio of hydrophilic to lipophilic molecular masses of the respective molecule and applying this ratio to a scale between 0 and 20 like it is done by Griffin [13,14].

The calculation of HLB values was performed using the following equation including values from table 4.1 [12,14,20]:

$$\text{HLB} = 7 + \Sigma \text{ hydrophilic group value} + \Sigma \text{ hydrophobic group value}$$

Table 4.1. Group values for calculating the HLB [12,14,20].

Hydrophilic groups	Attributed Value
-O-	1.3
Free -OH	1.9
Sorbitan -OH	0.5
-CH ₂ -CH ₂ -O-	0.35
Hydrophobic groups	Attributed Value
=CH-	-0.475
-CH ₂ -	-0.475
-CH ₃	-0.475
-CH(CH ₃)-CH ₂ -O-	-0.125

Particle preparation and purification

Particle manufacturing and subsequent purification was carried out exactly as described in 4.3.1.1. The only variables which were changed between the experiments were type and concentration of the used stabilizer. Screening water solubility of stabilizer candidates led to excluding all stabilizers showing an HLB value below the threshold value of Tween 85 from the following formulation experiments due to their poor solubility. Investigating the influence of the stabilizer's HLB value on the encapsulation efficiency the following stabilizers were included in the particle production process (each mass concentration: 5 mg mL⁻¹): PE9400, Brij 98, Tween 80, PVA, poloxamer 407, PE 10500. For further investigations the stabilizer showing the highest encapsulation efficiency was selected for obtaining its molar concentration from the utilized mass concentration (5 mg mL⁻¹). As a next step, samples were produced by using identical stabilizers but switching from an equalized mass concentration to an equalized molar concentration. Each stabilizer was used in the obtained molar concentration of 3.97*10⁻⁴ mol L⁻¹. The idea was to use for all preparations an equal number of stabilizer molecules and to compare the stabilizer's influence this way.

Focusing on the influence of molar concentration on encapsulation efficiency additional samples were included in the investigation. The six previously mentioned stabilizers were each analyzed additionally in molar concentrations of 2*10⁻⁴ mol L⁻¹ and 6*10⁻⁴ mol L⁻¹. Furthermore, Tween 85 and poloxamer 188 were included in the study also being analyzed in concentrations of 2*10⁻⁴ mol L⁻¹, 3.97*10⁻⁴ mol L⁻¹, and 6*10⁻⁴ mol L⁻¹.

Following detected encapsulation trends, all eight stabilizers investigated so far were tested in even lower molar concentrations. The sample sequence was enhanced by adding the following molar concentrations for each stabilizer: 0.25*10⁻⁴ mol L⁻¹, 0.5*10⁻⁴ mol L⁻¹, 0.75*10⁻⁴ mol L⁻¹, and 1*10⁻⁴ mol L⁻¹.

All produced samples were manufactured as triplicates, freeze dried, and subsequently analyzed via fluorescence intensity measurements quantifying curcumin content.

Fluorescence based quantification of the drug concentration

For quantification of the drug content in all produced samples an approach based on fluorescence intensity was selected. Measurements were performed by using a plate reader (Infinite M200, Tecan Deutschland GmbH, Crailsheim, Germany). By capturing absorbance and emission spectra utilizing the plate reader maximum wavelengths for fluorescence excitation and emission of curcumin were obtained. The respective spectra are displayed in Fig. 4.12.

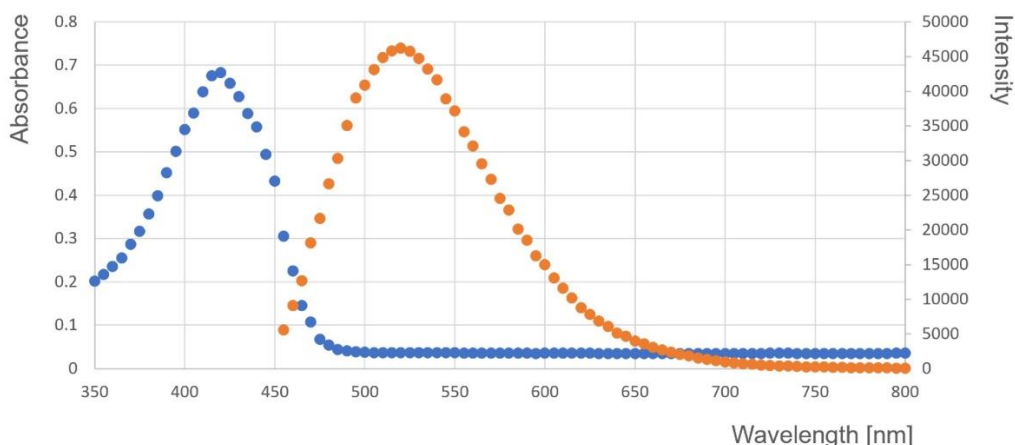


Fig. 4.12. Absorbance (blue) and fluorescence intensity (orange) spectra of curcumin in acetonitrile for identifying the wavelengths at the maxima in excitation (430 nm) and emission (515 nm).

For calibration of the curcumin quantification a concentration series of curcumin in acetonitrile was prepared and respective fluorescence intensities were measured at the fluorescence maximum (515 nm). For excitation a wavelength of 430 nm was utilized. Curcumin concentrations to be analyzed were set to $0.10 \mu\text{g mL}^{-1}$, $0.25 \mu\text{g mL}^{-1}$, $0.50 \mu\text{g mL}^{-1}$, $0.75 \mu\text{g mL}^{-1}$, and $1.00 \mu\text{g mL}^{-1}$ (see Fig. 4.13). Each concentration was prepared and quantified as a triplicate. Preliminary measurements could show that this corridor is suitable for a precise curcumin quantification under usable fluorescence intensities.

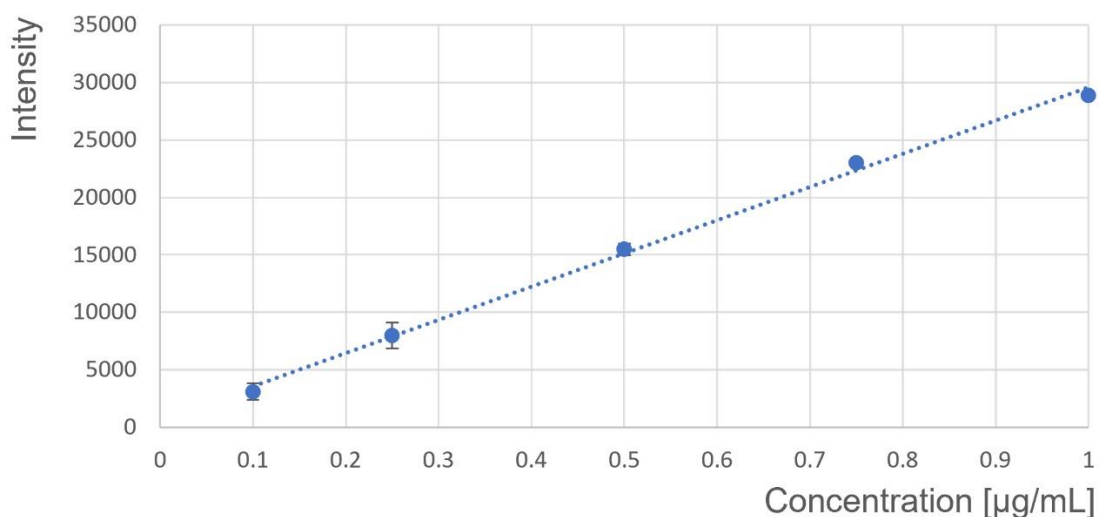


Fig. 4.13. Calibration for the quantification of curcumin in acetonitrile. Using this approach curcumin is well detectable in a concentration range between $0.10 \mu\text{g mL}^{-1}$ and $1.00 \mu\text{g mL}^{-1}$. Error bars representing standard deviations are too small for being displayed in some measurement triplicates. $R^2=0.9971$

Results from fluorescence intensity measurements shown in Fig. 4.13 indicate linearity between intensity values and curcumin concentrations as desired. Due to linearity a calibration function was obtained facilitating the quantification of curcumin concentration by fluorescence intensity measurements. The affiliated equation is shown below:

$$c = \frac{I - 676.89}{28877}$$

Where c ($\mu\text{g mL}^{-1}$) is the concentration value of curcumin in acetonitrile and I is the measured intensity value of the sample.

Quantification of drug loading and encapsulation efficiency

The amount of curcumin in a single sample was quantified by transferring the sample into a pre-tared Eppendorf reaction tube, freeze drying the purified sample, and determining the remaining mass of dried sample inside the reaction tube by measuring the total tube mass and subtracting the pre-tared mass. Freeze dried particles inside the reaction tube were again dissolved in 1000 μL acetonitrile for destruction of particles and liberation of incorporated curcumin into the solvent. Free curcumin was quantified in the solution by fluorescence intensity measurements as previously described. Fluorescence intensities too high to capture were reduced by diluting 100 μL of the sample solution with further 900 μL of acetonitrile. By measuring the contained curcumin concentration inside the dissolved samples and dividing it by the known sample volume the contained curcumin mass was received.

Encapsulation efficiency regarding the entire nanoparticle production was calculated using the following equation:

$$\text{encapsulation efficiency [\%]} = \frac{\text{curcumin in the purified particles [mg]}}{\text{utilized curcumin in the experiment [mg]}} * 100$$

Drug loading of curcumin inside nanoparticles was calculated using the following equation:

$$\text{drug loading [\%]} = \frac{\text{curcumin in the purified particles [mg]}}{\text{total mass of the purified particles [mg]}} * 100$$

Curcumin release study

In terms of capturing a release profile of manufactured curcumin loaded PLGA nanoparticles and to receive a better understanding of the localization of curcumin in the particle a drug release study was performed. Particles used in this study were manufactured using the microfluidic system from chapter three. Intentionally, investigated and developed methods were brought together. Particle manufacturing should be downscaled relying on microfluidics while applying the optimized formulation

for a maximum in drug loading while reducing the waste of drug material in total. Moreover, curcumin still was considered as a suitable model substance.

Concerning particle precipitation, the organic phase (acetonitrile) contained PLGA in a concentration of 9.8 mg mL^{-1} and curcumin in a concentration of 0.2 mg mL^{-1} . However, the curcumin proportion regarding particle material was highly increased to boost higher drug loadings in total supported by improved encapsulation conditions. The aqueous phase contained poloxamer 188 in a concentration of 1.67 mg mL^{-1} which corresponds to $2 \cdot 10^{-4} \text{ mol L}^{-1}$ being the stabilizer concentration which promised no decrease in drug loading according to previous experiments. The microfluidic mixing of both phases was performed in a 9 + 1 ratio meaning 9 parts of aqueous phase and 1 part of organic phase. After particle production the nanosuspension was purified using the Centrisart system (Centrisart 300,000 MWCO PES, Sartorius GmbH, Göttingen, Germany) as already mentioned in chapter three to yield as much particle material as possible. Curcumin content of the sample was quantified as previously introduced (lyophilization, weight determination, and fluorescence measurement). Using the known curcumin content, the applied curcumin mass for the release samples could be predicted.

As release medium phosphate-buffered saline (containing sodium chloride: 800 mg, potassium dihydrogen phosphate: 27 mg, potassium chloride: 20 mg, and disodium hydrogen phosphate: 178 mg dissolved in 100 mL Milli-Q water) with added Tween 80 (1 mg mL^{-1}) was used. Tween 80 was intentionally added as a solubilizer for curcumin maintaining a better release due to a higher saturation concentration in water [21]. Furthermore, preliminary experiments showed that curcumin degradation was decreased by adding Tween 80 as a solubilizer. It was assumed that curcumin inside of solubilizer micelles could be better protected from hydrolyzation and oxidative degradation.

Release medium (890 μL) and particle suspension (110 μL) were filled into Eppendorf reaction tubes. For each time point a separate reaction tube was prepared. Additionally, every time point was analyzed as a triplicate (respectively three reaction tubes). Release time points were 0 h, 1 h, 6 h and 24 h. Particles inside the release medium were incubated to the respective timepoints under shaking (100 rpm) at 37°C . After incubation, all Eppendorf reaction tubes (as well the tubes for time point 0 h) were centrifuged (Sigma 3-30KS from Sigma Laborzentrifugen GmbH, Osterode am Harz, Germany) using $40,000 \text{ g}$ for 30 min at 20°C to separate the supernatant containing free curcumin from the particles forming a pellet at the tubes' ground. Both, supernatant and pellet were analyzed in terms of curcumin content as already described before. To be precise, 500 μL supernatant of each sample were freeze dried and afterwards dissolved in 1000 μL acetonitrile. The pellets were freed from supernatant as effective as possible using a pipette, subsequently freeze dried and finally dissolved in 1000 μL acetonitrile. Both acetonitrile solutions were quantified regarding curcumin concentration.

Characterization of the sedimentation behavior of micelles formed by stabilizer molecules

Tween 80, poloxamer 407, and poloxamer 188 were separately dissolved in Milli-Q water to a concentration of 5 mg mL⁻¹ for each stabilizer. 50 mL of the respective stabilizer solution was filled into a Falcon Tube (Cellstar Tubes, Greiner Bio-One GmbH, Frickenhausen, Germany) and centrifuged (Multifuge X1R from Thermo Scientific, Waltham, Massachusetts, USA) at 20,000 g for 60 min at 20°C. After the centrifugation process the Falcon Tube was visually checked for a pellet assembled at the bottom.

4.3.2.2 Results and discussion

Selection of the stabilizers

To investigate the stabilizer's influence on drug encapsulation a selection of HLB values was made covering as much as possible of the HLB scale. Table 4.2 shows all selected stabilizers with associated values. HLB values not showing a reference were calculated using the Davies method relying on the structural information previously shown.

Table 4.2. Stabilizers for encapsulation efficiency investigation and their HLB values.

Stabilizer	HLB value
Span 85	1.8 [14]
Brij 93	4 [22]
Span 80	4.3 [14]
Span 60	4.7 [14]
PE 10100	5.4
Span 40	6.7 [14]
Span 20	8.6 [14]
PE 6200	9.2
PE 4300	10.9
Tween 85	11 [23]
PE 9400	14.5
Brij 98	15.6
Tween 80	16.4
PVA	18 [24]
PE F-127 (Poloxamer 407)	22 [25,26]
PE 10500	28.3
PE F-68 (Poloxamer 188)	29 [26]

All stabilizers from table 4.2 were tested for suitability in encapsulation experiments. A possible dissolution in the aqueous phase was crucial for nanoprecipitation. Stabilizers showing a HLB value smaller than Tween 85 were excluded from the investigation immediately. Concluding from preliminary experiments their water solubility was too low for being used in this context. Tween 85 showed the lowest HLB value in this row providing a water solubility usable for drug encapsulation experiments. As a result, Tween 85 and all stabilizers showing higher HLB values were included in the study. Their distribution over the HLB scale is shown in Fig. 4.14.

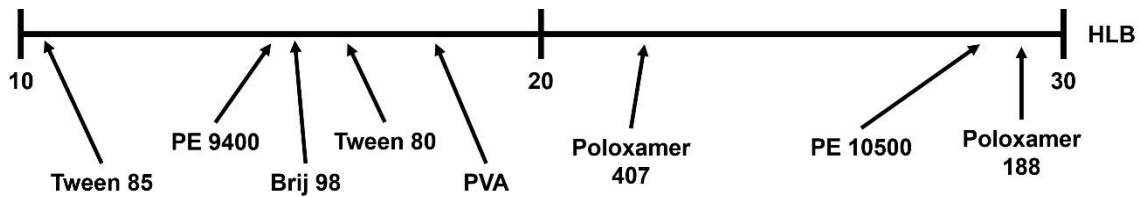


Fig. 4.14. Stabilizers which could be used for encapsulation efficiency investigation. The selection was made to cover the entire HLB range between 10 and 30 as well distributed as possible.

Drug encapsulation and the stabilizer's influence

Particle manufacturing was carried out successfully for all selected/chosen stabilizers as it was expected relating to previous experiments shown in 4.3.1. The utilized curcumin amount (0.1% of the PLGA mass) was kept low intentionally for keeping encapsulation efficiencies as high as possible and to make it easier to detect differences in influence on the encapsulation among different stabilizers in a system being not overloaded with drug substance. Assuming HLB values of respective stabilizers being the reason for different encapsulation efficiencies no trend could be found confirming this. As shown in Fig. 4.15 the encapsulation efficiency of curcumin into the manufactured PLGA particles increases or decreases randomly between the selected stabilizers (stabilizer concentration: 5 mg mL⁻¹). Stabilizers were listed from left to right according to HLB values starting with PE 9400 (HLB = 14.5) and ending with PE 10500 (HLB = 28.3). However, this data shows poloxamer 407 providing the most efficient encapsulation efficiency. Matching this observation, all other included poloxamer types (PE 9400 and PE 10500) tend to be close in encapsulation efficiency to poloxamer 407. PVA appears to be similarly effective whereas Brij 98 and Tween 80 are extremely ineffective in direct comparison. Nevertheless, similarities in encapsulation tend to appear fully independent from HLB values highlighted for example by poloxamer types being similar respecting encapsulation but widely spread over the HLB scale. Concluding from this comparison, no statement can be made regarding a specific parameter influencing encapsulation efficiency.

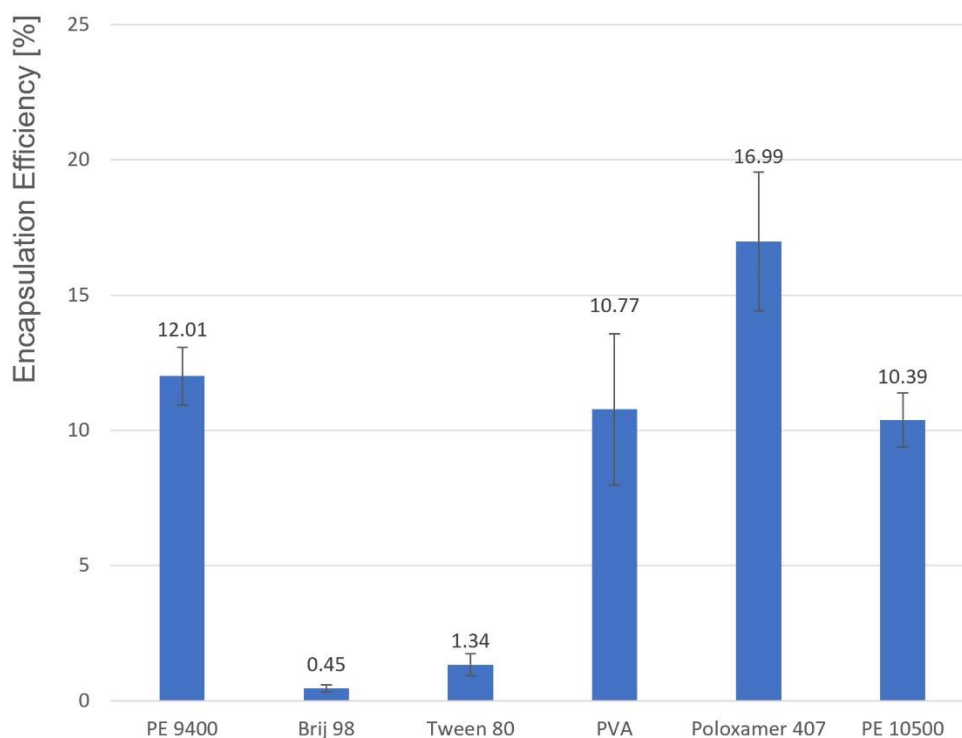


Fig. 4.15. Encapsulation efficiency of curcumin in PLGA nanoparticles using different stabilizers. The stabilizer concentration in the aqueous phase was set to 5 mg mL^{-1} for all samples.

Focusing on poloxamer 407 as the most effective stabilizer regarding encapsulation the belonging mass concentration was recalculated to a molar concentration. As the number of stabilizer molecules is of utmost importance for stabilization this approach was taken. The resulting molar concentration of poloxamer 407 used in Fig. 4.15 was $3.97 \cdot 10^{-4} \text{ mol L}^{-1}$. All remaining stabilizers were adapted to this molar concentration and encapsulation efficiency was analyzed again for readjusted stabilizer concentrations. Compared to Fig. 4.15 the results were changing drastically (see Fig. 4.16). Tween 80 and Brij 98 are increasing in efficiency whereas PVA is dropping clearly. All considered stabilizers belonging to the poloxamer type were equalizing in encapsulation efficiency and aligning with poloxamer 407. Poloxamer 407 confirms the value from Fig. 4.15 as expected comparing both figures. Concluding from this it was assumed that the utilized stabilizer mass is not the key factor whereas the available number of stabilizer molecules highly influences the encapsulation of drug molecules into the produced particles.

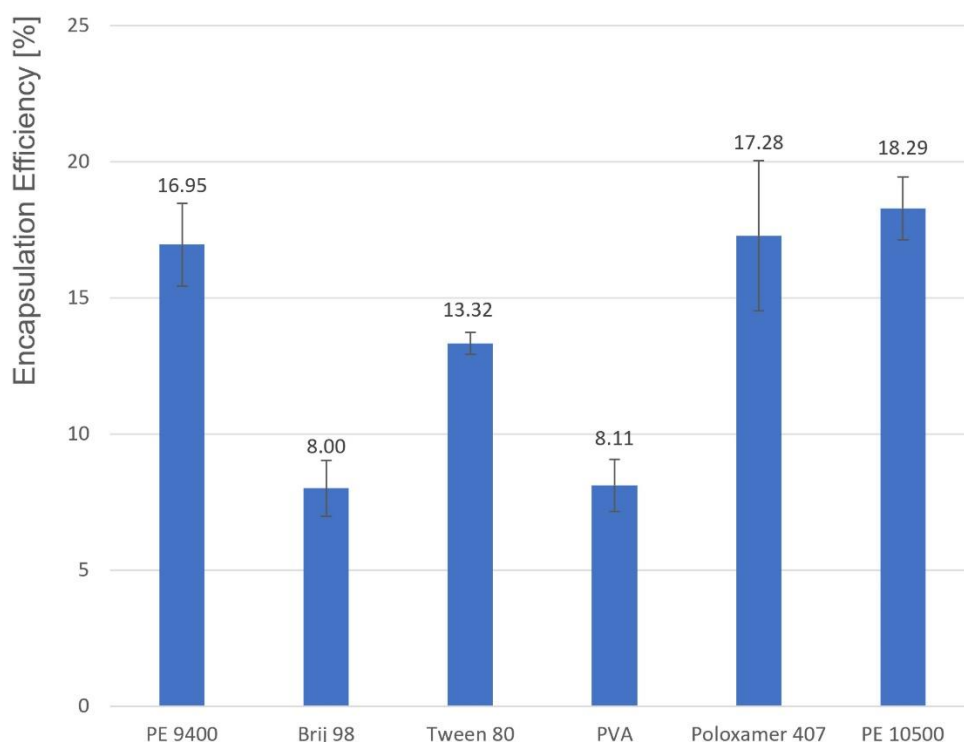


Fig. 4.16. Encapsulation efficiency of curcumin in PLGA nanoparticles using different stabilizers. The stabilizer concentration in the aqueous phase was set to $3.97 \cdot 10^{-4} \text{ mol L}^{-1}$ for all samples.

For more detailed information, concentration ranges around the already investigated $3.97 \cdot 10^{-4} \text{ mol L}^{-1}$ were analyzed. Adjacent molar concentrations $2 \cdot 10^{-4} \text{ mol L}^{-1}$ and $6 \cdot 10^{-4} \text{ mol L}^{-1}$ were included in the investigation with reference to an increase or decrease of encapsulation efficiency. Additionally, Tween 85 (HLB = 11 [23]) and poloxamer 188 (HLB = 29 [26]) were included in the following series of manufactured PLGA nanoparticles for a larger variety of stabilizers. Especially, Tween 85 was added due to its low HLB value to extend the HLB range to even lower values with the intention to avoid misassumptions regarding no influence of the HLB on encapsulation.

As displayed by Fig. 4.17 just Brij 98, Tween 80, and PE 10500 show a clear trend of an increasing encapsulation efficiency by reducing the stabilizer's molar concentration. Remaining stabilizers show no clear behavior regarding concentration effects. Nevertheless, from the three candidates a first assumption can be drawn that larger numbers of stabilizer in the surrounding medium can lead to lower drug encapsulation into the PLGA particles.

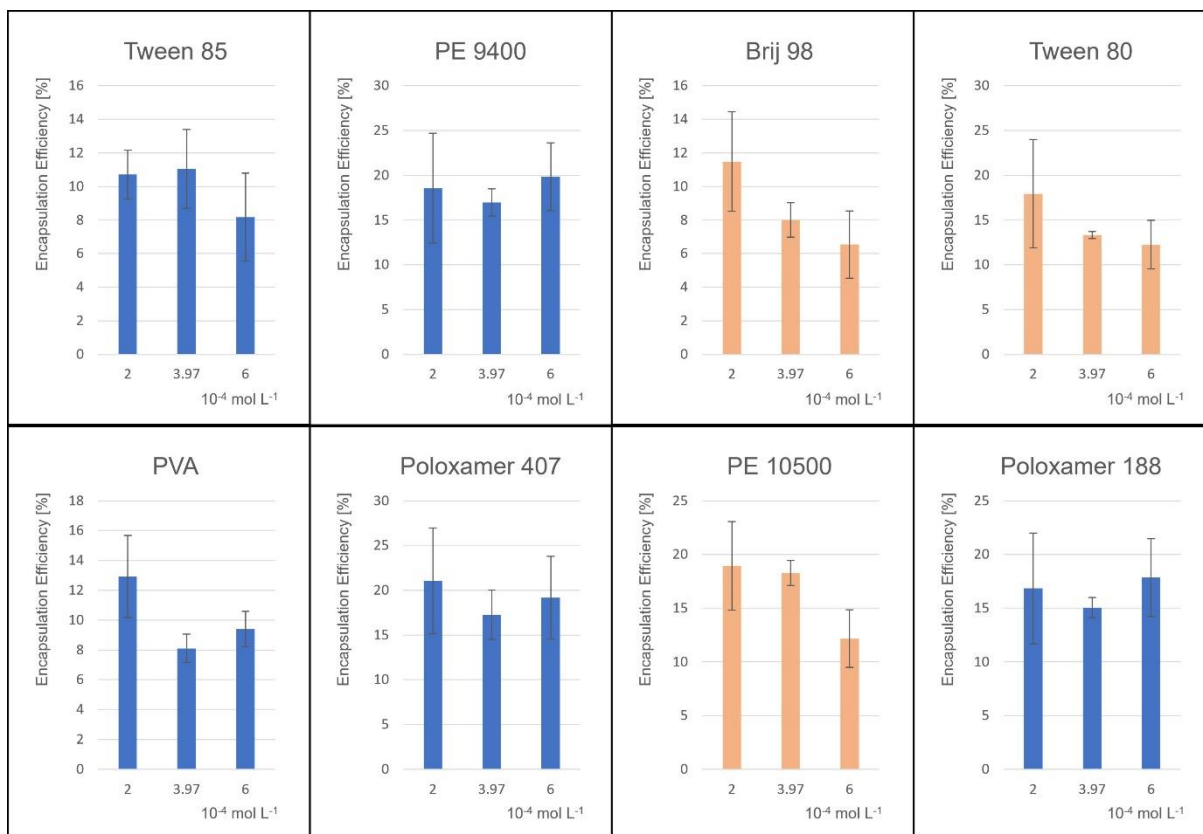


Fig. 4.17. Influence of three different PE molar stabilizer concentrations on the encapsulation efficiency (2×10^{-4} mol L⁻¹; 3.97×10^{-4} mol L⁻¹; 6×10^{-4} mol L⁻¹). One concentration above and below 3.97×10^{-4} mol L⁻¹ was chosen intentionally to highlight the behavior of the encapsulation efficiency related to the stabilizer concentration. A clear ascending encapsulation trend for a falling stabilizer concentration is just visible for Brij 98, Tween 80, and PE 10500 (highlighted in orange).

Due to no clear trend in influence of different molar concentrations on the encapsulation efficiency the same set of data was reanalyzed regarding drug loading. Since, encapsulation efficiency is influenced by the overall particle yield after particle preparation and purification, drug loading is not. The problem becomes clear by focusing on how encapsulation efficiency is calculated. Quantified mass of drug substance in the purified particle sample is divided by the utilized mass of drug substance in the experiment. In comparison to that drug loading results from the quantified mass of drug substance in the purified particle sample divided by the total yielded particle mass. Regarding this, a larger or smaller particle yield would influence the encapsulation efficiency significantly whereas the drug loading as a fixed ratio should not be influenced. However, in contrast to Fig. 4.17, Fig. 4.18 shows a clear trend for all included stabilizers. Drug loading increases by reducing the molar stabilizer concentration. Clearly, for all eight formulations tested 2×10^{-4} mol L⁻¹ delivers the highest loading. It is worth investigating how far this trend can be exploited for an optimal formulation.

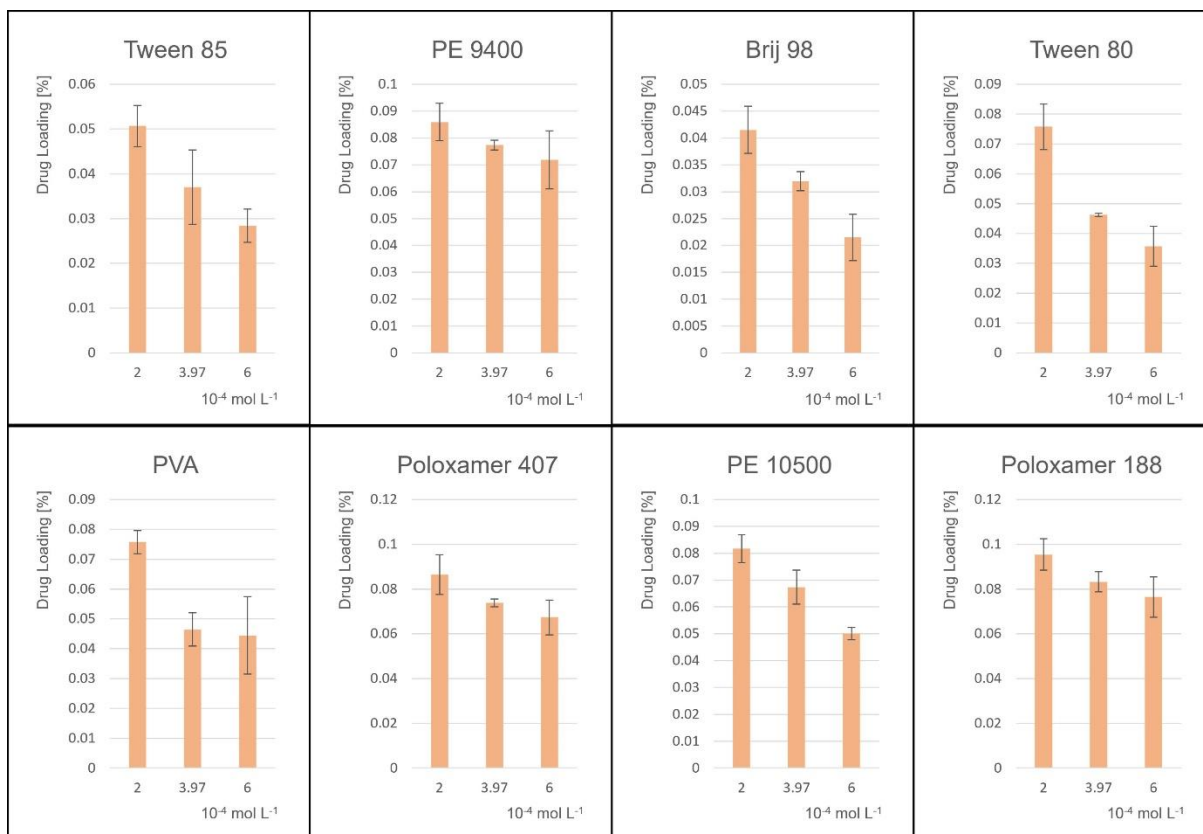


Fig. 4.18. Influence of three different molar stabilizer concentrations on the drug loading (2×10^{-4} mol L⁻¹; 3.97×10^{-4} mol L⁻¹; 6×10^{-4} mol L⁻¹). Shown diagrams are based on the same data as used for Fig. 4.17. Instead of encapsulation efficiency the drug loading of the PLGA particles is shown. Now an ascending trend in drug loading for a decreasing stabilizer concentration is visible for all investigated stabilizers.

To find a molar concentration for a maximized drug loading the previously observed trend was followed. Molar stabilizer concentrations were further reduced by including 1×10^{-4} mol L⁻¹, 0.75×10^{-4} mol L⁻¹, 0.5×10^{-4} mol L⁻¹ and 0.25×10^{-4} mol L⁻¹ into the series. Fig. 4.19 displays the results in drug loading for this extended range of molar stabilizer concentrations including previous data from Fig. 4.18 in orange and adding new data in green or blue. As shown in green PE 9400, PVA, poloxamer 407, and PE 10500 do not show further increase of drug loading by lowering the molar stabilizer concentration. Instead, drug loading stays on a certain level. A smaller deviation is shown at 0.5×10^{-4} mol L⁻¹ for PVA which is assumed to be an inaccuracy in curcumin quantification. Concluding from these data, curcumin loading could not be further increased by reducing the concentrations of PE 9400, PVA, poloxamer 407, and PE 10500 below 2×10^{-4} mol L⁻¹.

Added measurements for Tween 85, Brij 98, Tween 80, and poloxamer 188 (displayed in blue) show no clear trend regarding increase or decrease in drug loading. Tween 85 and Brij 98 show an increase regarding drug loading in some concentrations. Nevertheless, this increase is not continuous and is characterized by fluctuations. Tween 80 and poloxamer 188 are even dropping in drug loading for stabilizer concentrations below 2×10^{-4} mol L⁻¹.

Summing up the obtained data, an increasing molar stabilizer concentration can reduce the drug loading significantly. Accordingly, the chosen concentration is crucial for an effective drug loading. For reaching a maximum in drug loading the stabilizer concentration must be kept below $2 \cdot 10^{-4} \text{ mol L}^{-1}$. Concentrations below this threshold do not appear to affect the curcumin loading significantly (see Fig. 4.19). Interestingly, the type of stabilizer and respective HLB value is of minor importance whereas all investigated stabilizers can reach a comparable drug loading of around 0.07% to 0.08% if the stabilizer concentration was kept at or below the threshold value.

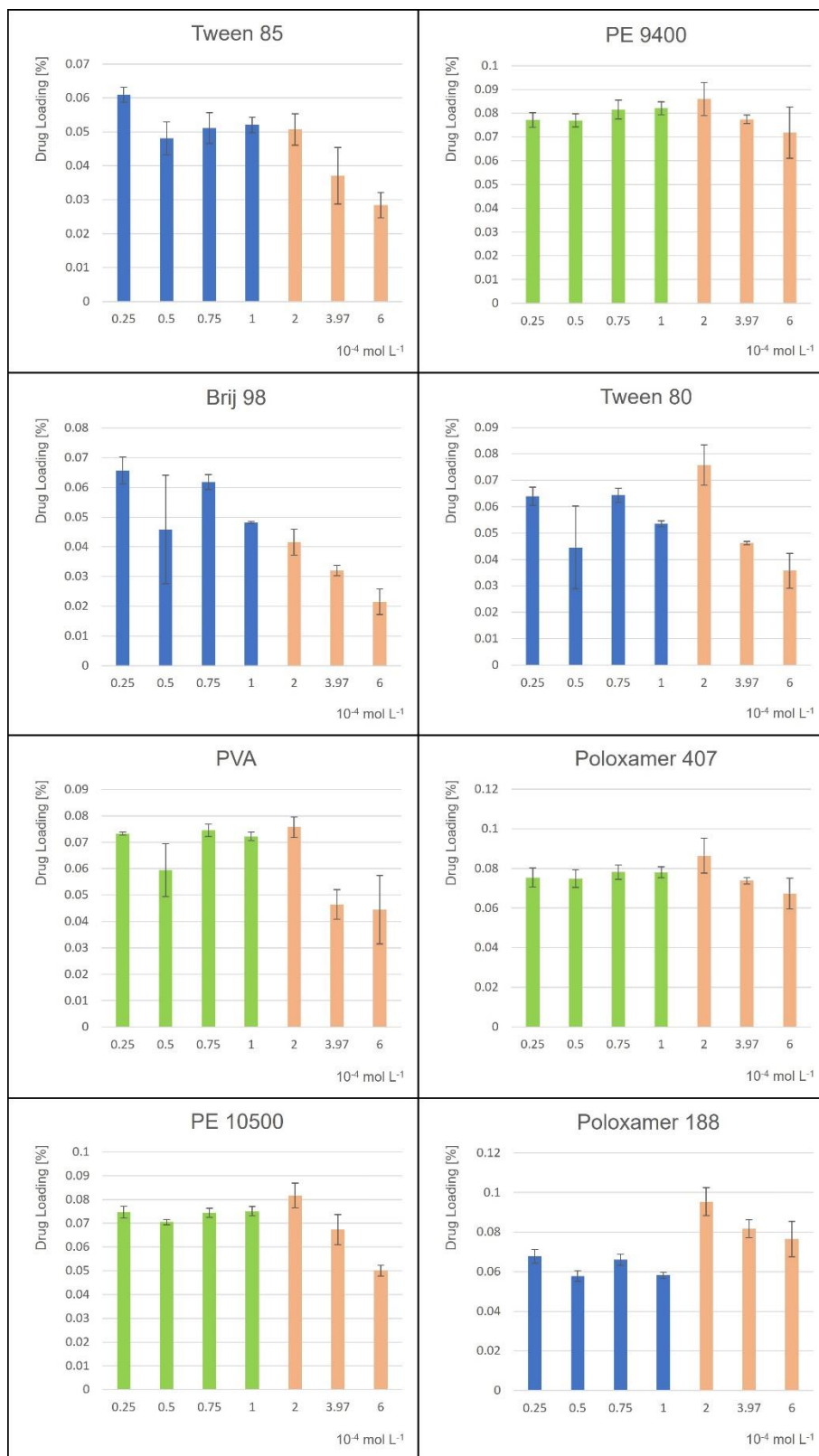


Fig. 4.19. Influence of further reduction of molar stabilizer concentration on drug loading. For all stabilizers concentrations of $1 \cdot 10^{-4} \text{ mol L}^{-1}$, $0.75 \cdot 10^{-4} \text{ mol L}^{-1}$, $0.5 \cdot 10^{-4} \text{ mol L}^{-1}$, and $0.25 \cdot 10^{-4} \text{ mol L}^{-1}$ augmented the data set. Data from Fig. 4.18 ($2 \cdot 10^{-4} \text{ mol L}^{-1}$, $3.97 \cdot 10^{-4} \text{ mol L}^{-1}$, $6 \cdot 10^{-4} \text{ mol L}^{-1}$) are included to the series in orange. For PE 10500, PVA, poloxamer 407, and PE 9400 new data are shown in green. Reducing molar concentrations below $2 \cdot 10^{-4} \text{ mol L}^{-1}$ did not result in an increase of drug loading. Instead, a plateau in drug loading was reached. Blue bars display unclear loading behaviors for remaining stabilizers while reducing molar concentrations.

Curcumin release from the particle system

Microfluidic particle manufacturing was carried out successfully as expected from performed microfluidic experiments in chapter three. After Centrisart purification the nanosuspension showed a curcumin concentration of $40.8 \mu\text{g mL}^{-1}$. From the curcumin quantification in supernatants and pellets of the respective samples the released curcumin content was calculated and displayed in Fig. 4.20. The average values affiliated to the time points are shown below:

0 h: **67.87%**, 1 h: **77.49%**, 6 h: **78.91%**, 24 h: **81.41%**

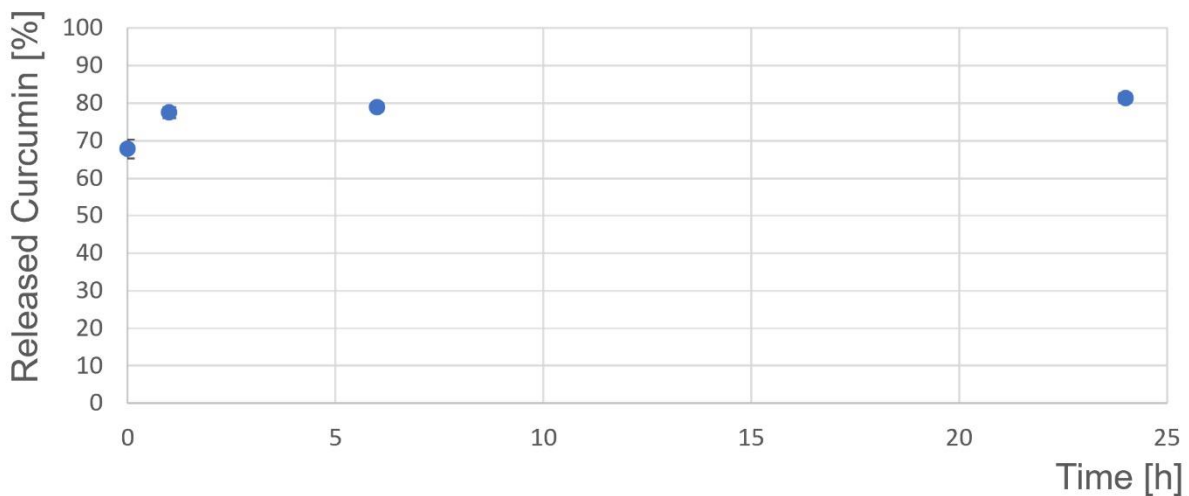


Fig. 4.20. Short time release study of curcumin over 24 hours. Right from the start a burst release is detectable showing an easy liberation of the drug into the surrounding medium (PBS containing Tween 80 (1 mg mL^{-1})).

Clearly, a burst release can be observed (Fig. 4.20). It highlights that no particle degradation is necessary for releasing larger amounts of the cargo. Curcumin incorporated inside of particles would have been released much slower during degradation of PLGA chains or diffusion driven over time. Obviously, this burst release profile could be influenced by enhancing the solubility of curcumin in water due to addition of Tween 80, but the overall trend would stay comparable. A faster release leads to the conclusion larger amounts of curcumin being located at the surface of particles which enables the drug substance to leave particles easily without being retained. Although, both substances show high lipophilicity a homogeneous distribution of curcumin in PLGA does not seem to occur. Nevertheless, accurate detection of the curcumin distribution inside of the particle is obviously difficult to carry out. Accordingly, more investigations must be done in this field.

Evaluation of the data

Results of previously mentioned encapsulation experiments including different stabilizer types and stabilizer concentrations conclude that the stabilizer's molar concentration is the most relevant and most important factor influencing the drug loading. In contrast to that, respective mass concentrations were not suitable for extracting a correlation in this direction. For the majority of stabilizers, a maximized drug loading results at or below a stabilizer concentration of $2 \cdot 10^{-4} \text{ mol L}^{-1}$ (exceptions: Tween 85 and Brij 98). Increasing this concentration led to a decrease in curcumin loading. It is comprehensible that an increase of stabilizer molecules in the system first leads to a full occupation of surfaces and subsequently to formation of micelles in the dispersant [14,27,28]. Micelles in the surrounding medium acting as a solubilizer [29] incorporate drug substance while dragging it away from the particle and lowering the overall particle drug loading (see Fig. 4.21).

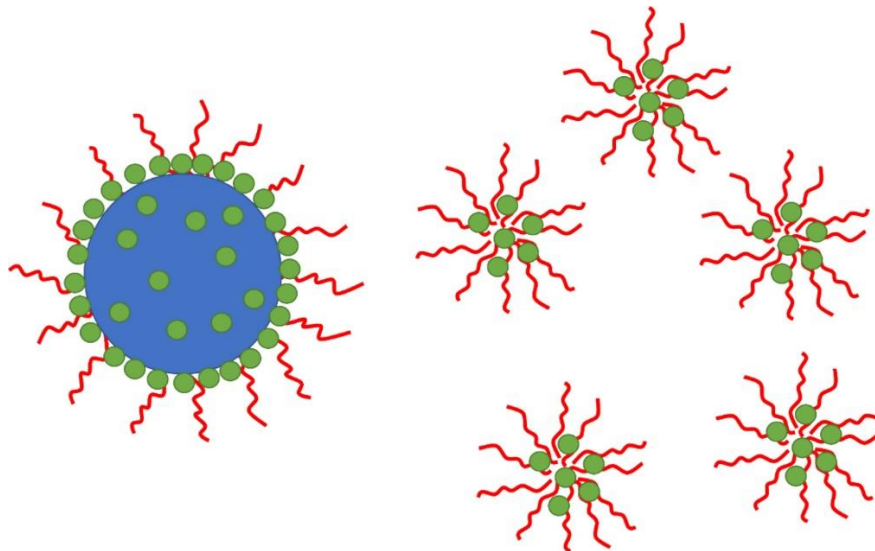


Fig. 4.21. Curcumin molecules (green dots) dispersed inside of a PLGA nanoparticle (blue) and in larger number attached to the particle surface. Curcumin loading on the particle is competing with drug incorporation in micelles formed by stabilizer molecules (red lines) in the surrounding dispersant. Here the stabilizer is simply acting as a solubilizer dragging drug substance away from the particle into the dispersant.

While yielding particles by centrifugation micelles remain in the supernatant leading to a lower drug mass in the harvested and separated pellet. This could be verified by centrifugation of pure stabilizer solutions. Three different stabilizer solutions (Tween 80, poloxamer 407, poloxamer 188, each 5 mg mL^{-1}) formed no visible or collectable pellet at the bottom of the used Falcon Tube and still showing the characteristic opalescence in the supernatant. Concluding from that, not a relevant number of micelles carrying drug substance can be included in a nanoparticle pellet to be harvested. Literature data proved that all three solutions ranged above the critical

micelle concentration confirming the general presence of micelles in the investigated solutions [30–35].

As previously shown in the release study curcumin shows a strong burst release from PLGA nanoparticles (Fig. 4.20) which can be explained by most of the drug being located on the particle surface (see Fig. 4.21). This indicates that curcumin does not dissolve in larger quantities in the polymer-based particle despite its high lipophilicity. The relatively low solubility of curcumin in PLGA additionally favors the drug encapsulation into micelles which are competing with the produced nanoparticles for internalizing curcumin molecules into their lipophilic core.

Nevertheless, below the molar concentration of $2 \cdot 10^{-4} \text{ mol L}^{-1}$, the different stabilizers show no significant effect on the curcumin loading. This can be concluded from the fact that by varying the stabilizer concentration below $2 \cdot 10^{-4} \text{ mol L}^{-1}$, the loading remains constant in most cases. Accordingly, the stabilizer molecules located on the particle surface do not affect the curcumin loading significantly and the decrease in drug loading above $2 \cdot 10^{-4} \text{ mol L}^{-1}$ can be attributed to the formation of micelles in the dispersant (and not to interaction between drug substance and stabilizer on the particle surface).

In general, it is questionable if this behavior is perfectly transferable to other particle systems. For the loading of curcumin in PLGA nanoparticles, previous investigations clearly showed that curcumin is not effectively encapsulated inside the nanoparticle core and, moreover, micelles (if present in the system) compete with the particles for drug loading. However, this does not necessarily have to be the case with alternative nanoparticle systems. The loading of other drug substances easier to incorporate into cores of respective nanoparticles may be less influenced by formed micelles in the dispersant. Further investigations on the influence of stabilizer micelles on drug loading focusing on alternative drug substances would be desirable. Accordingly, it always makes sense to screen for an influence of stabilizer concentration on drug loading for each individual system (drug substance, particle material, and stabilizer).

However, the key information to extract from this study is the following. If an influence of stabilizer concentration on drug loading can be detected, the type of stabilizer is of minor importance. In contrast to that, the number of stabilizer molecules in the entire system and a resulting micelle formation above a certain stabilizer concentration shows a much higher impact on the desired drug loading in general. If no micelles are introduced into the system by keeping stabilizer concentrations at a minimum the influence of the utilized stabilizers on drug loading is neglectable.

4.4 References

- [1] P.H.M. Hoet, I. Brüske-Hohlfeld, O. v. Salata, Nanoparticles – known and unknown health risks, *J Nanobiotechnology*. 2 (2004) 12. <https://doi.org/10.1186/1477-3155-2-12>.
- [2] J.G. Weers, D.P. Miller, Formulation Design of Dry Powders for Inhalation, *J Pharm Sci*. 104 (2015) 3259–3288. <https://doi.org/10.1002/JPS.24574>.
- [3] S.A. Yousef, Y.H. Mohammed, S. Namjoshi, J.E. Grice, H.A.E. Benson, W. Sakran, M.S. Roberts, Mechanistic Evaluation of Enhanced Curcumin Delivery through Human Skin In Vitro from Optimised Nanoemulsion Formulations Fabricated with Different Penetration Enhancers, *Pharmaceutics*. 11 (2019) 639. <https://doi.org/10.3390/PHARMACEUTICS11120639>.
- [4] R.R. Kotha, D.L. Luthria, Curcumin: Biological, Pharmaceutical, Nutraceutical, and Analytical Aspects, *Molecules*. 24 (2019) 2930. <https://doi.org/10.3390/MOLECULES24162930>.
- [5] C.F. Chignell, P. Bilskj, K.J. Reszka, A.G. Motten, R.H. Sik, T.A. Dahl, Spectral and Photochemical Properties of Curcumin, *Photochem Photobiol*. 59 (1994) 295–302. <https://doi.org/10.1111/J.1751-1097.1994.TB05037.X>.
- [6] H.K. Makadia, S.J. Siegel, Poly Lactic-co-Glycolic Acid (PLGA) as Biodegradable Controlled Drug Delivery Carrier, *Polymers (Basel)*. 3 (2011) 1377–1397. <https://doi.org/10.3390/POLYM3031377>.
- [7] N. Lababidi, V. Sigal, A. Koenneke, K. Schwarzkopf, A. Manz, M. Schneider, Microfluidics as tool to prepare size-tunable PLGA nanoparticles with high curcumin encapsulation for efficient mucus penetration, *Beilstein Journal of Nanotechnology*. 10 (2019) 2280–2293. <https://doi.org/10.3762/BJNANO.10.220>.
- [8] N. Lababidi, C.V. Montefusco-Pereira, C. de Souza Carvalho-Wodarz, C.M. Lehr, M. Schneider, Spray-dried multidrug particles for pulmonary co-delivery of antibiotics with N-acetylcysteine and curcumin-loaded PLGA-nanoparticles, *European Journal of Pharmaceutics and Biopharmaceutics*. 157 (2020) 200–210. <https://doi.org/10.1016/J.EJPB.2020.10.010>.
- [9] K.K. Chereddy, V.L. Payen, V. Pr at, PLGA: From a classic drug carrier to a novel therapeutic activity contributor, *Journal of Controlled Release*. 289 (2018) 10–13. <https://doi.org/10.1016/J.JCONREL.2018.09.017>.
- [10] J.A. Loureiro, M.C. Pereira, PLGA Based Drug Carrier and Pharmaceutical Applications: The Most Recent Advances, *Pharmaceutics*. 12 (2020) 903. <https://doi.org/10.3390/PHARMACEUTICS12090903>.
- [11] F. Danhier, E. Ansorena, J.M. Silva, R. Coco, A. le Breton, V. Pr at, PLGA-based nanoparticles: An overview of biomedical applications, *Journal of Controlled Release*. 161 (2012) 505–522. <https://doi.org/10.1016/J.JCONREL.2012.01.043>.
- [12] J.T. Davies, A quantitative kinetic theory of emulsion type. I. Physical chemistry of the emulsifying agent, *Proceedings of 2nd International Congress Surface Activity*. 1 (1957) 426.
- [13] R.C. Pasquali, M.P. Taurozzi, C. Bregni, Some considerations about the hydrophilic–lipophilic balance system, *Int J Pharm*. 356 (2008) 44–51. <https://doi.org/10.1016/J.IJPHARM.2007.12.034>.
- [14] A. Fahr, *Voigt Pharmazeutische Technologie*, Voigt Pharmazeutische Technologie. (2022). <https://doi.org/10.52777/9783769277487>.
- [15] C.J. Mart nez Rivas, M. Tarhini, W. Badri, K. Miladi, H. Greige-Gerges, Q.A. Nazari, S.A. Galindo Rodr guez, R. . Rom n, H. Fessi, A. Elaissari, Nanoprecipitation process: From encapsulation to drug delivery, *Int J Pharm*. 532 (2017) 66–81. <https://doi.org/10.1016/J.IJPHARM.2017.08.064>.

- [16] D. Primavessy, N. Günday Türeli, M. Schneider, Influence of different stabilizers on the encapsulation of desmopressin acetate into PLGA nanoparticles, *European Journal of Pharmaceutics and Biopharmaceutics*. 118 (2017) 48–55. <https://doi.org/10.1016/j.ejpb.2016.12.003>.
- [17] A. Dubes, H. Parrot-Lopez, W. Abdelwahed, G. Degobert, H. Fessi, P. Shahgaldian, A.W. Coleman, Scanning electron microscopy and atomic force microscopy imaging of solid lipid nanoparticles derived from amphiphilic cyclodextrins, *European Journal of Pharmaceutics and Biopharmaceutics*. 55 (2003) 279–282. [https://doi.org/10.1016/S0939-6411\(03\)00020-1](https://doi.org/10.1016/S0939-6411(03)00020-1).
- [18] S.L. Marusin, Sample preparation — the key to SEM studies of failed concrete, *Cem Concr Compos*. 17 (1995) 311–318. [https://doi.org/10.1016/0958-9465\(95\)00020-D](https://doi.org/10.1016/0958-9465(95)00020-D).
- [19] R.B. Miles, W.R. Lempert, J.N. Forkey, Laser Rayleigh scattering, *Meas Sci Technol*. 12 (2001) R33. <https://doi.org/10.1088/0957-0233/12/5/201>.
- [20] R. Barret, *Medicinal chemistry: Fundamentals*, Elsevier, 2018. <https://doi.org/10.1016/C2017-0-01426-X>.
- [21] O. Naksuriya, S. Okonogi, R.M. Schiffelers, W.E. Hennink, Curcumin nanoformulations: A review of pharmaceutical properties and preclinical studies and clinical data related to cancer treatment, *Biomaterials*. 35 (2014) 3365–3383. <https://doi.org/10.1016/J.BIOMATERIALS.2013.12.090>.
- [22] S. Mosallam, N.M. Sheta, A.H. Elshafeey, A.A. Abdelbary, Fabrication of Highly Deformable Bilosomes for Enhancing the Topical Delivery of Terconazole: In Vitro Characterization, Microbiological Evaluation, and In Vivo Skin Deposition Study, *AAPS PharmSciTech*. 22 (2021) 1–12. <https://doi.org/10.1208/S12249-021-01924-Z>.
- [23] H. Lian, Y. Peng, J. Shi, Q. Wang, Effect of emulsifier hydrophilic-lipophilic balance (HLB) on the release of thyme essential oil from chitosan films, *Food Hydrocoll*. 97 (2019) 105213. <https://doi.org/10.1016/J.FOODHYD.2019.105213>.
- [24] W.N. Omwoyo, P. Melariri, J.W. Gathirwa, F. Oloo, G.M. Mahanga, L. Kalombo, B. Ogutu, H. Swai, Development, characterization and antimalarial efficacy of dihydroartemisinin loaded solid lipid nanoparticles, *Nanomedicine*. 12 (2016) 801–809. <https://doi.org/10.1016/J.NANO.2015.11.017>.
- [25] T. Schmidts, D. Dobler, C. Nissing, F. Runkel, Influence of hydrophilic surfactants on the properties of multiple W/O/W emulsions, *J Colloid Interface Sci*. 338 (2009) 184–192. <https://doi.org/10.1016/J.JCIS.2009.06.033>.
- [26] A.C.S. Akkari, J.Z.B. Papini, G.K. Garcia, M.K.K.D. Franco, L.P. Cavalcanti, A. Gasperini, M.I. Alkschbirs, F. Yokaichyia, E. de Paula, G.R. Tófoli, D.R. de Araujo, Poloxamer 407/188 binary thermosensitive hydrogels as delivery systems for infiltrative local anesthesia: Physico-chemical characterization and pharmacological evaluation, *Materials Science and Engineering: C*. 68 (2016) 299–307. <https://doi.org/10.1016/J.MSEC.2016.05.088>.
- [27] A.R. Studart, E. Amstad, L.J. Gauckler, Colloidal stabilization of nanoparticles in concentrated suspensions, *Langmuir*. 23 (2007) 1081–1090. <https://doi.org/10.1021/LA062042S>.
- [28] A.D. Pomogailo, V.N. Kestelman, *Metallopolymer Nanocomposites*, Springer Berlin Heidelberg, 2005. <https://doi.org/10.1007/B137740>.
- [29] M.S. Haider, M.M. Lübtow, S. Endres, S. Forster, V.J. Flegler, B. Böttcher, V. Aseyev, A.C. Pöppler, R. Luxenhofer, Think beyond the Core: Impact of the Hydrophilic Corona on Drug Solubilization Using Polymer Micelles, *ACS Appl Mater Interfaces*. 12 (2020) 24531–24543. <https://doi.org/10.1021/ACSAMI.9B22495>.
- [30] L.S.C. Wan, P.F.S. Lee, CMC of polysorbates, *J Pharm Sci*. 63 (1974) 136–137. <https://doi.org/10.1002/jps.2600630136>.

- [31] B. Farhadieh, Determination of CMC and Partial Specific Volume of Polysorbates 20, 60, and 80 from Densities of Their Aqueous Solutions, *J Pharm Sci.* 62 (1973) 1685–1688. <https://doi.org/https://doi.org/10.1002/jps.2600621022>.
- [32] K. Bouchemal, F. Agnely, A. Koffi, G. Ponchel, A concise analysis of the effect of temperature and propanediol-1, 2 on Pluronic F127 micellization using isothermal titration microcalorimetry, *J Colloid Interface Sci.* 338 (2009) 169–176. <https://doi.org/10.1016/j.jcis.2009.05.075>.
- [33] M. Katakam, A.K. Banga, Use of poloxamer polymers to stabilize recombinant human growth hormone against various processing stresses, *Pharm Dev Technol.* 2 (1997) 143–149. <https://doi.org/10.3109/10837459709022619>.
- [34] V. Saxena, M. Delwar Hussain, Poloxamer 407/TPGS mixed micelles for delivery of gambogic acid to breast and multidrug-resistant cancer, *Int J Nanomedicine.* 7 (2012) 713–721. <https://doi.org/10.2147/IJN.S28745>.
- [35] A.M. Bodratti, P. Alexandridis, Formulation of poloxamers for drug delivery, *J Funct Biomater.* 9 (2018) 11. <https://doi.org/10.3390/jfb9010011>.

Chapter 5

Particle quantification

Contributions to the chapter:

Methodology, fabrication, sample preparation, investigation, data analysis, calculations, and result interpretation of all experimental data were done by the author of the thesis.

Single-particle tracking methodology and the MATLAB particle detection script was developed and written by Dr. Thomas John, Department of Experimental Physics, Saarland University, Saarbrücken, Germany.

Rhodamine B labeled PMMA nanoparticles were synthesized by Dr. Anna K. Boehm, Polymer Chemistry, Saarland University, Saarbrücken, Germany.

Analytical ultracentrifugation measurements were performed by Dr. Louis Weber, INM-Leibniz Institute for New Materials, Saarbrücken, Germany.

Gas pycnometry measurements were performed by Dominik Perius and Dominik Schmidt, INM-Leibniz Institute for New Materials, Saarbrücken, Germany.

Benchtop produced acetalated maltodextrin nanoparticles were provided by Salma M. Abdel-Hafez, Department of Pharmacy, Biopharmaceutics and Pharmaceutical Technology, Saarland University, Saarbrücken, Germany.

Parts of this chapter have already been published in the following research paper:

J. Buescher, T. John, A.K. Boehm, L. Weber, S.M. Abdel-Hafez, C. Wagner, T. Kraus, M. Gallei, M. Schneider, A precise nanoparticle quantification approach using microfluidics and single-particle tracking, *J Drug Deliv Sci Technol.* 75 (2022) 103579. <https://doi.org/10.1016/J.JDDST.2022.103579>.

5.1 Introduction: Particle quantification

For early formulation experiments very small batch sizes are desirable further reducing the formulation to the smallest possible amount. For nanocarriers as highly relevant formulations this holds also true [1–5]. In terms of solving solubility issues [6], protection of sensible drugs [7] and foster cellular uptake [8] they are often used. As already described in chapter three a suitable way of downscaling nanoparticle manufacturing can be the use of a microfluidic system [9,10]. Microfluidic systems allow to keep batch sizes as small as possible. Establishing quality control techniques is a key step for the investigation of these batches. Especially particle concentration in terms of real numbers is a major parameter of interest. For this type of analysis powerful tools are needed.

Measurements of nanoparticle sizes have been performed for a long time including light scattering techniques [11,12], scanning electron microscopy (SEM) [13], or atomic force microscopy (AFM) [14]. But only morphological and qualitative information about the respective particle collectives is provided by these methods. In contrast to this obtaining quantitative information on particle numbers is highly challenging.

However, nowadays some commercially available light scattering based techniques are available for determining particle numbers. Nanoparticle tracking analysis (NTA) [15,16], tunable resistive pulse sensing (TRPS) [17–19], or multi angle dynamic light scattering (MADLS) [11,12] are techniques to be mentioned here being currently on the market and providing nanoparticle concentration data. By counting the analyzed particles in the visualized volume NTA can determine a total particle concentration [20,21]. As a requirement for this quantification measurement the particle concentration must range between 10^7 – 10^9 particles per mL as the manufacturer suggests. The measurement itself is based on a diffusion measurement of particles in individually visualized areas of the total sample. From this, a number for the visible particles can be extracted [20,21]. TRPS is based on the coulter principle. It is capable of both sizing and counting particles [17]. Nevertheless, drawbacks of these systems are their high costs and the comparably high complexity in setting up a measurement. The Zetasizer Ultra already provides particle quantification by using MADLS as standard built-in function. Particle concentration measurements based on this approach are already reported in literature [22–24]. Yet, literature does not provide much information about concentration ranges which offer good data quality in terms of quantification precision.

This work establishes a quantification method for nanoparticles in highly diluted nanosuspensions. Mass concentrations of particles down to $0.8249 \mu\text{g mL}^{-1}$ could be quantified in number. Regarding the earlier mentioned standard techniques, the new approach was tested back-to-back. The main aim for the method was to improve quantification precision especially in low particle concentration ranges. Concentration ranges too small to be quantified by conventional gravimetric measurements [25,26] – including microbalances – considering a gravimetric approach as an absolute technique for determination of the total amount of particles. Furthermore, the intention

was to design a method which can quantify nanoparticles in an inexpensive, simple, and straightforward way and in addition to that can be applied to any fluorescent microscope with the functionality of detecting single particles.

The central idea regarding particle quantification is based on single-particle tracking [27–29]. Single-particle tracking was performed here in well-known volumes inside a microfluidic channel allowing to avoid just relying on the approximate volume covered by a laser beam, as it is the case with NTA, for example. The manufacturing of these channels is very reproducible and allows a precise measurements of channel depth, length, and width. Visualization of a certain area in the mentioned channel by using a microscope leads to a straightforward calculation of the visualized volume. A mean number of particles in the captured volume was determined by capturing an image sequence of the visualized channel section and using single-particle tracking to count the particles in it. The independence of the volume flow and the flow profiles in the channel is a great benefit of the developed approach. Only things to be ensured are a sufficient fluorescence for particle visualization and non-overlapping particles in the detection area. It does not play a major role how fast particles are traveling through the visualized channel section as long as they are moving with an appropriate speed according to the frame capturing rate. The total particle number of the analyzed sample can be calculated from the obtained particle count per volume. Rhodamine B labeled PMMA (poly(methyl methacrylate)) particles were used as a model nanosuspension due to their monodispersity. They were used as a reference particle collective for evaluating the determined particle counts. For realization and alternative investigation approach of the described number determination, a certain volume of the reference nanosuspension was freeze-dried [30]. Using a μ -balance the containing particle mass could be measured. The consequent mass of a single particle could be calculated using size information of the monodisperse particle sample (by using transmission electron microscopy [31,32]) as well as information about particle density (obtained by analytical ultracentrifugation [33–35], and gas pycnometry [36,37]). Bringing this information together, the PMMA particle concentration can be calculated as well using this gravimetric alternative. Using the two quantitative results both analytical approaches could be compared.

As additional characterization of PLGA nanoparticles manufactured in chapter four analytical ultracentrifugation was used to obtain density data for this kind of particle collective as well.

The next step was to compare the obtained single-particle tracking data to multi angle dynamic light scattering data focusing on the resulting PMMA particle concentrations and precision of the measurements. For the MADLS measurements the same PMMA particles were used as in single-particle tracking quantification. MADLS was chosen to highlight the single-particle tracking benefit regarding precision in very small particle concentrations and in general the extension in quantifiability to very low concentrations.

A realistic and non-idealized benchtop manufactured nanoparticle collective of coumarin 6 loaded acetalated maltodextrin particles [38] was quantified by the established single-particle tracking quantification method as a first trial for quantifying nanoparticles how it was intended for final drug products. In addition to that, acetalated coumarin 6 loaded maltodextrin particles were manufactured using the microfluidic approach (described in chapter three). Afterwards, this batch was quantified using single-particle tracking to show that the entire process of preparing nanoparticles in minimal batch sizes and the following nanoparticle quantification can also be carried out for realistic nanoparticle formulations.

To challenge the limits (especially in detection) of the single-particle tracking approach the fluorescence-based particle detection was switched to a dark-field based particle detection [39,40]. On purpose smaller but still highly fluorescent polystyrene particles were used to enable a visualization and particle quantification changing the detection method between fluorescence and dark-field very quickly. In addition, the smaller particle size challenged the dark-field detection as well, focusing on the comparably low scattering intensity compared to emitted light by fluorescence. Particles were tracked in the identical channel using dark-field and fluorescence detection alternating making a direct comparison between both detection methods possible.

5.2 Materials

Deuterium oxide (D₂O) and Kolliphor 188 (Poloxamer 188) were obtained from Merck, Darmstadt, Germany. Poloxamer 407 was purchased from Caesar & Loretz GmbH, Hilden, Germany. Polydimethylsiloxane (PDMS) (containing reagents RTV 615 A and B) was purchased from Momentive Performance Materials, Leverkusen Germany. The purification system Millipore, Milli-Q Synthesis, Merck, Darmstadt, Germany provided pure water. Ethylene diamine (99%), DCM (99.8% analytical reagent grade), and calcium hydride (93%) were obtained from Fisher Scientific GmbH, Schwerte, Germany. DCM was dried over calcium hydride before usage. Rhodamine B base (dye content 97%), sodium disulfide (for analysis), potassium hydroxide flakes (90% reagent grade), sodium dodecylsulfate (≥98.5%), and sodium persulfate (≥98%) were purchased from Sigma Aldrich, Taufkirchen, Germany. Methacryloyl chloride (97%) was obtained from ABCR, Karlsruhe, Germany. Triethylamine and acetonitrile were purchased from Th. Geyer GmbH Co. KG, Renningen, Germany. Ethanol (99% denatured with 1% MEK) was obtained from BCD Chemie GmbH, Hamburg, Germany. Allyl methacrylate (ALMA, >99%) and methyl methacrylate (MMA, 99%) were obtained from Sigma Aldrich, Taufkirchen, Germany. An alumina column (basic, 50-200 μm, Acros Organics, Schwerte, Germany) was used to remove the monomers' radical inhibitors for polymerization by passing the monomers through the column. Dowfax 2A1 was purchased from Dow Chemicals, Wiesbaden, Germany. For usage in emulsion polymerization, deionized water was degassed using a constant nitrogen flow for 30 minutes.

5.3 Particle quantification

5.3.1 Fluorescence microscopy

5.3.1.1 Methods

Synthesis of rhodamine B methacrylamide (RhBMA)

According to literature [41,42] RhBMA **3** (Fig. 5.1) was synthesized. Briefly, 9.6 g (20 mmol, 1 eq.) rhodamine B base **1** were dissolved in 120 ml ethanol and 9 g ethylene diamine (150 mmol, 7.5 eq.) were added to the solution dropwise. Whereby the color of the reaction mixture was changing from red to a darker shade it was heated to reflux for 15 hours. After cooling to room temperature, the solution was dried under reduced pressure. 40 mL of deionized water were added and extracted with DCM (two times, each 40 mL). The used DCM was combined, washed with water, and dried under reduced pressure. A dark, pink solid was obtained (yield: 79%). Rhodamine B amine **2** (the obtained product) was processed without any further purification to RhBMA **3**. To achieve this, under nitrogen atmosphere 8.3 g (17.2 mmol, 1 eq.) rhodamine B amine **2** was dissolved in 60 mL DCM. 5.8 mL (21.2 mmol, 2.4 eq.) triethylamine were added. Following, over 1 hour while keeping the reaction temperature at 0°C a solution of 3.4 mL (34.4 mmol, 4 eq.) methacryloyl chloride in 20 mL DCM was added dropwise. Afterwards, for 24 hours the reaction mixture was stirred at room temperature. For eight times the solution was washed using each 50 mL of deionized water, afterwards for three times washed using each 50 mL of a saturated Na₂CO₃ solution and finally at least once washed with 50 mL of a saturated NaCl solution. A pink solid was obtained after the purification and drying under reduced pressure (yield: 54%).

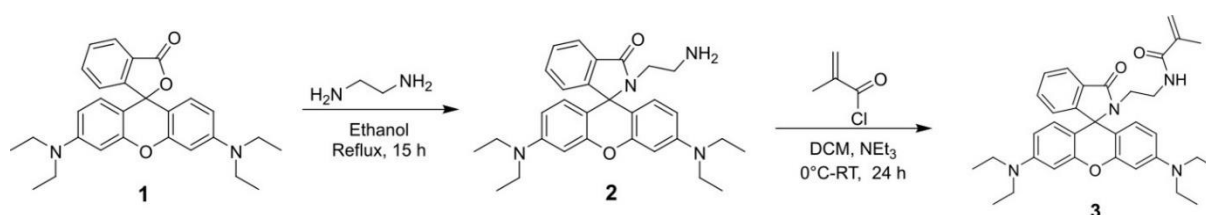


Fig. 5.1. Rhodamine B methacrylamide (RhBMA) synthesis scheme. Adopted with permission from [43]. ©2022, Elsevier

Synthesis of P(MMA-co-ALMA) seed particles

In a 1 L double-wall vessel equipped with nitrogen feeding, a reflux condenser and a stirrer the seed particles were synthesized at 85°C. A monomer emulsion consisting of

0.4 g ALMA, 3.6 g MMA, 0.05 g sodium dodecylsulfate (SDS) and 280 g deionized water was filled in the vessel and was stirred at 280 rpm. By adding 0.05 g sodium disulfite (NaDS), 0.3 g sodium persulfate (NaPS), and 0.05 g NaDS (all were dissolved in 5 mL deionized water) in this order the polymerization was initiated. After 15 minutes a monomer emulsion was added continuously with a feeding rate of 1.2 mL min⁻¹ containing 0.41 g KOH, 0.24 g SDS, 8 g ALMA, 72 g MMA, 0.23 g Dowfax 2A1, and 93 g deionized water. For feeding a rotary piston pump reglo-CPF digital, RH00 (Ismatec, Wertheim, Germany) was used. The final dispersion was stirred for 60 min before it was cooled to room temperature.

Synthesis of P(MMA-co-ALMA)@P(MMA-co-ALMA-co-RhBMA) core-shell particles

In a 250 mL double-wall vessel equipped with argon feeding, a reflux condenser and a stirrer core-shell particles were synthesized at 85°C. Inside the vessel 28.21 g deionized water and 27.39 g of the PMMA core particle dispersion were stirred at 280 rpm. By adding 0.006 g NaDS, 0.069 g NaPS, and 0.006 g NaDS (all were dissolved in 5 mL deionized water) in this order the polymerization was initiated. After 15 minutes a monomer emulsion was added continuously with a feeding rate of 0.2 mL min⁻¹ containing 0.007 g SDS, 0.068 g ALMA, 0.61 g MMA, 0.014 g Dowfax 2A1, and 3 g deionized water. For feeding the same rotary piston pump was used as described before. After another 15 minutes 0.011 g NaPS was added to reinitiate the polymerization. After 10 minutes a monomer emulsion was added continuously with a feeding rate of 0.2 mL min⁻¹ containing 0.08 g KOH, 0.059 g SDS, 1.5 g ALMA, 13.05 g MMA, 0.046 g Dowfax 2A1, 0.45 g RhBMA and 18.8 g deionized water. 60 minutes later the dispersion was cooled to room temperature after the polymerization of the core-shell particles was completed (Fig. 5.2).

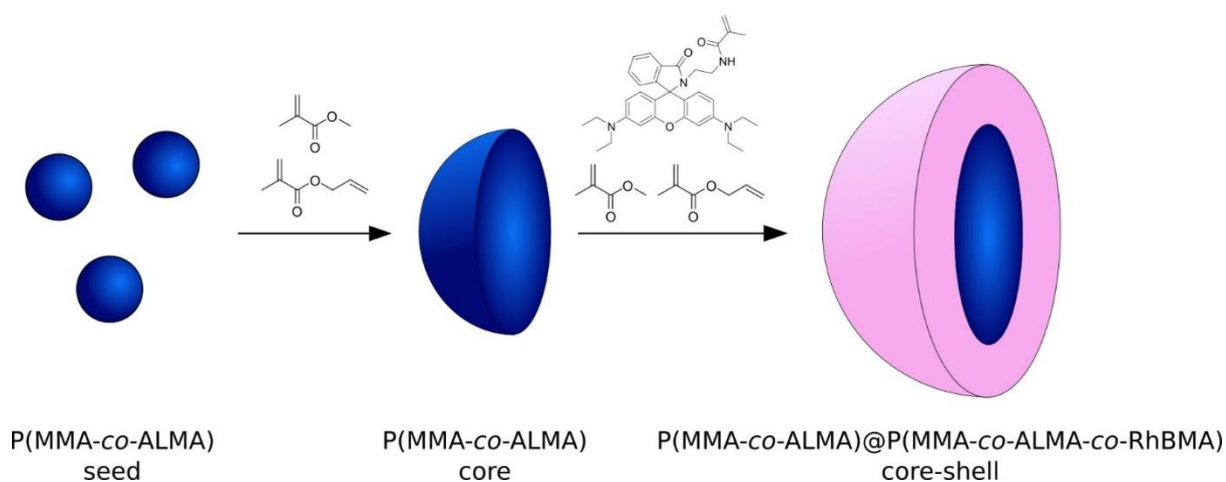


Fig. 5.2. P(MMA-co-ALMA)@P(MMA-co-ALMA-co-RhMBA) core-shell particles synthesis scheme. Adopted with permission from [43]. ©2022, Elsevier

Transmission electron microscopy (TEM) size measurements and volume calculation of PMMA particles

Carbon coated copper grids were used for sample preparation and polymer-based particles were diluted and drop-casted on the respective grids. Additional staining was not required for particle visualization. Using a JEOL JEM-2100 in bright field mode micrographs (Fig. 5.3) were recorded using a slow-scan charge-coupled device camera Gatan Orius SC1000. Operating voltage was set to 200 kV. For image analysis ImageJ (Open Source) was used. A mean volume for a single particle was calculated from the particle radius r extracted from TEM images (Fig. 5.3) assuming particles are spheres.

$$V_{particle} = \frac{4}{3}\pi r^3$$

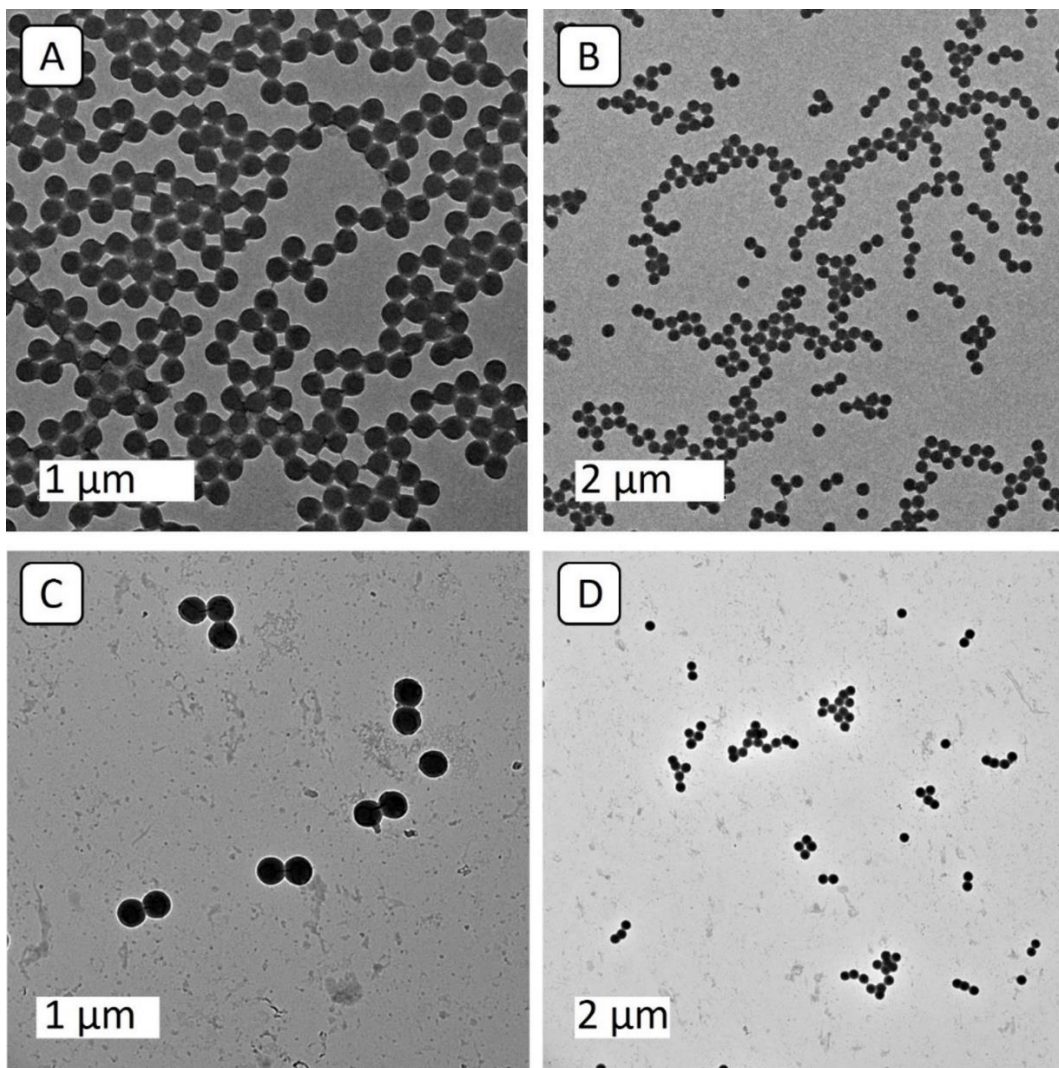


Fig. 5.3. Seed particles are represented by TEM photographs A and B. Final core-shell particles are shown by TEM photographs C and D. Images were used for particle size determination. Adopted with permission from [43]. ©2022, Elsevier

Sample preparation for single-particle tracking

From the stock dispersion five different particle concentrations were diluted and analyzed. An aqueous poloxamer 188 solution (1 mg mL^{-1}) was used for preparing the different dilutions. To lower the interfacial tension inside of the microfluidic channels and to increase the viscosity of the dispersion slightly poloxamer 188 was specifically chosen. To maintain a consistent small flow through the microfluidic channel these properties proved to be very helpful. Diluting from the originally synthesized suspension (82.49 mg mL^{-1}) the five different dilutions contained $0.8249 \text{ } \mu\text{g mL}^{-1}$, $0.618675 \text{ } \mu\text{g mL}^{-1}$, $0.41245 \text{ } \mu\text{g mL}^{-1}$, $0.206225 \text{ } \mu\text{g mL}^{-1}$, and $0.08249 \text{ } \mu\text{g mL}^{-1}$ regarding PMMA particles per volume. All the concentrations were analyzed as a triplicate.

Preparation of microfluidic chips for single-particle tracking

In epoxide master molds the microfluidic chips were prepared. By using soft lithography master molds were manufactured [44–46]. For manufacturing and especially predetermining a certain channel depth regarding the final chip these molds provide an exact negative image of the chip (see Fig. 5.4 C1). In a ratio of 10:1 reagents RTV 615 A and B were mixed (nine parts RTV 615 A and one part RTV 615 B) and filled in the mold. Crosslinking at 70°C results in PDMS [44] (Fig. 5.4 C2). The hardened PDMS can be detached from the mold after 24 hours of heating. For completing the measurement channels, they were sealed with a microscopic cover glass ($24 \text{ mm} \times 60 \text{ mm} \times 100 \text{ mm}$) from the bottom side. The bonding of the glass slide to the PDMS block was initiated by activating the surfaces with a plasma cleaner (Plasma Cleaner PDC-32G, Harrick Plasma, Ithaca, NY, USA) for 60 seconds. Following the activation both parts were stucked together and bonding was enforced by heating for 60 minutes at 70°C [44] (Fig. 5.4 C3). To make sure that nanosuspensions can be pumped into the measurement channels at the bottom side of the chip, the PDMS block was perforated with a hand punch from the top side towards the bottom side providing inlet channels for the suspension (Fig. 5.4 C4).

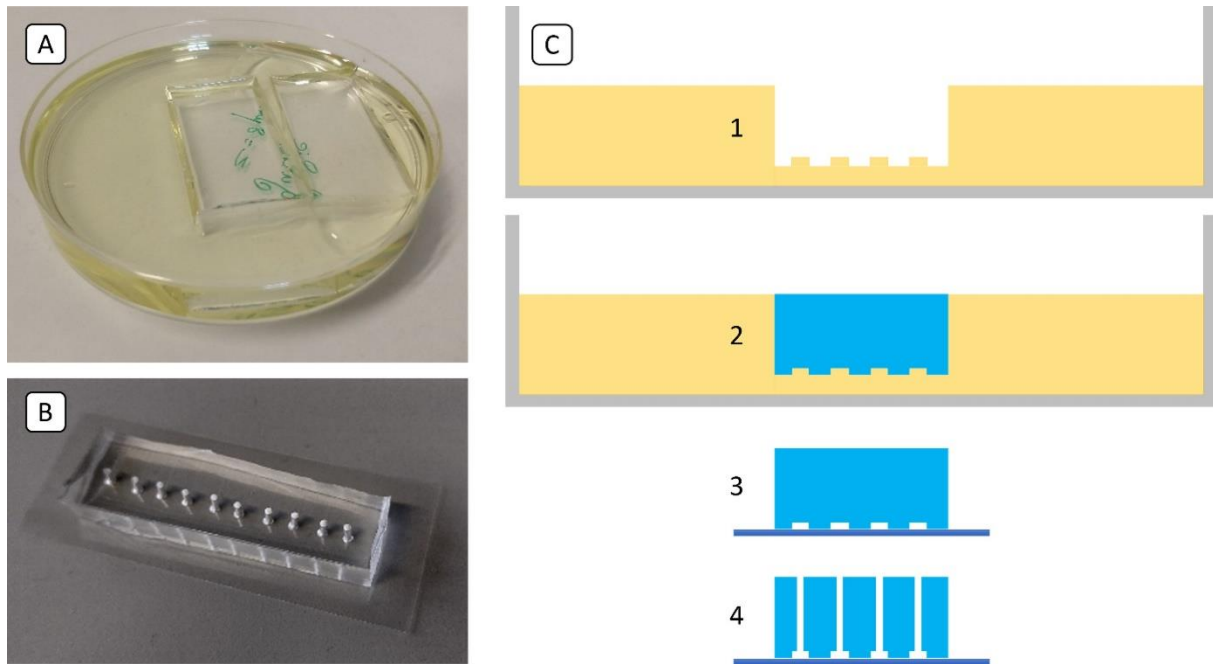


Fig. 5.4. A) PDMS part of the microfluidic counting device in the shape determining epoxide master mold. B) Finalized microfluidic counting device with inlet channels from the top and microfluidic channels at the bottom sealed with a glass slide. C) Process of device production: 1) Empty master mold. 2) PDMS filled master mold. 3) Crosslinked PDMS block with microfluidic channels on the bottom side sealed with a glass slide. 4) Finalized microfluidic counting device with added inlet channels for reaching the microfluidic channels.

Determination of the channel depth

To achieve cross-section cuts of the channels, a microfluidic chip was cut vertically with a scalpel. At ten different positions along the measurement channel these cross-section cuts were performed. This was carried out to check for differences in the channel depth distributed over the total channel length. For later particle concentration measurements, a mean channel depth was calculated from the measured values. By using Scanning Electron Microscopy (SEM) cross-section cuts were visualized. The device used for this visualization was an EVO HD15 (Zeiss, Jena, Germany). Earlier, the SEM samples were gold sputtered [47]. Using ImageJ, the depth could be extracted from the captured micrographs (Fig. 5.5).

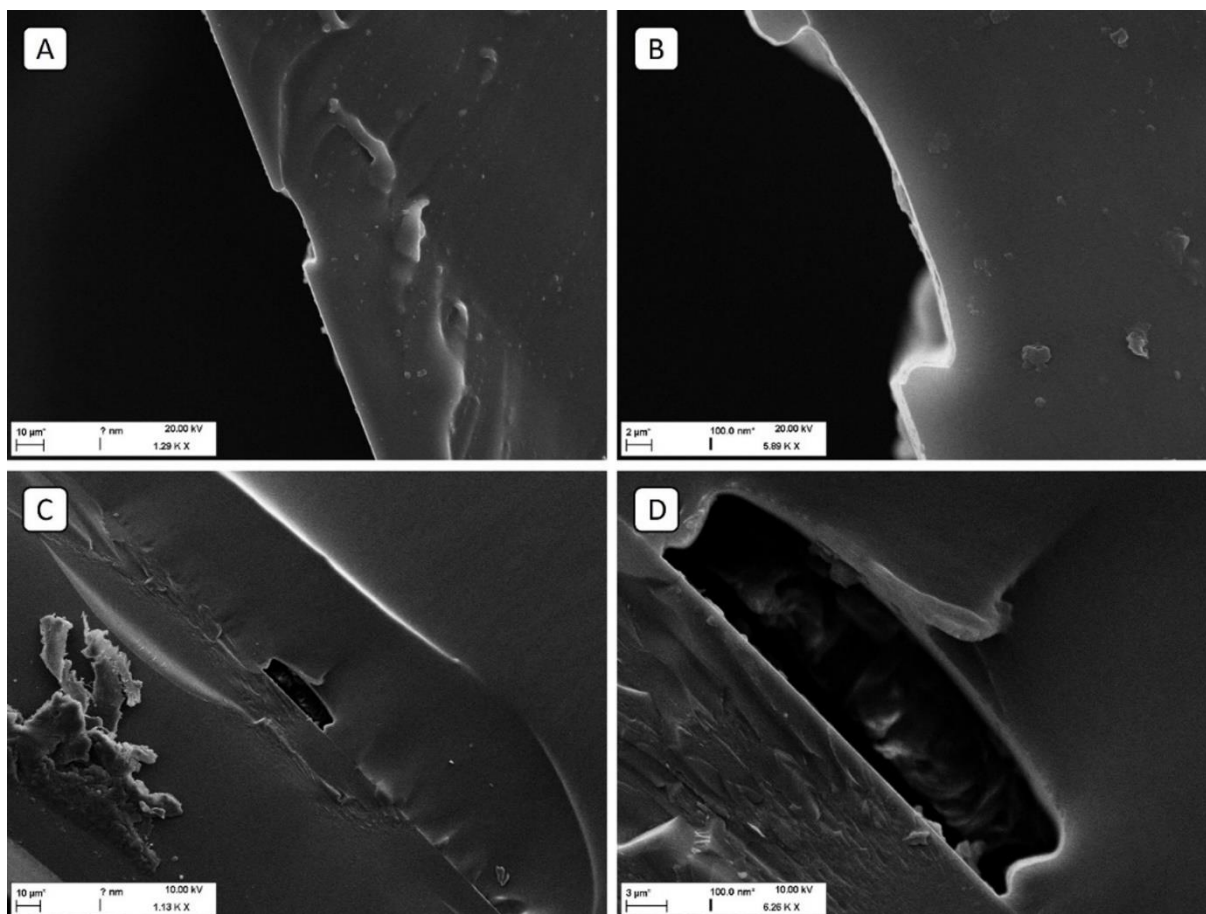


Fig. 5.5. SEM micrographs A and B are showing one non-finished channel in the PDMS block. It is not sealed from the bottom side. SEM micrographs C and D are showing a channel in the PDMS block ready for operation, which is sealed with a glass slide. Micrographs are used for determination of the channel depth. Adopted with permission from [43]. ©2022, Elsevier

Fluorescence microscopy

Concerning fluorescence excitation and visualization of rhodamine B labeled PMMA particles, an inverted fluorescence microscope (Eclipse Ti-S, Nikon Instruments Europe, Amsterdam, Netherlands) was used combined with a mercury lamp. It was equipped with an air-objective PLAN FL 20x with a numerical aperture (NA) of 0.70 (Nikon Instruments Europe, Amsterdam, Netherlands) in combination with a camera (Hamamatsu Photonics, C13440 Orca-Flash 4.0, Hamamatsu, Japan). The low NA and magnification allow to capture particles as sharp objects, even at different height positions over the channel depth provided by the depth of field of several μm . A depth of field, which is larger than the channel depth [48]. 10,000 images in sequence were captured by the mentioned setup. The frame rate resulted in 33.33 frames per second caused by an exposure time of 30 milliseconds.

In preliminary experiments using a plate reader (Infinite M200, Tecan Deutschland GmbH, Crailsheim, Germany) an excitation and emission spectrum were captured from the named particle collective (see Fig. 5.6).

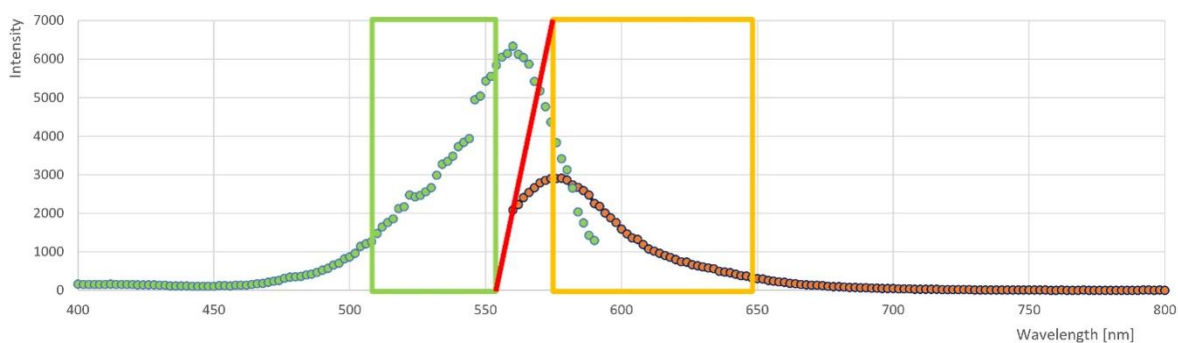


Fig. 5.6. Absorbance (green) and emission (orange) spectra of the rhodamine B labeled PMMA particles. The green rectangle symbolizes the bandwidth of the excitation filter, the orange one the bandwidth of the emission filter, and the red line the threshold value of the dichroic mirror in the filter cube. Absorbance values (green curve) are shown as intensity because for analysis a fixed emission wavelength of 620 nm was chosen, and respective values are the intensity values at 620 nm resulting from the corresponding wavelength given in the green curve.

Due to the special fluorescent requirements of rhodamine B a custom-made filter cube was compiled to isolate suitable wavelengths for imaging. Starting from the absorption and emission curves of rhodamine B labeled PMMA particles the single components were carefully selected to transmit as much excitation and emission light and to exclude as many unwanted wavelengths as possible. The selected wavelength windows are shown in Fig. 5.6. The fully assembled cube contained an excitation filter: 536/40 BrightLine HC, a dichroic mirror: 565 DCXR, and an emission filter: 610/75 ET Bandpass, all from AHF Germany (see Fig. 5.7 and 5.8). This specific dichroic mirror was selected to locate the cutoff (565 nm) perfectly between the peaks of the absorbance and emission curves. Accordingly, light of longer wavelengths could pass the mirror unhindered which was impossible for shorter wavelengths being reflected entirely. Excitation and emission filters were selected to fit as close as possible to the dichroic mirror allowing wavelengths closely below (excitation) and above (emission) the mirror cutoff to pass respective filters and to exclude undesired wavelengths from the detection.

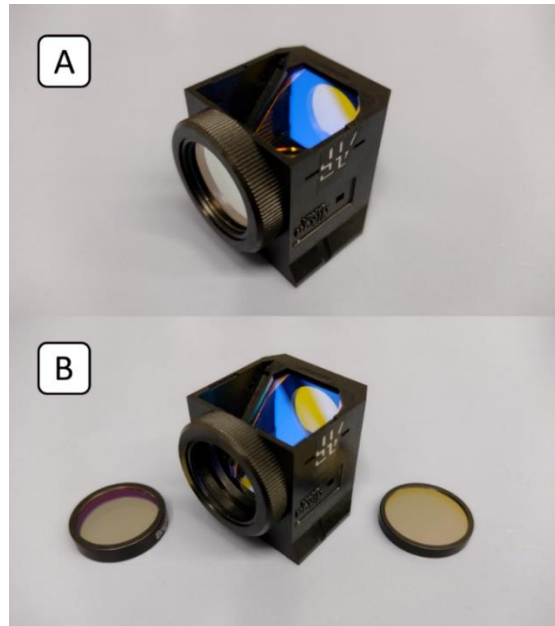


Fig. 5.7. A) Filter cube ready for operation. B) Filter Cube disassembled. Excitation and emission filters lying next to the cube which contains the dichroic mirror (observable due to the blue reflections inside of the cube).

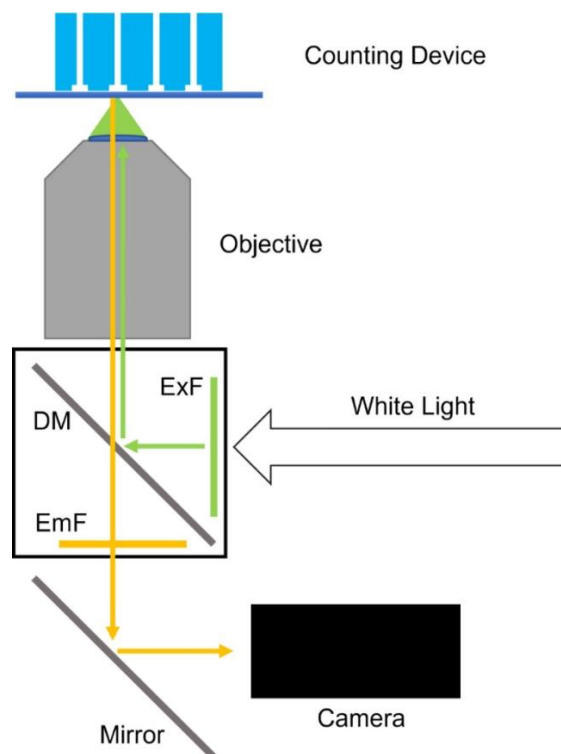


Fig. 5.8. Schematic overview of the used fluorescence microscope. White light (origin: mercury lamp) is filtered by an excitation filter (ExF) in the filter cube. Excitation light (here shown in green) is nearly totally reflected towards the sample by a dichroic mirror (DM) and is focused on a microfluidic channel. Emitted fluorescence light (origin: Rhodamine B labeled PMMA particles and shown in orange) passes the objective and the dichroic mirror. The emission filter (EmF) excludes all undesired wavelengths after the dichroic mirror and emitted fluorescence light is subsequently reflected into a camera for detection.

Performing single-particle tracking for particle quantification

To maintain a movement of particles through the PDMS chip a microfluidic flow controller was used (Microfluidic Flow Controller OB1 MK3+ from Elveflow, Paris, France). With an accuracy of 0.001 mbar per step the mentioned controller is applying air pressure to the sample in the applicable pressure range of 0.0 to 2.0 bar. For addressing a particle speed in the channel, which allows quantification, the flow rate was tuned manually. This includes preventing particles from moving too fast and being not detectable any more for the camera due to motion blur but still moving as fast as possible. Particles moving too fast appear as a fading streak instead of the desired dot-like structure. Chosen pumping pressures ranked between 5.0 mbar and 15.0 mbar depending on channel width and corresponding fluidic resistance conserving the best shape for detection. For proper particle speed and therefore proper particle visibility these pressures were specifically adjusted for every measurement. However, while the image sequence is recorded a certain number of particles should pass the channel. The result will be more accurate the larger the analyzed sample is chosen.

In a randomly selected section of the channel the image sequence is captured (Fig. 5.9). Channel depth was obtained using SEM, as previously described, width and length of the section were measured immediately in the image. By combining this information, the volume of the visualized area was calculated. For clarification, channel depth (obtained from SEM images) and channel length (captured in microscope image) remaining constant from sequence to sequence. While channel width, which the master mold predetermines, is differing from channel to channel.

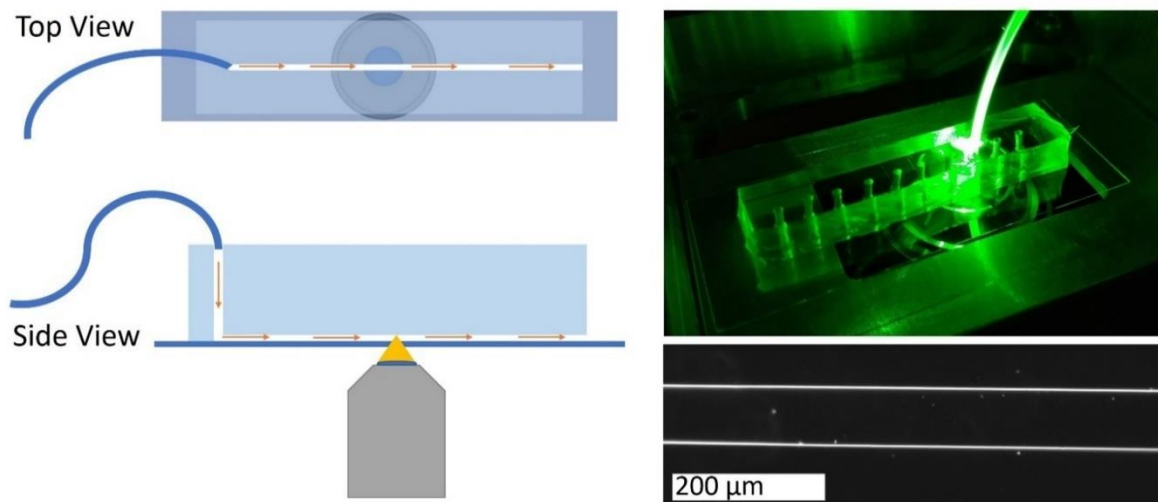


Fig. 5.9. Left: One channel in the microfluidic quantification device with a schematic top and side view. A PDMS block providing the preformed channel geometry sealed with a glass slide from below. The microscope's objective is displayed beneath. Right: Fluorescence microscope with the microfluidic quantification device during operation. Beneath this image a single microfluidic channel of the device is shown. The displayed area represents the selected volume used for the concentration measurement. Channel boundaries in this image are made visible as white lines using dark field microscopy [39]. For clarification, these lines disappear after switching from dark field to fluorescence. Adopted with permission from [43]. ©2022, Elsevier

Particle number analysis using a single-particle tracking script

Using a custom written script for MATLAB (MathWorks, Natick, United States), which is designed for highlighting, detecting, and counting particles in single images (Fig. 5.10), the recorded image sequences were analyzed. The differentiation of particles from the common background is essential in the region of interest. To realize this and to isolate all particles in the respective image, the script is analyzing the first 100 images and calculating the common background from these. Regions in the images, which are not changing in the sequence are detected and defined as a common background. From every single image this background is subtracted. Furthermore, this allows to exclude particles from the overall quantification, which are non-moving and therefore undesired. Thus, it is feasible to detect nanoparticles as single fluorescent spots traveling through the measuring channel. Avoiding overlap of particle fluorescence signals is mandatory. Therefore, to maintain separation of particles in recorded images analyzed particle concentrations are intentionally kept very low. Background noise must be excluded in the detection of particles. This is implemented by programming the MATLAB script to set detection levels correctly and to adjust detection thresholds for every recorded sequence automatically. This threshold is set between image background noise and particle signals. While detecting particles with MATLAB every captured sequence can be checked in parallel with ImageJ. This allows by randomized manual checking to control if the detection script is performing properly. Finally, the particles in every image are counted by the script. All particle counts are added up to a total count. This particle count is divided by the total number of captured images in the sequence leading to a mean particle count per image. To be precise, this leads additionally to a mean particle count per visualized volume. Note that, the mean number of particles in the observed volume is determining the particle concentration. This allows that same particles appear in consecutive images. The particle concentration of the non-diluted sample can be calculated easily from the obtained particle concentration.

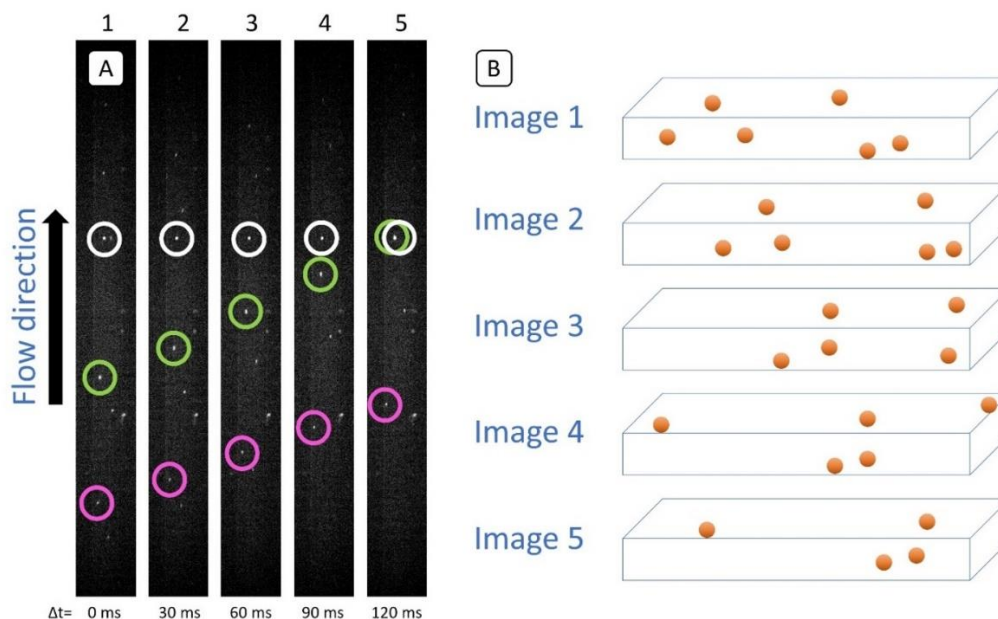


Fig. 5.10. A) Visualized channel with fluorescent core-shell particles inside. All five frames are chronological chosen and show different particles with different speeds – for example green and purple circle – moving through the visualized volume. For quantification 10,000 frames were captured. Non-moving and immobilized particles could be identified clearly as static objects. One example is the white circle.

B) The quantification process in schematic overview. SEM images in Fig. 5.5. and the lateral channel dimensions of the affiliated image sequence provide the visualized volume for quantification. Particles in every image can be counted precisely in the respective volume. The used microscope's objective was intentionally chosen to be able to visualize the channel depth in total. Adopted with permission from [43]. ©2022, Elsevier

Gravimetric measurement of the particle content in the original PMMA suspension

Into a pre-tared Eppendorf reaction tube one milliliter of the non-diluted PMMA nanoparticle suspension was transferred. After freezing the suspension at -80°C it was freeze-dried using an Alpha 4-3 LCS Basic (Christ, Osterode, Germany). Freeze-drying parameters were 0.200 mbar at room temperature (“main drying”) for four days and one additional day at 0.080 mbar at room temperature (“final drying”). Afterwards the Eppendorf reaction tube with dried nanoparticles inside was weighed again leading to the exact weight of the particle collective. A μ -balance (MC5, Sartorius, Göttingen, Germany) was used for this weight determination. The average particle mass per volume was calculated after repeating this weight determination six times.

Particle density measurements using analytical ultracentrifugation (AUC) and gas pycnometry

Density determination of PMMA particles was performed using a modified Optima XL-80K from Beckman Coulter [49]. An overview of the device is given in Fig. 5.11.

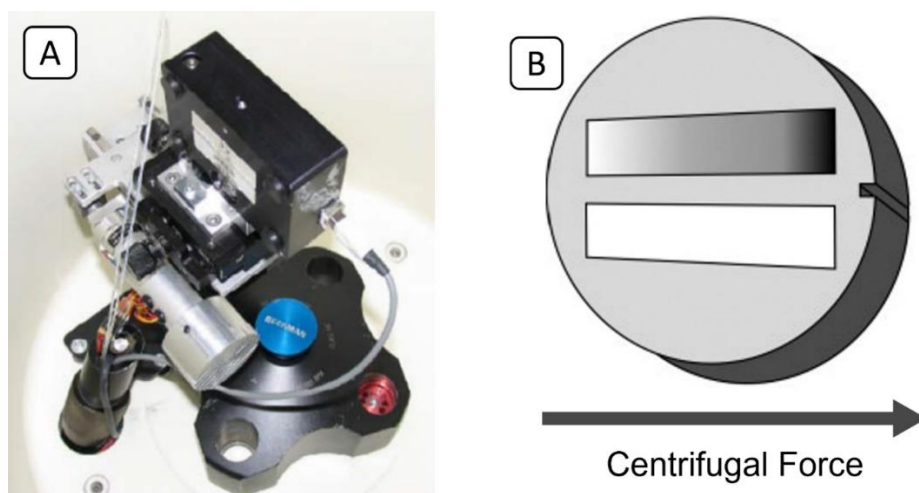


Fig. 5.11. A) Rotor and measuring device inside of an analytical ultracentrifuge. B) Schematic drawing of an analytical ultracentrifugation measurement cuvette with a sample cell (fading dark) and a reference cell (bright). Adopted with permission from [49,50]. ©2007, Elsevier and ©2009, Springer.

Following literature protocols [51–53] measurements were carried out diluting particles in pure H₂O and a 1:1 mixture of D₂O and H₂O. The idea was to calculate particle density directly from sedimentation coefficients relying on known viscosities and densities of the dispersants. For sample preparation 0.2% of the original suspension was utilized. To avoid too high or too low absorbance levels inside the cuvette during the experiment this concentration was selected. Every suspension was measured against its pure dispersant in the reference cell (either pure H₂O or 1:1 mixture of D₂O and H₂O) as it is shown in Fig. 5.11 B. Holding a constant rotor speed of 2000 rpm at 20°C both measurements were performed at an absorbance wavelength of 530 nm. Inside of the cuvette the named rotor speed resulted in a g-gradient from min. 271.9 g to max. 319.0 g. For both samples sedimentation coefficients [s_1 (H₂O) and s_2 (D₂O/H₂O)] were obtained from the AUC experiments. Respective sedimentation coefficients were extracted using a gaussian fit over the obtained peaks (see Fig. 5.12) and taking the average value of this fit. A gaussian fit was necessary as the obtained peaks were not well defined. The observable second peak in each graph was assumed to consist of agglomerates built of two or more particles in contrast to the first peak which clearly represents single particles sediment on their own. Even using ultrasonication could not disassemble particle agglomerates which additionally can be formed at any time. Fading out from the second peak to higher values leads to the conclusion that different orientations towards the direction of sedimentation or different shapes of agglomerates resulting in slower or faster particle velocity while centrifugation.

However, each visually comparable point on both graphs resulting in nearly identical calculated density values, which makes sense keeping in mind that material density stays the same for all particles in the suspension, but agglomerate size is changing.

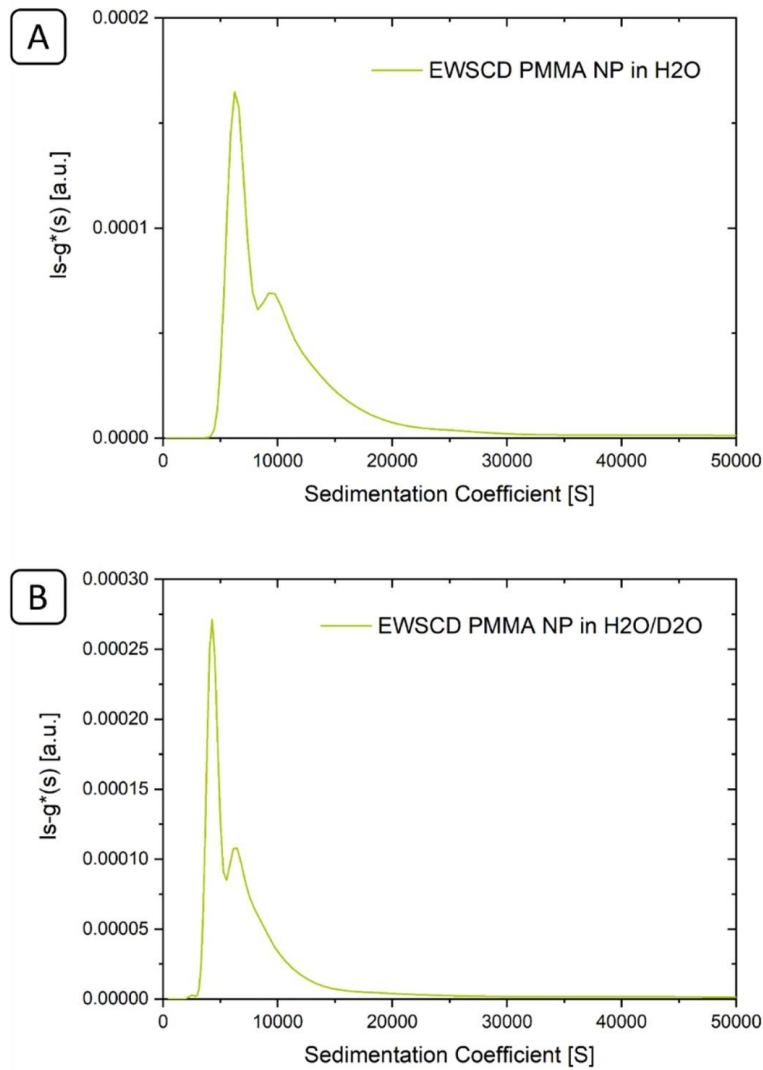


Fig. 5.12. Sedimentation coefficient distributions. Analyzed particles are core shell PMMA nanoparticles. A) Dispersant consisting of H₂O. B) Dispersant consisting of a 1:1 mixture of H₂O and D₂O. Adopted with permission from [43]. ©2022, Elsevier

Using the following equation and including the sedimentation coefficients obtained by the gaussian fit, the density of the PMMA particles could be calculated [51,52]:

$$\rho_{Particles} = \frac{s_2 \eta_2 \rho_1 - s_1 \eta_1 \rho_2}{s_2 \eta_2 - s_1 \eta_1}$$

Regarding H₂O and the 1:1 mixture of D₂O and H₂O, values for density (ρ) and dynamic viscosity (η) at 20°C were extracted from literature [52] and are displayed in table 5.1.

Table 5.1. Material parameters of H₂O and the 1:1 mixture of D₂O and H₂O at 20°C used for particle density calculation. Data is taken from Nontapot et al. [52]. Table adopted with permission from [43]. ©2022, Elsevier

η (H ₂ O)	1.0016 mPa s
η (D ₂ O/H ₂ O)	1.0629 mPa s
ρ (H ₂ O)	0.9982 g/cm ³
ρ (D ₂ O/H ₂ O)	1.0516 g/cm ³

As the chosen procedure offers also for particles with broader sized distribution the option to measure the density, the AUC density determination was carried out for “classical” benchtop produced PLGA nanoparticles manufactured in chapter four. In this case no drug substance was included in the particle production. Accordingly, the density of pure PLGA particles including poloxamer 188 as a stabilizer on particle surfaces was determined. The density measurement was carried out exactly as already performed for PMMA particle density determination. Resulting sedimentation distribution curves are displayed in Fig. 5.13. Obviously, due to a larger distribution in diameter the PLGA distribution curves of sedimentation coefficients are much broader compared to already mentioned PMMA nanoparticle data. Nevertheless, maximum values of the curves could be utilized for the density calculation. Independent of the distribution width associated values (maximum values, bending points, etc.) in both curves representing identical diameters in the distribution. As they correspond to each other they can always be used for the calculation. Since, they represent the same particles just in a different dispersant. Both additional peaks for smaller sedimentation coefficient values (small peak in the blue graph and small curvature in the green graph) were considered as artifacts appearing sometimes during these measurements.

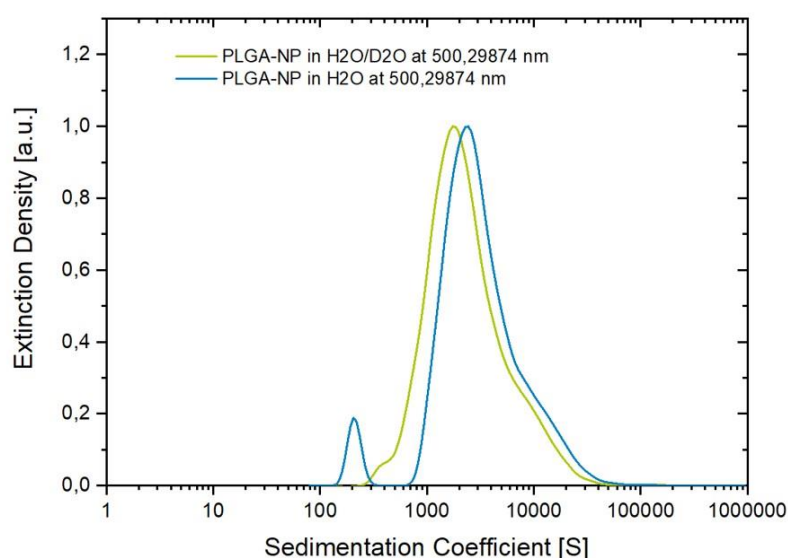


Fig. 5.13. Sedimentation coefficient distributions. Analyzed particles are PLGA nanoparticles stabilized with poloxamer 188. Blue curve: Dispersant consisting of H₂O. Green curve: Dispersant consisting of a 1:1 mixture of H₂O and D₂O.

In addition to this, the density of PMMA particles was also determined by gas pycnometry as an alternative method in a dry environment. This way, potential swelling effects can be excluded. An AccuPyc 1330 from Micromeritics, Norcross, Georgia, USA was used for these measurements. A bulk mass of about 250 mg freeze-dried particles was analyzed in each measurement using helium for density determination. A schematic overview of the measurement setup is given in Fig. 5.14.

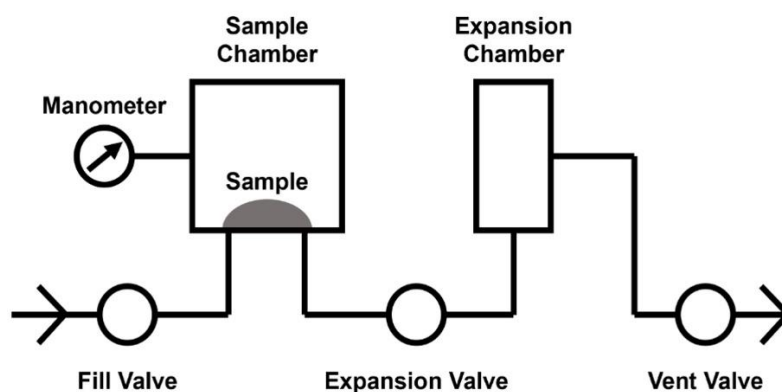


Fig. 5.14. Schematic overview of the used gas pycnometer. Image designed and modified with regard to the device manual.

Particle quantification using gravimetric data

The mass of a single particle could be calculated with information about volume and density of the analyzed particles using the following equation:

$$m = \rho * V$$

For obtaining the number of particles in 1 mL of original PMMA suspension the average mass of 1 mL dried particle suspension was divided by the calculated mass of one single particle (for this approach a monodisperse particle ensemble is necessary).

Multi angle dynamic light scattering (MADLS) for particle quantification

The Zetasizer Ultra was used for particle quantification based on MADLS. For facilitating particle quantification, 74.5 kcps was utilized as a background count rate. By analyzing the device response to pure Milli-Q water as dispersant for the diluted PMMA particle suspension this value was identified. Obviously, this measurement provided no usable size information, but provided the needed background count rate of the dispersant.

However, from the original stock dispersion (82.49 mg mL⁻¹) five different particle concentrations were diluted using Milli-Q water. Different concentrations contained

0.08249 mg mL⁻¹, 0.0618675 mg mL⁻¹, 0.041245 mg mL⁻¹, 0.0206225 mg mL⁻¹, and 0.008249 mg mL⁻¹ of particle material per volume. The Zetasizer is limited to a certain concentration range and the named particle concentrations cover this range. It was revealed by preliminary experiments that bad data quality was obtained if higher or lower concentrations were quantified not allowing for concentration determination. For balancing the high fluctuation in concentration measurements each concentration was quantified nine times.

Statistical analysis

By performing a one-way analysis of variance (ANOVA) to an alpha-value of 0.05 the obtained particle concentrations were compared and checked for significant differences. A significant difference was considered at p-values < 0.05.

Quantification of benchtop produced non-idealized nanoparticles based on acetalated maltodextrin

A nanoparticle system based on acetalated maltodextrin was chosen to test the single-particle tracking approach on a realistic particle collective. Particle production was carried out as already described in literature [38]. For fluorescent labeling coumarin 6 was loaded on the particles. The coumarin 6 content added to the particle material during the preparation of particles equals 2% of the polymer mass. Quantification of particles based on single-particle tracking was exactly performed as previously described. The analyzed sample contained 42.67 ng mL⁻¹ as particle mass concentration. For crosschecking the nanosuspension was also quantified using MADLS as an alternative method. The MADLS quantification also was exactly performed as previously shown. The analyzed MADLS sample contained 42.67*10³ ng mL⁻¹ as particle mass concentration.

Quantification of microfluidic produced non-idealized nanoparticles based on acetalated maltodextrin

For testing the single-particle tracking approach also on microfluidic manufactured particles acetalated maltodextrin particles were produced this way. The microfluidic production device was used as preciously described in chapter three. As the organic phase acetonitrile was used with dissolved acetalated maltodextrin resulting in a mass concentration of 5 mg mL⁻¹. In addition to that, coumarin 6 (2% of the acetalated maltodextrin content) was dissolved in this phase as well. The aqueous phase consisted of an alkaline poloxamer 407 solution (5 mg mL⁻¹) for particle stabilization. It was alkalinized by adding trimethylamine in a concentration of 40 mg mL⁻¹. In this type of manufacturing an alkaline dispersant is necessary to keep particles from degrading. For particle precipitation the flow rate ratio in the microfluidic chip was calculated and tuned to 1 part organic phase and 9 parts aqueous phase resulting in a final particle

mass concentration of 0.5 mg mL^{-1} . Particle size of the freshly prepared sample was measured using the Zetasizer.

After particle formation no further purification step was carried out. Instead, the number concentration regarding the particles was determined directly after manufacturing. The single-particle tracking based quantification was performed as described earlier using a dilution of the sample, which contained $0.25 \text{ } \mu\text{g mL}^{-1}$ as particle mass concentration. Analysis of the sample was carried out as a triplicate.

5.3.1.2 Results and discussion

Results from single-particle tracking

As a model particle system, different concentrations of dispersed PMMA particles containing a fluorescent rhodamine B functionalized shell were analyzed for demonstrating the usage of particle quantification based on single-particle tracking. Relying on TEM imaging the average size of the particle collective resulted in $267.03 \pm 9.79 \text{ nm}$. Measuring channel depth led to an average value of $6.57 \text{ } \mu\text{m}$. For all measured samples the visualized channel sections had the length of $390 \text{ } \mu\text{m}$. As mentioned before, channel width was differing in a range from $31 \text{ } \mu\text{m}$ to $55 \text{ } \mu\text{m}$ between the samples. Using these previously shown values, visualized volumes were calculated and ranged between $79,784 \text{ } \mu\text{m}^3$ and $139,622 \text{ } \mu\text{m}^3$. To ensure that all particles with sufficient fluorescence signal can be visualized inside this volume by the used objective the relatively low channel depth was chosen intentionally. Now that channel dimensions were well-known the exact volume containing counted particles was determinable.

The results of five different particle concentrations are shown in Fig. 5.15. All the analyzed concentrations were diluted from the stock suspension. Displaying the extended quantification range and precision in highly diluted samples particle concentrations were set as low as possible being still realistic regarding time consumption. Here the lowest quantified particle concentration contained $0.08249 \text{ } \mu\text{g mL}^{-1}$ of PMMA particles. If needed particle concentrations could be reduced further. Theoretically speaking, one single particle per sample would be enough for quantification, if the whole sample volume would be analyzed. In direct comparison to conventional gravimetric and other quantification approaches this points out the superiority of the developed single-particle tracking approach.

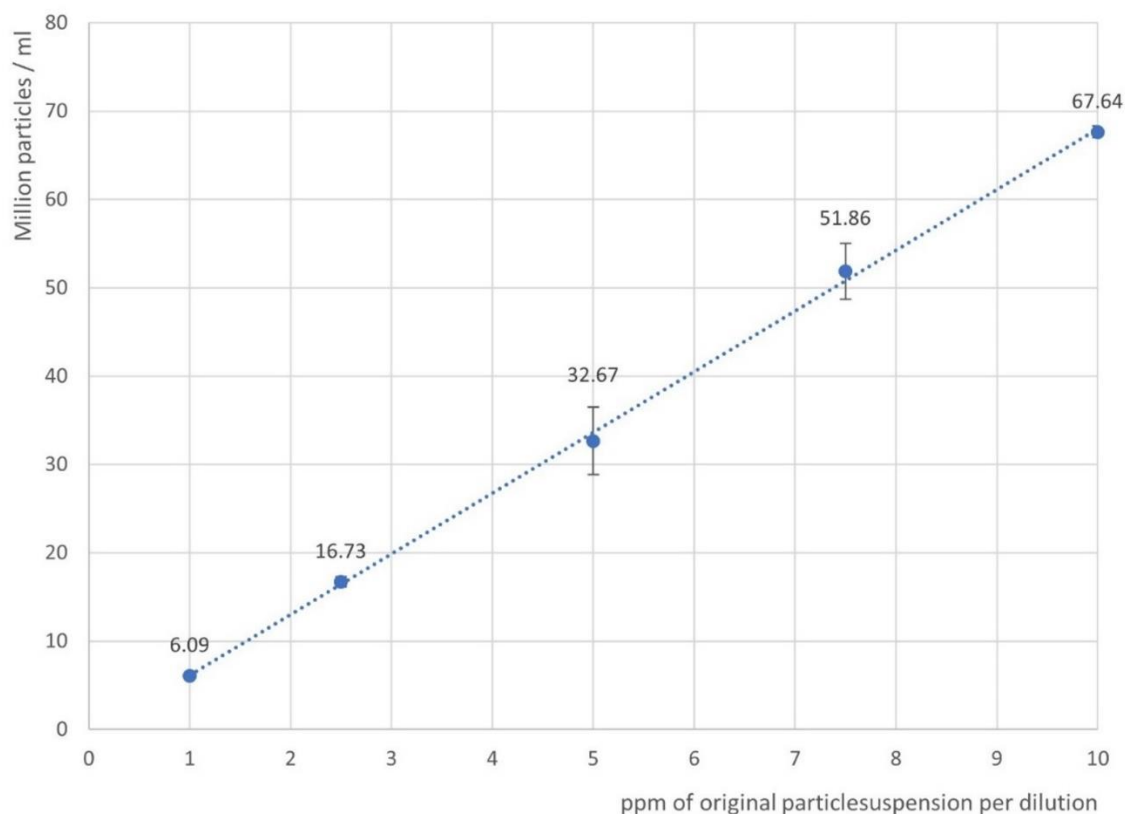


Fig. 5.15. Single-particle tracking results for concentration measurements of used PMMA particles. The different concentrations are diluted ($n = 3$) from a stock suspension (82.49 mg mL^{-1}) and resulting in $0.8249 \text{ } \mu\text{g mL}^{-1}$, $0.618675 \text{ } \mu\text{g mL}^{-1}$, $0.41245 \text{ } \mu\text{g mL}^{-1}$, $0.206225 \text{ } \mu\text{g mL}^{-1}$, and $0.08249 \text{ } \mu\text{g mL}^{-1}$. The graph clearly shows the conserved linearity in the measurements according to the dilution steps. $R^2 = 0.9991$. Adopted with permission from [43]. ©2022, Elsevier

Concentration measurements by multi angle dynamic light scattering

Due to direct availability of devices and concepts multi angle dynamic light scattering was chosen for comparison with the single-particle tracking approach. Particle concentrations can be also obtained with this method as literature [22–24] and manufacturers are stating. Comparing to the particle tracking approach the Zetasizer Ultra was not able to quantify particles in similar concentration ranges. As preliminary experiments showed, particle concentrations as low as quantified by single-particle tracking did not deliver trustworthy results performing MADLS. Consequently, higher particle concentrations had to be selected. Nevertheless, the original PMMA particle suspension represented the stock all analyzed particle concentrations were diluted from.

In Fig. 5.16 particle concentrations obtained from the five different dilution steps are shown. In contrast to particle tracking and to equalize high fluctuating particle counts within the diluted sample each dilution step was analyzed nine times.

Concluding from Fig. 5.16 MADLS measurements and respective particle concentrations are also showing a linear behavior as expected. Comparing both

methods, the significant difference is in the measurable concentration range. Particle concentrations at least a factor of 100 higher compared to single-particle tracking are necessary for MADLS to measure reliable particle counts. Furthermore, in MADLS precision and reproducibility are much lower in terms of fluctuation in measured concentrations among the samples. Comparing relative standard deviations between Fig. 5.15 and Fig. 5.16 makes this clear (largest relative standard deviations: Fig. 5.15 = 11.67%; Fig. 5.16 = 49.45%).

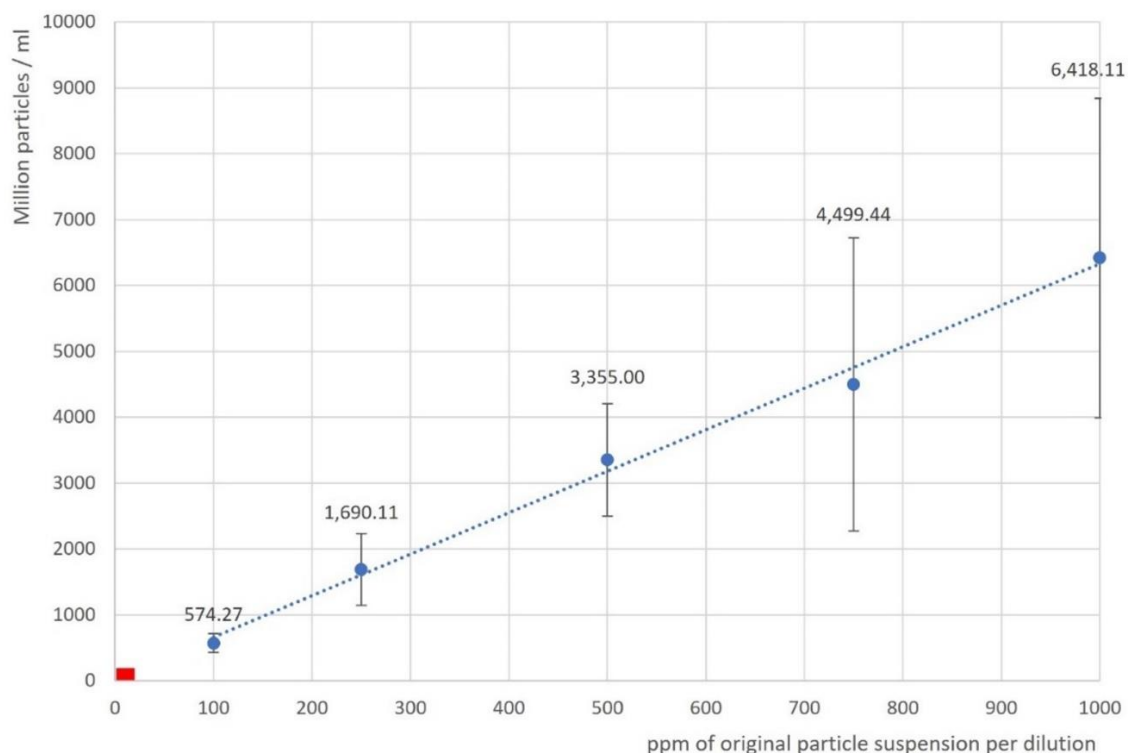


Fig. 5.16. Multi angle dynamic light scattering results for concentration measurements of used PMMA particles. The different concentrations are diluted ($n = 9$) from a stock suspension (82.49 mg mL^{-1}) and resulting in $0.08249 \text{ mg mL}^{-1}$, $0.0618675 \text{ mg mL}^{-1}$, $0.041245 \text{ mg mL}^{-1}$, $0.0206225 \text{ mg mL}^{-1}$, and $0.008249 \text{ mg mL}^{-1}$. The observation range by single particle tracking is indicated by the red rectangle. $R^2 = 0.9944$. Adopted with permission from [43]. ©2022, Elsevier

Verifying obtained particle concentrations by a gravimetric approach

Particle concentrations obtained by single-particle tracking were reviewed by using an alternative quantification method. A gravimetric method was used to estimate the number of particles per volume. 1 mL of monodisperse PMMA particle suspension was freeze-dried, and the weight of the dry particle mass was determined. Particle diameter was measured using TEM and particle density was measured using AUC and gas pycnometry. Using those determined values an average weight of a single particle could be calculated. This allowed the conversion of 1 mL freeze-dried particle suspension and its respective mass into a particle number. For the entire calculation

homogeneity in particle size and mass is obligatory. Therefore, previously shown monodisperse PMMA particles were used [41,42].

Fig. 5.17 is summarizing the measured average particle size obtained by TEM micrographs (Fig. 5.3). Average particle size and average particle mass in 1 mL suspension was found to be 267.03 ± 9.79 nm and 82.49 ± 2.39 mg (see table 5.2).

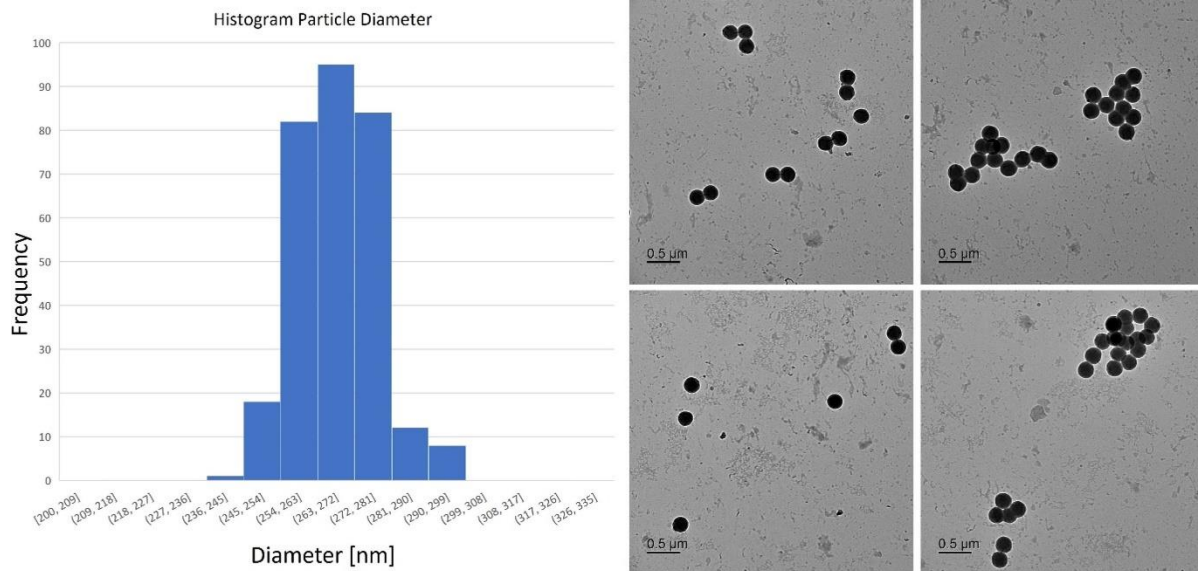


Fig. 5.17. Particle diameter distribution obtained by measuring the displayed TEM micrographs using ImageJ. Histogram relies on 300 measured particle diameters. Adopted with permission from [43]. ©2022, Elsevier

Table 5.2. Particle mass per 1 mL monodisperse PMMA core-shell particle suspension. Table adopted with permission from [43]. ©2022, Elsevier

Measurement	Value [mg]
1	82.938
2	78.690
3	81.789
4	85.439
5	85.270
6	80.813
Average	82.490 ± 2.39

The AUC measurement of the mentioned particles in two different dispersants of known density and viscosity resulted in a distribution of sedimentation coefficients. From those distribution curves (see Fig. 5.12) and the average values of their respective gaussian fits ($H_2O = 6.91 \cdot 10^{-10}$ s and $H_2O/D_2O = 4.51 \cdot 10^{-10}$ s) a particle density of 1.172 ± 0.014 g cm^{-3} could be extracted. Regarding the density of a solid PMMA block (1.185 g cm^{-3}) measured by Chung et al. [54] the AUC obtained value is

very close. Swelling behavior in water and rhodamine B functionalization of the PMMA already suggested a lower density compared to the density of pure and dry PMMA. In aqueous environments swelling of PMMA is described between 1.5% and 3% according to literature [55–57]. After an assumed swelling of 3% PMMA density can be calculated to 1.178 g cm^{-3} . Comparing this predicted value to the measured one it fits well still considering a possibility of slight differences in polymer density due to rhodamine B functionalization.

AUC measurements of PLGA nanoparticles resulted in a particle density of 1.276 g cm^{-3} . This value was calculated from the maximum values in the respective curves in Fig. 5.13 ($\text{H}_2\text{O} = 2.29 \cdot 10^{-10} \text{ s}$ and $\text{H}_2\text{O}/\text{D}_2\text{O} = 1.74 \cdot 10^{-10} \text{ s}$). According to the literature density value of PLGA (1.34 g cm^{-3}) [58] the measured value is comprehensible. A slightly smaller value can be explained by the swelling of PLGA in aqueous environments [59] and the attached stabilizer molecules on the particle surface having a potential for slowing down the sedimentation velocity by acting as a molecular parachute. Calculating the density using the maximum values demonstrates that the solvent approach can also be used for broader distributed particle collectives. Thus, AUC can be applied to many spherical and particle based drug formulations lacking often respective density values.

Due to the fact, that TEM particle size measurements of PMMA particles were carried out in dry state, but in contrast to that, AUC density measurements were carried out under aqueous conditions, an alternative density determination in dry state was desirable. Gas pycnometry was chosen for this purpose. Dry PMMA particle density obtained by gas pycnometry resulted in an average value of $1.224 \pm 0.026 \text{ g cm}^{-3}$ (single values ranging between 1.284 g cm^{-3} and 1.202 g cm^{-3}). The range of obtained values indicated a lower precision compared to AUC.

Concluding density determination, AUC obtained density values are below values for dry PMMA due to swelling under aqueous conditions, and gas pycnometry obtained values are above the literature value. For further calculations the literature value of dry PMMA was chosen deliberately, as it is between AUC and gas pycnometry density values. It is obvious by comparing the calculated particle numbers based on the three different density values (see Fig. 5.18), that slight differences in absolute calculated particle concentrations statistically do not play a significant role. Furthermore, comparing them to single-particle tracking and MADLS they are not differing significantly as well ($p = 0.468$). Based on the chosen PMMA density literature value the particle concentration of the stock PMMA particle suspension was calculated. Obtained by the gravimetric quantification approach the average particle concentration of this particle suspension resulted in $6.98 \cdot 10^{12} \text{ particles mL}^{-1}$.

In comparison to that, particle concentrations obtained by single-particle tracking or MADLS were multiplied by the dilution factor of the respective sample. All the received average concentrations displaying the concentration of the original PMMA suspension either calculated back from different analyzed dilutions or obtained gravimetrically are shown in the next subsection in Fig. 5.18.

Evaluation of the data

For evaluation of significant differences between all determined values an ANOVA was performed. No significant difference between the values was shown confirmed by a p-value = 0.468 (Fig. 5.18). Displaying no significant difference among the concentration values a post-hoc test was considered as not needed. Comparing average particle concentrations, the gravimetric approach predicted the highest concentration (particle tracking: $6.60 \cdot 10^{12}$ particles mL⁻¹, MADLS: $6.33 \cdot 10^{12}$ particles mL⁻¹, gravimetric: $6.98 \cdot 10^{12}$ particles mL⁻¹). By comparing MADLS and single-particle tracking, single-particle tracking resulted in a higher average value than MADLS being closer to the gravimetric approach (Fig. 5.18). Furthermore, the fluctuation of measured particle concentrations was much higher in MADLS compared to single-particle tracking (see Fig. 5.15 and 5.16) which reveals a lack in precision. Besides, in single-particle tracking accuracy and precision can be improved by enlarging the captured sequence in image numbers leading to a reduction of standard deviations. For previously shown measurements highly reproducible results were obtained due to 10,000 captured images per sequence. But nevertheless, precision in quantification can be further improved by increasing the number of captured images. Emphasizing small standard deviations and the relation in count rates between different particle concentrations it becomes clear that particle quantification based on single-particle tracking is a robust method even for highly diluted nanosuspensions.

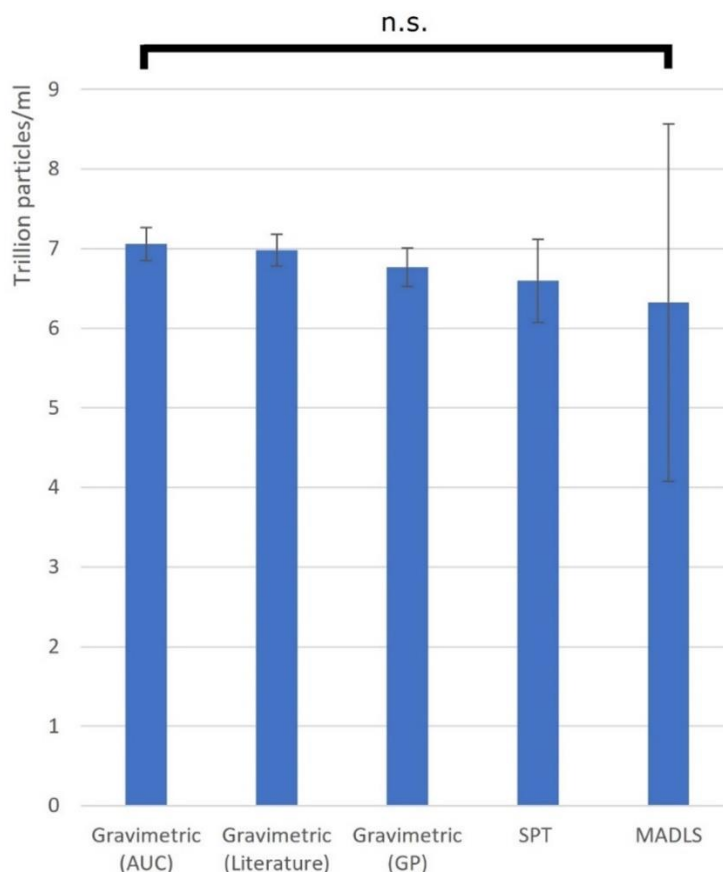


Fig. 5.18. Average particle concentrations and standard deviations are shown. They are calculated from all performed gravimetric measurements using the different density values from analytical ultracentrifugation (AUC), gas pycnometry (GP), or literature and are compared to particle concentrations obtained by single-particle tracking (SPT) and multi angle dynamic light scattering (MADLS). A p-value = 0.468 considered as non-significant resulted from a one-way analysis of variance (ANOVA) to an alpha-value of 0.05. Adopted with permission from [43]. ©2022, Elsevier

Single-particle tracking of benchtop produced acetalated maltodextrin nanoparticles

Representing the undiluted sample, the particle concentration obtained by single-particle tracking results in $2.04 \cdot 10^{12}$ particles mL^{-1} (SD = $1.50 \cdot 10^{11}$ particles mL^{-1}) (see Fig. 5.19). MADLS was used for crosschecking the concentration value. Obtaining a value of $1.89 \cdot 10^{12}$ particles mL^{-1} the earlier measured concentration was affirmed. Measured average values are not perfectly matching, but the trend was continued, which already was found in PMMA particle quantification. The concentrations obtained by MADLS measurements were slightly lower. In addition, MADLS showed a much higher standard deviation compared to single-particle tracking. Consequently, an ANOVA could find no significant difference between both measured average concentrations ($p = 0.808$). MADLS used for crosschecking single-particle tracking measurements revealed that single-particle tracking can also be utilized for the concentration determination of real drug delivery systems owning broader particle distributions and lacking optimized fluorescence.

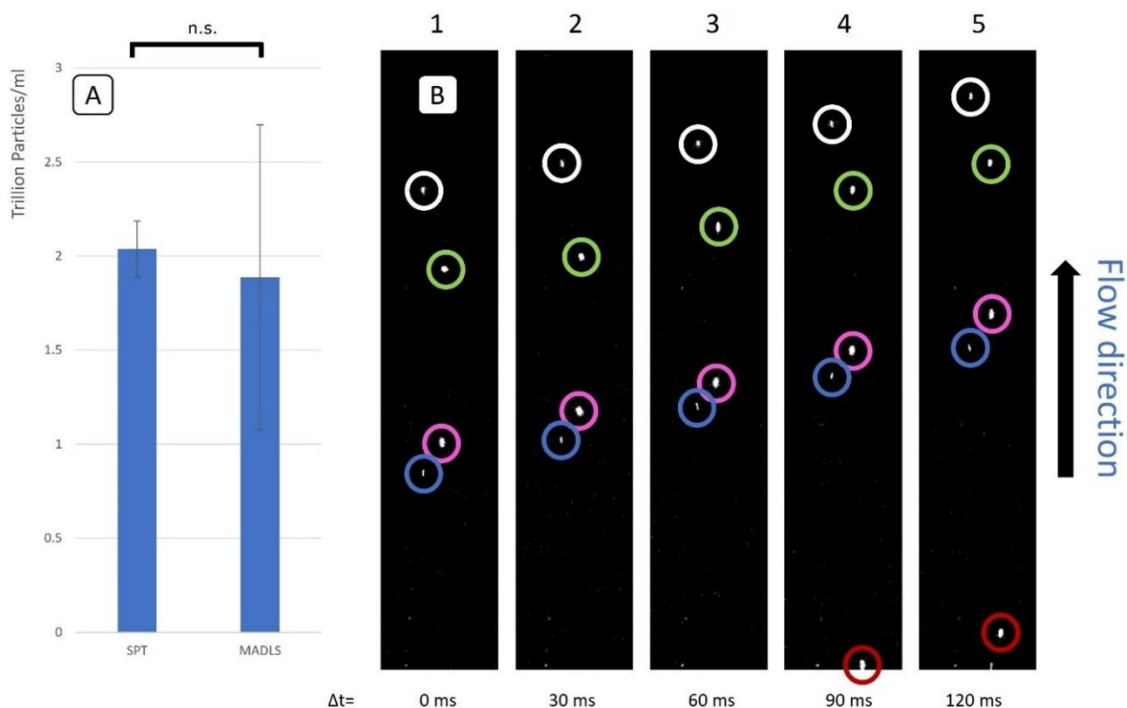


Fig. 5.19. A) SPT and MADLS obtained particle concentrations of undiluted acetalated maltodextrin particles loaded with coumarin 6. SPT: 2.04×10^{12} particles mL^{-1} , MADLS: 1.89×10^{12} particles mL^{-1} . Both measurements in comparison ($n = 3$) can verify the particle concentrations obtained by the SPT approach. A p -value = 0.808 resulting from an ANOVA confirms, that no significant difference exists between both measurement types.

B) One microfluidic channel used for SPT with benchtop produced coumarin 6 loaded acetalated maltodextrin particles inside. Particles appear very bright and are easy to detect. White, green, pink, and blue circles each are highlighting a particle moving through the quantification area. One particle entering the visualized volume is highlighted by the red circle. Adopted with permission from [43]. ©2022, Elsevier

Single-particle tracking of microfluidic produced acetalated maltodextrin nanoparticles

Single-particle tracking based quantification of the sample provided a particle number concentration of 4.64×10^{10} particles mL^{-1} ($\text{SD} = 7.72 \times 10^9$ particles mL^{-1}). This concentration represents the number concentration of the freshly prepared and undiluted nanosuspension. Particles in the analyzed samples provided high fluorescence intensities leading to uncomplicated particle detection (see Fig. 5.20). The shift in particle concentration between both acetalated maltodextrin particle collectives (benchtop and microfluidic) can be attributed to the fact that benchtop produced particles contained a nearly ten times higher mass concentration (4.27 mg mL^{-1}) in comparison to microfluidic produced particles (0.50 mg mL^{-1}). Furthermore, both formulations differed in particle size. Microfluidic manufactured particles showed a z -average of $\sim 220 \text{ nm}$ and benchtop produced ones showed just $\sim 180 \text{ nm}$. Both values were obtained by the Zetasizer. From this shift of the particle

distribution curve, it can be concluded that larger particles showing a much higher volume and mass content of the overall used particle material resulting in lower particle numbers generally.

At this point the results show that in terms of manufacturing it is possible to prepare a nanosuspension carrying a drug substance which, first, can be used as a final drug product, and second, is produced by using the developed microfluidic system from chapter three. And in terms of analytics, it is possible to quantify the real number of particles inside the sample directly after preparation.

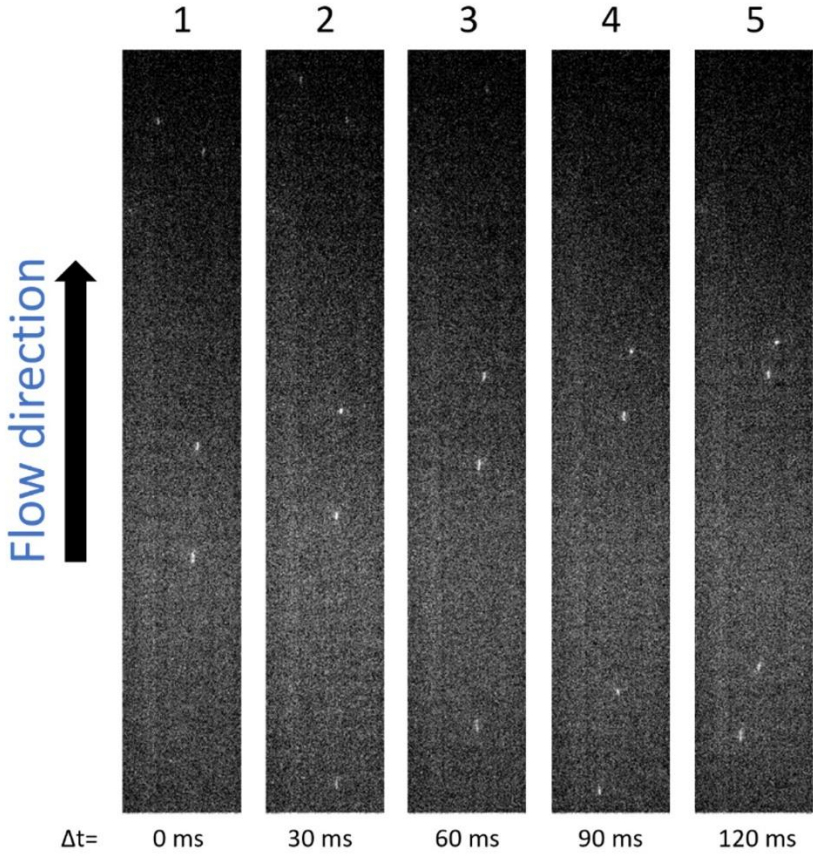


Fig. 5.20. A microfluidic channel used for SPT with microfluidic manufactured coumarin 6 loaded acetalated maltodextrin particles inside. Particles appear very bright and are easy to detect.

5.3.2 Dark-field microscopy

5.3.2.1 Methods

Dark-field microscopy

To challenge the detection limits of the single-particle tracking quantification approach, the detection method was changed to dark-field imaging. This was done desiring a quantification of particles containing no fluorescence active substances. Conserving the ability to also count these particles, dark-field detection seems appropriate. However, a sufficient light scattering caused by particles is mandatory for an efficient particle detection. Elastic light scattering intensity of a single particle (particles must be spheres smaller than the wavelength of light) can be calculated by the Rayleigh approximation [60]:

$$I = I_0 \left(\frac{1 + \cos^2 \theta}{2R^2} \right) \left(\frac{2\pi}{\lambda} \right)^4 \left(\frac{n^2 - 1}{n^2 + 2} \right)^2 \left(\frac{d}{2} \right)^6$$

Where I is the intensity of the scattered light, I_0 is the intensity of the light hitting the particle, θ is the scattering angle, R is the distance between observer and particle, λ is the wavelength, n is the refractive index of the particle material, and d is the diameter of the respective particle.

The scattering intensity is depending on the particle radius to the power of 6. Thus, for smaller particles it is highly challenging to detect them due to the low intensity of scattered light [60].

As shown in Fig. 5.21 dark-field microscopy relies on focusing a ring-shaped light beam on the sample in a way that all light, which is not influenced by any sample, is directed away from the microscope's objective [39,40]. If no sample would be in the focus of the light beam the image captured by the objective would be completely dark. A sample in the focus leads to interaction with light. In general absorption, reflection, refraction, diffraction, or scattering can occur [61]. Even if particles are smaller than the wavelength of irradiating light, they still have the ability to scatter photons in every direction [61]. This fact is to be exploited for the detection and quantification of nanoparticles. Photons, which are directed towards the objective creating an image to be captured enabling the detection of particles. Additionally, using dark-field microscopy a particle smaller than the resolution limit of the used microscope still can be detected. This is caused by the ability to detect light scattered by the particle giving an information about the localization of the particle, even if there is no further morphological information about the respective particle [62].

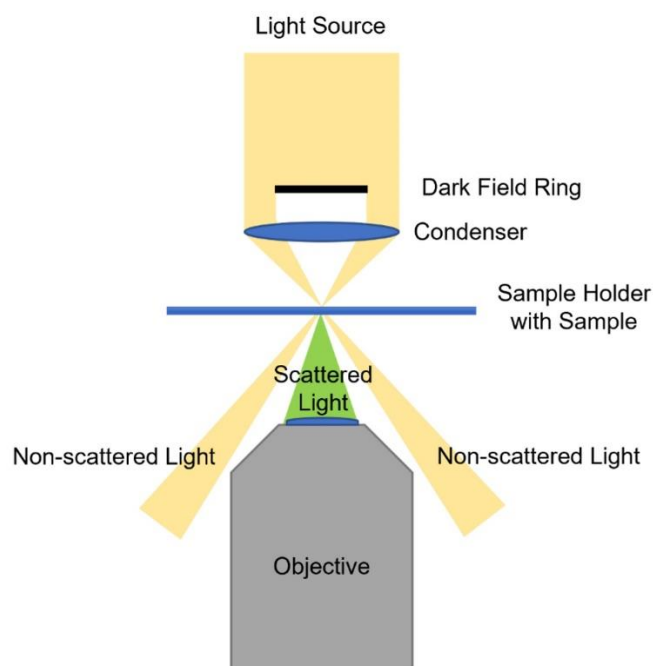


Fig. 5.21. Schematic overview of dark-field microscopy for particle quantification used in this study.

Characterization of the used nanosuspension

For challenging single-particle tracking quantification in dark-field mode particles providing intentionally a very small particle size were selected. Still, they should offer the opportunity to be tracked in parallel by using fluorescence microscopy for crosschecking the obtained particle numbers. For this purpose, commercially available polystyrene particles were chosen (P(S/V-COOH) by Bangs Laboratories, Inc., Fishers, Indiana, USA). Manufacturer information speaking of monodisperse particles in a size of ~110 nm labeled with Dragon Green as a fluorescent dye. Specified particle sizes and monodispersity were checked by visualization based on TEM imaging.

Carbon coated copper grids were used for TEM sample preparation and polystyrene particles were diluted and drop-casted on the respective grids. Particles did not require additional staining for particle visualization. For visualization the same TEM (JEOL JEM-2100) equipped with a slow-scan charge-coupled device camera Gatan Orius SC1000 was used in bright field mode as already described before. Operating voltage was set to 200 kV. Obtained micrographs were analyzed using ImageJ.

Sample preparation for single-particle tracking

The original nanosuspension (10 mg mL⁻¹ particle mass concentration) was diluted in an aqueous poloxamer 188 solution (1 mg mL⁻¹) to a mass concentration of 10 ng mL⁻¹. Poloxamer 188 was once again used for lowering surface tensions and increasing slightly the viscosity of the dispersion. In this state the nanosuspension was ready for quantification.

Preparation of microfluidic chips for single-particle tracking

Microfluidic quantification devices were identically manufactured as previously mentioned in fluorescence based single-particle tracking quantification of rhodamine B labeled PMMA particles [44].

Performing single-particle tracking for particle quantification

Fluorescent polystyrene particles were quantified using single-particle tracking very similar to the previously mentioned PMMA particle quantification. For maintaining a particle flow through the quantification channel, the Microfluidic Flow Controller OB1 MK3+ from Elveflow was used again. Likewise, particle speed inside the channel was tuned manually by increasing or decreasing the pressure to a usable velocity (pressure range between 5.0 and 15.0 mbar). A section of the channel was chosen randomly for capturing an image sequence while particles passing by. The channel depth of the used quantification channel was identical to the previously SEM measured depth delivering a well-known volume inside the captured channel area. First, particle fluorescence was used for particle detection. Dragon green as fluorescent dye loaded on the particles resembles fluorescein isothiocyanate (FITC) in excitation and emission wave lengths very much making it possible to use an FITC filter cube with the microscope (Eclipse Ti-S, Nikon Instruments) for detection. The filter cube suited for FITC provides the following specifications: 482/35 BrightLine HC, a dichroic mirror: HC 506, and an emission filter: 536/40 BrightLine HC, all from AHF Germany). Using the Dragon Green adapted fluorescence detection, the particle quantification based on single-particle tracking was carried out exactly as performed on rhodamine B labeled PMMA particles.

After capturing the image sequence for fluorescence-based particle quantification the detection mode was switched from fluorescence to dark-field. The identical sample, channel, microscope, objective, and pumping settings were used. The only difference in particle detection was the detection method. A dark-field condenser (Dry 0.95-0.80, Nikon Instruments Europe, Amsterdam, Netherlands) was installed, and the quantification channel was visualized using dark-field microscopy. As light source a LED was used. According to the already performed fluorescence-based quantification another image sequence (10,000 images) relying now on dark-field imaging was captured while particles were moving through the channel. After both image sequences were captured, they were compared back-to-back.

5.3.2.2 Results and discussion

Particle properties

Particles were predicted by the manufacturer to be spheres of ~110 nm. As shown in Fig. 5.22 this could be verified. Furthermore, homogeneity in particle size could be shown as well. This was crucial to ensure that larger particles were excluded from the sample leaving only small particles to be detected for challenging dark-field microscopy with small particle sizes. For direct comparison of fluorescence and dark-field based single-particle tracking quantification polystyrene particles had to provide a strong fluorescence signal. Due to Dragon Green labeling this could be facilitated (see Fig. 5.23). Concluding, this sample appeared perfectly suited for the experiment.

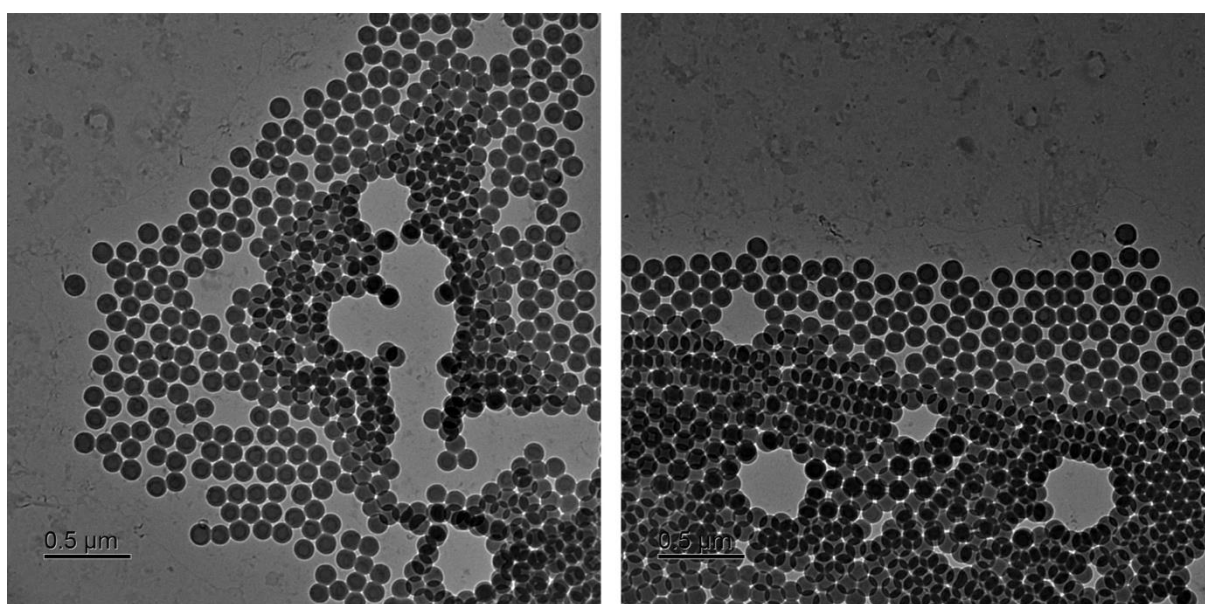


Fig. 5.22. TEM micrographs of Dragon Green labeled polystyrene particles. The manufacturer claimed particles of ~110 nm which could be verified. Particles appear very homogeneous in size as desired.

Particle visualization using fluorescence

Fluorescence detection was very successful for this type of particles. The earlier mentioned FITC filter cube fitted the wavelengths for excitation and emission regarding Dragon Green precisely. In addition to that the fluorescence quantum yield appeared very high as well. This made it easy to keep camera exposure times short (20 ms) preserving a dark background to raise the contrast to single bright objects in the image. Consequently, and referring to Fig. 5.23 polystyrene particles were visible as clear bright spots in front of a dark background.

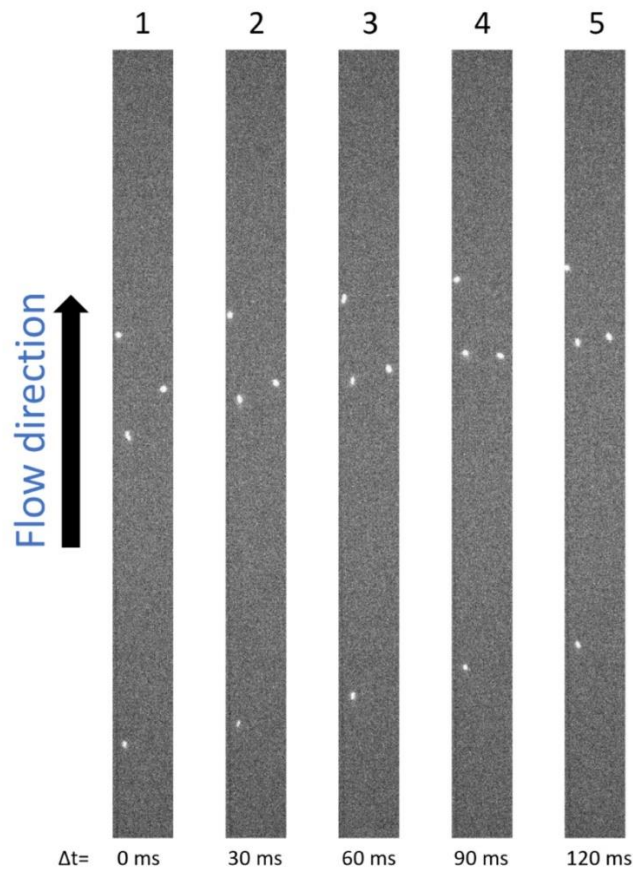


Fig. 5.23. Fluorescently labeled polystyrene nanoparticles moving through a microfluidic channel visualized by fluorescence microscopy. Particles are clearly visible as bright spots moving forward from image to image.

Particle visualization using dark-field

Fig. 5.24 shows small but bright objects inside of the channel. Due to immobilization (no change in position from image to image) those objects were not considered as particles. Besides that, no moving objects (polystyrene particles) could be detected in the sequence at all. This leads to the conclusion that particle scattering intensity was below the scattering noise caused by the quantification channel itself. Most likely, the dot-like structures result from scattering of impurities and dust attached to the channel borders. Larger scattering objects like the one in the mid part of the visualized channel section is outshining all smaller scattering signals due to the high scattering intensity and interference rings. Comparing fluorescence based and dark-field based particle detection it can be concluded that fluorescence detection is much more effective especially when it comes to distinguish particles from the image background. Overall, the dark-field based setup it is not capable of detecting particles in a size range around 100 nm and below. To facilitate single-particle tracking quantification based on dark-field microscopy, quantification channels must be improved to exclude strong light scattering by the quantification device itself.

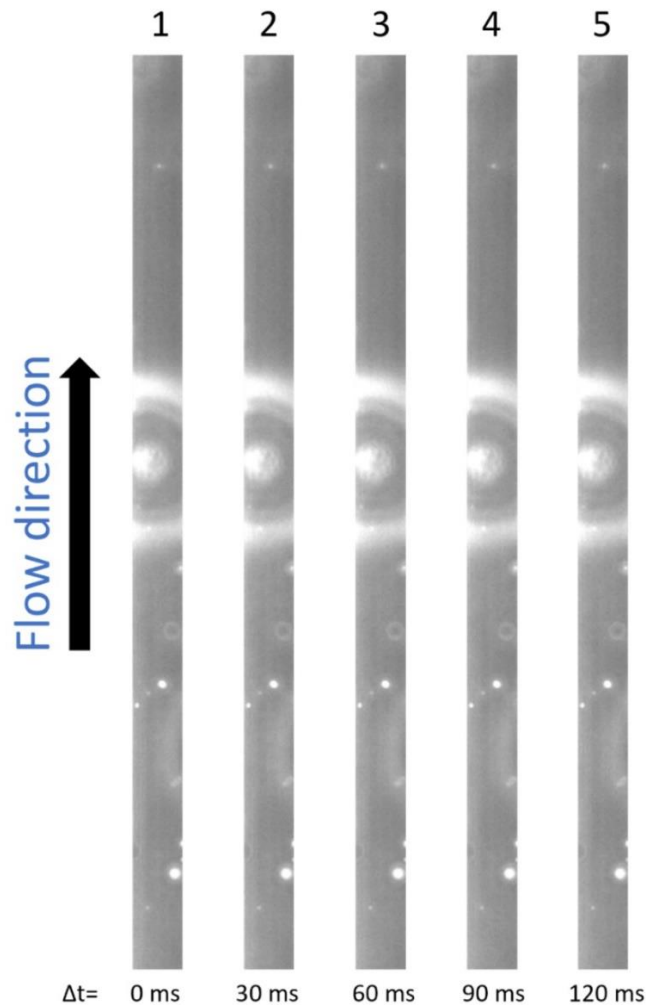


Fig. 5.24. Fluorescently labeled polystyrene nanoparticles moving through the identical microfluidic channel as in Fig. 5.23. Particles cannot be visualized using dark-field microscopy. Channel borders, imperfections, and impurities of the microfluidic counting device scatter in much higher intensities compared to the particles to be counted. Particles are simply outshined and therefore not visible.

Evaluation of the data

Without any further MATLAB analysis of the obtained image sequences, it becomes clear that a drastic difference between both detection methods exists. Perfectly visible particles detected by using fluorescence vanished immediately after switching to dark-field detection. This is even more impressive keeping in mind that the quantification equipment (quantification channel, microscope, and objective) and the sample remained the same. It is obvious that the intensity of scattered light was much lower compared to the intensity of emitted fluorescence light. Due to the great influence of the particle diameter on the scattering intensity this is comprehensible [60]. Nevertheless, particle detection based on light scattering is extensively reported in literature. The best example for this is NTA. It relies on light scattering of particles to be analyzed. Nevertheless, particles in the desired size range can be characterized using this method [21]. A great issue in the previously performed experiments is the

weak scattering intensity of characterized particles. It shows a lower intensity in comparison to the scattered light from further scattering objects like impurities in the channels, little cracks in the silicone, or inaccuracies in the molding of the device. Without excluding these sources of extensive light scattering visualization of nanoparticles and quantification via dark-field imaging cannot be facilitated. The system could be improved by using microfluidic quantification channels which offer the needed requirements. An example would be a channel made of glass with polished channel borders to avoid defects and impurities inside the channel. This would also enable the use of a stronger light source. Without additional sources of light scattering particles could be better detected in front of a darker background and would not be outshined as in previous experiments. A stronger light source like a laser instead of an LED could increase the scattering signal additionally making nanoparticles easier to detect. Applying these improvements to the quantification setup a nanoparticle quantification based on dark-field single-particle tracking could be facilitated in the future. As an outlook for the already investigated setup it would be interesting to find out where the detection threshold regarding particle size is set. By analyzing different increasing particle sizes (particles still must be monodisperse) a specific size could be determined facilitating a dark-field based particle quantification.

5.4 References

- [1] J.A. Loureiro, M.C. Pereira, PLGA Based Drug Carrier and Pharmaceutical Applications: The Most Recent Advances, *Pharmaceutics*. 12 (2020) 903. <https://doi.org/10.3390/PHARMACEUTICS12090903>.
- [2] K.K. Chereddy, V.L. Payen, V. Pr eat, PLGA: From a classic drug carrier to a novel therapeutic activity contributor, *Journal of Controlled Release*. 289 (2018) 10–13. <https://doi.org/10.1016/J.JCONREL.2018.09.017>.
- [3] S. Gelperina, K. Kisich, M.D. Iseman, L. Heifets, The Potential Advantages of Nanoparticle Drug Delivery Systems in Chemotherapy of Tuberculosis, *Am J Respir Crit Care Med*. 172 (2012) 1487–1490. <https://doi.org/10.1164/RCCM.200504-613PP>.
- [4] A.T. Florence, Issues in Oral Nanoparticle Drug Carrier Uptake and Targeting, *J Drug Target*. 12 (2004) 65–70. <https://doi.org/10.1080/10611860410001693706>.
- [5] U. Schr oder, B.A. Sabel, Nanoparticles, a drug carrier system to pass the blood-brain barrier, permit central analgesic effects of i.v. dalargin injections, *Brain Res*. 710 (1996) 121–124. [https://doi.org/10.1016/0006-8993\(95\)01375-X](https://doi.org/10.1016/0006-8993(95)01375-X).
- [6] J. Hu, K.P. Johnston, R.O. Williams, Nanoparticle Engineering Processes for Enhancing the Dissolution Rates of Poorly Water Soluble Drugs, *Drug Dev Ind Pharm*. 30 (2004) 233–245. <https://doi.org/10.1081/DDC-120030422>.
- [7] A.C. Anselmo, S. Mitragotri, Nanoparticles in the clinic, *Bioeng Transl Med*. 1 (2016) 10–29. <https://doi.org/10.1002/BTM2.10003>.
- [8] S. Behzadi, V. Serpooshan, W. Tao, M.A. Hamaly, M.Y. Alkawareek, E.C. Dreaden, D. Brown, A.M. Alkilany, O.C. Farokhzad, M. Mahmoudi, Cellular uptake of nanoparticles: journey inside the cell, *Chem Soc Rev*. 46 (2017) 4218–4244. <https://doi.org/10.1039/C6CS00636A>.

- [9] N. Lababidi, V. Sigal, A. Koenneke, K. Schwarzkopf, A. Manz, M. Schneider, Microfluidics as tool to prepare size-tunable PLGA nanoparticles with high curcumin encapsulation for efficient mucus penetration, *Beilstein Journal of Nanotechnology*. 10 (2019) 2280–2293. <https://doi.org/10.3762/BJNANO.10.220>.
- [10] G.M. Whitesides, The origins and the future of microfluidics, *Nature*. 442 (2006) 368–373. <https://doi.org/10.1038/nature05058>.
- [11] W.I. Goldberg, Dynamic light scattering, *Am J Phys*. 67 (1999) 1152–1160. <https://doi.org/10.1119/1.19101>.
- [12] J. Lim, S.P. Yeap, H.X. Che, L.S. Chun, Characterization of magnetic nanoparticle by dynamic light scattering, *Nanoscale Res Lett*. 8 (2013) 381. <https://doi.org/https://doi.org/10.1186/1556-276X-8-381>.
- [13] A. Dubes, H. Parrot-Lopez, W. Abdelwahed, G. Degobert, H. Fessi, P. Shahgaldian, A.W. Coleman, Scanning electron microscopy and atomic force microscopy imaging of solid lipid nanoparticles derived from amphiphilic cyclodextrins, *European Journal of Pharmaceutics and Biopharmaceutics*. 55 (2003) 279–282. [https://doi.org/10.1016/S0939-6411\(03\)00020-1](https://doi.org/10.1016/S0939-6411(03)00020-1).
- [14] F.J. Giessibl, Advances in atomic force microscopy, *Rev Mod Phys*. 75 (2003) 949–983. <https://doi.org/10.1103/RevModPhys.75.949>.
- [15] V. Filipe, A. Hawe, W. Jiskoot, Critical evaluation of nanoparticle tracking analysis (NTA) by NanoSight for the measurement of nanoparticles and protein aggregates, *Pharm Res*. 27 (2010) 796–810. <https://doi.org/10.1007/s11095-010-0073-2>.
- [16] P. Kramerberger, M. Ciringer, A. Strancar, M. Peterka, Evaluation of nanoparticle tracking analysis for total virus particle determination, *Virology*. 9 (2012) 1–10. <https://doi.org/10.1186/1743-422X-9-265>.
- [17] Y. Pei, R. Vogel, C. Minelli, Tunable resistive pulse sensing (TRPS), *Characterization of Nanoparticles: Measurement Processes for Nanoparticles*. (2020) 117–136. <https://doi.org/10.1016/B978-0-12-814182-3.00009-2>.
- [18] W. Anderson, R. Lane, D. Korbie, M. Trau, Observations of Tunable Resistive Pulse Sensing for Exosome Analysis: Improving System Sensitivity and Stability, *Langmuir*. 31 (2015) 6577–6587. <https://doi.org/10.1021/ACS.LANGMUIR.5B01402>.
- [19] E. Weatherall, G.R. Willmott, Applications of tunable resistive pulse sensing, *Analyst*. 140 (2015) 3318–3334. <https://doi.org/10.1039/C4AN02270J>.
- [20] R.A. Dragovic, C. Gardiner, A.S. Brooks, D.S. Tannetta, D.J.P. Ferguson, P. Hole, B. Carr, C.W.G. Redman, A.L. Harris, P.J. Dobson, P. Harrison, I.L. Sargent, Sizing and phenotyping of cellular vesicles using Nanoparticle Tracking Analysis, *Nanomedicine*. 7 (2011) 780–788. <https://doi.org/10.1016/j.nano.2011.04.003>.
- [21] C. Gardiner, Y.J. Ferreira, R.A. Dragovic, C.W.G. Redman, I.L. Sargent, Extracellular vesicle sizing and enumeration by nanoparticle tracking analysis, *J Extracell Vesicles*. 2 (2013). <https://doi.org/10.3402/jev.v2i0.19671>.
- [22] V. Palmieri, D. Lucchetti, I. Gatto, A. Maiorana, M. Marcantoni, G. Maulucci, M. Papi, R. Pola, M. de Spirito, A. Sgambato, Dynamic light scattering for the characterization and counting of extracellular vesicles: a powerful noninvasive tool, *Journal of Nanoparticle Research*. 16 (2014). <https://doi.org/10.1007/s11051-014-2583-z>.
- [23] M. Heinlaan, K. Kasemets, V. Aruoja, I. Blinova, O. Bondarenko, A. Lukjanova, A. Khosrovyan, I. Kurvet, M. Pullerits, M. Sihtmäe, G. Vasiliev, H. Vija, A. Kahru, Hazard evaluation of polystyrene

nanoplastic with nine bioassays did not show particle-specific acute toxicity, *Science of The Total Environment*. 707 (2020) 136073. <https://doi.org/10.1016/J.SCITOTENV.2019.136073>.

- [24] I. Makra, P. Terejanszky, R.E. Gyurcsanyi, A method based on light scattering to estimate the concentration of virus particles without the need for virus particle standards, *MethodsX*. 2 (2015) 91–99. <https://doi.org/10.1016/J.MEX.2015.02.003>.
- [25] M. Rauma, T.S. Isaksson, G. Johanson, A new technique to assess dermal absorption of volatile chemicals in vitro by thermal gravimetric analysis, *Toxicology in Vitro*. 20 (2006) 1183–1189. <https://doi.org/10.1016/J.TIV.2006.03.004>.
- [26] P.E. Rasmussen, H.D. Gardner, J. Niu, Buoyancy-Corrected Gravimetric Analysis of Lightly Loaded Filters, *J Air Waste Manage Assoc*. 60 (2012) 1065–1077. <https://doi.org/10.3155/1047-3289.60.9.1065>.
- [27] C. Manzo, M.F. Garcia-Parajo, A review of progress in single particle tracking: From methods to biophysical insights, *Reports on Progress in Physics*. 78 (2015) 124601. <https://doi.org/10.1088/0034-4885/78/12/124601>.
- [28] K. Forier, A.S. Messiaen, K. Raemdonck, H. Deschout, J. Rejman, F. De Baets, H. Nelis, S.C. De Smedt, J. Demeester, T. Coenye, K. Braeckmans, Transport of nanoparticles in cystic fibrosis sputum and bacterial biofilms by single-particle tracking microscopy, *Nanomedicine*. 8 (2013) 935–949. <https://doi.org/10.2217/nnm.12.129>.
- [29] K. Braeckmans, K. Buyens, W. Bouquet, C. Vervaet, P. Joye, F. De Vos, L. Plawinski, L. Doeuvre, E. Angles-Cano, N.N. Sanders, J. Demeester, S.C. De Smedt, Sizing nanomatter in biological fluids by fluorescence single particle tracking, *Nano Lett*. 10 (2010) 4435–4442. <https://doi.org/10.1021/nl103264u>.
- [30] F. Franks, Freeze-drying of bioproducts: putting principles into practice, *European Journal of Pharmaceutics and Biopharmaceutics*. 45 (1998) 221–229. [https://doi.org/10.1016/S0939-6411\(98\)00004-6](https://doi.org/10.1016/S0939-6411(98)00004-6).
- [31] S.B. Rice, C. Chan, S.C. Brown, P. Eschbach, L. Han, D.S. Ensor, A.B. Stefaniak, J. Bonevich, A.E. Vladar, A.R.H. Walker, J. Zheng, C. Starnes, A. Stromberg, J. Ye, E.A. Grulke, Particle size distributions by transmission electron microscopy: an interlaboratory comparison case study, *Metrologia*. 50 (2013) 663–678. <https://doi.org/10.1088/0026-1394/50/6/663>.
- [32] A.K. Boehm, E. Ionescu, M. Koch, M. Gallei, Combining Soft Polysilazanes with Melt-Shear Organization of Core–Shell Particles: On the Road to Polymer-Templated Porous Ceramics, *Molecules*. 24 (2019) 3553. <https://doi.org/10.3390/MOLECULES24193553>.
- [33] P.H. Brown, P. Schuck, Macromolecular Size-and-Shape Distributions by Sedimentation Velocity Analytical Ultracentrifugation, *Biophys J*. 90 (2006) 4651–4661. <https://doi.org/10.1529/BIOPHYSJ.106.081372>.
- [34] J. Lebowitz, M.S. Lewis, P. Schuck, Modern analytical ultracentrifugation in protein science: A tutorial review, *Protein Science*. 11 (2002) 2067–2079. <https://doi.org/10.1110/PS.0207702>.
- [35] T.M. Laue, W.F. Stafford III, Modern Applications of Analytical Ultracentrifugation, *Annu Rev Biophys Biomol Struct*. 28 (1999) 75–100. <https://doi.org/10.1146/ANNUREV.BIOPHYS.28.1.75>.
- [36] C.R. Bilchak, E. Buenning, M. Asai, K. Zhang, C.J. Durning, S.K. Kumar, Y. Huang, B.C. Benicewicz, D.W. Gidley, S. Cheng, A.P. Sokolov, M. Minelli, F. Doghieri, Polymer-Grafted Nanoparticle Membranes with Controllable Free Volume, *Macromolecules*. 50 (2017) 7111–7120. <https://doi.org/10.1021/ACS.MACROMOL.7B01428>.

- [37] J.S. An, W.J. Han, H.J. Choi, Synthesis of hollow magnetite nanoparticles via self-assembly and their magnetorheological properties, *Colloids Surf A Physicochem Eng Asp.* 535 (2017) 16–23. <https://doi.org/10.1016/J.COLSURFA.2017.09.019>.
- [38] S.M. Abdel-Hafez, J. Zapp, M. Gallei, M. Schneider, Formulation attributes, acid tunable degradability and cellular interaction of acetalated maltodextrin nanoparticles, *Carbohydr Polym.* 288 (2022) 119378. <https://doi.org/10.1016/J.CARBPOL.2022.119378>.
- [39] P.F. Gao, G. Lei, C.Z. Huang, Dark-Field Microscopy: Recent Advances in Accurate Analysis and Emerging Applications, *Anal Chem.* 93 (2021) 4707–4726. <https://doi.org/10.1021/ACS.ANALCHEM.0C04390>.
- [40] Min Hu, Carolina Novo, Alison Funston, Haining Wang, Hristina Staleva, Shengli Zou, Paul Mulvaney, Younan Xia, G. V. Hartland, Dark-field microscopy studies of single metal nanoparticles : understanding the factors that influence the linewidth of the localized surface plasmon resonance, *J Mater Chem.* 18 (2008) 1949–1960. <https://doi.org/10.1039/B714759G>.
- [41] C.G. Schäfer, B. Viel, G.P. Hellmann, M. Rehahn, M. Gallei, Thermo-cross-linked Elastomeric Opal Films, *ACS Appl Mater Interfaces.* 5 (2013) 10623–10632. <https://doi.org/10.1021/AM402588V>.
- [42] C.G. Schäfer, M. Gallei, J.T. Zahn, J. Engelhardt, G.P. Hellmann, M. Rehahn, Reversible light-, thermo-, and mechano-responsive elastomeric polymer opal films, *Chemistry of Materials.* 25 (2013) 2309–2318. <https://doi.org/10.1021/cm400911j>.
- [43] J. Buescher, T. John, A.K. Boehm, L. Weber, S.M. Abdel-Hafez, C. Wagner, T. Kraus, M. Gallei, M. Schneider, A precise nanoparticle quantification approach using microfluidics and single-particle tracking, *J Drug Deliv Sci Technol.* 75 (2022) 103579. <https://doi.org/10.1016/J.JDDST.2022.103579>.
- [44] J. Friend, L. Yeo, Fabrication of microfluidic devices using polydimethylsiloxane, *Biomicrofluidics.* 4 (2010) 026502. <https://doi.org/10.1063/1.3259624>.
- [45] B.H. Jo, L.M. van Lerberghe, K.M. Motsegood, D.J. Beebe, Three-dimensional micro-channel fabrication in polydimethylsiloxane (PDMS) elastomer, *Journal of Microelectromechanical Systems.* 9 (2000) 76–81. <https://doi.org/10.1109/84.825780>.
- [46] P. Kim, K.W. Kwon, M.C. Park, S.H. Lee, S.M. Kim, K.Y. Suh, Soft lithography for microfluidics: A Review, *Biochip J.* 2 (2008) 1–11.
- [47] S.L. Marusin, Sample preparation — the key to SEM studies of failed concrete, *Cem Concr Compos.* 17 (1995) 311–318. [https://doi.org/10.1016/0958-9465\(95\)00020-D](https://doi.org/10.1016/0958-9465(95)00020-D).
- [48] Z. Zalevsky, Extended depth of focus imaging: a review, *SPIE Reviews.* 1 (2010) 018001. <https://doi.org/10.1117/6.0000001>.
- [49] H. Cölfen, T.M. Laue, W. Wohlleben, K. Schilling, E. Karabudak, B.W. Langhorst, E. Brookes, B. Dubbs, D. Zollars, M. Rocco, B. Demeler, The Open AUC Project, *European Biophysics Journal.* 39 (2010) 347–359. <https://doi.org/10.1007/S00249-009-0438-9>.
- [50] J.L. Cole, J.W. Lary, T. P. Moody, T.M. Laue, Analytical Ultracentrifugation: Sedimentation Velocity and Sedimentation Equilibrium, *Methods Cell Biol.* 84 (2008) 143–179. [https://doi.org/10.1016/S0091-679X\(07\)84006-4](https://doi.org/10.1016/S0091-679X(07)84006-4).
- [51] I. Perevyazko, A. Vollrath, S. Hornig, G.M. Pavlov, U.S. Schubert, Characterization of poly(methyl methacrylate) nanoparticles prepared by nanoprecipitation using analytical ultracentrifugation, dynamic light scattering, and scanning electron microscopy, *J Polym Sci A Polym Chem.* 48 (2010) 3924–3931. <https://doi.org/10.1002/pola.24157>.

- [52] K. Nontapot, V. Rastogi, J.A. Fagan, V. Reipa, Size and density measurement of core-shell Si nanoparticles by analytical ultracentrifugation, *Nanotechnology*. 24 (2013) 155701. <https://doi.org/10.1088/0957-4484/24/15/155701>.
- [53] Walter. Mächtle, L. Börger, *Analytical ultracentrifugation of polymers and nanoparticles*, Springer, 2006.
- [54] J.P. Chung, Y.M. Seong, T.Y. Kim, Y. Choi, T.H. Kim, H.J. Choi, C.H. Min, H. Benmakhlof, K.J. Chun, H.T. Chung, Development of a PMMA phantom as a practical alternative for quality control of gamma knife® dosimetry, *Radiation Oncology*. 13 (2018) 1–9. <https://doi.org/10.1186/s13014-018-1117-8>.
- [55] W.L. Tham, W.S. Chow, Z.A.M. Ishak, Simulated body fluid and water absorption effects on poly(methyl methacrylate)/hydroxyapatite denture base composites, *Express Polym Lett*. 4 (2010) 517–528. <https://doi.org/10.3144/EXPRESSPOLYMLETT.2010.66>.
- [56] K.E. Smith, P. Trusty, B. Wan, K. Gall, Long-term toughness of photopolymerizable (meth)acrylate networks in aqueous environments, *Acta Biomater*. 7 (2011) 558–567. <https://doi.org/10.1016/j.actbio.2010.09.001>.
- [57] M. N’Diaye, F. Pascaretti-Grizon, P. Massin, M.F. Baslé, D. Chappard, Water absorption of poly(methyl methacrylate) measured by vertical interference microscopy, *Langmuir*. 28 (2012) 11609–11614. <https://doi.org/10.1021/LA302260A>.
- [58] M.M. Arnold, E.M. Gorman, L.J. Schieber, E.J. Munson, C. Berkland, NanoCipro encapsulation in monodisperse large porous PLGA microparticles, *Journal of Controlled Release*. 121 (2007) 100–109. <https://doi.org/10.1016/j.jconrel.2007.05.039>.
- [59] C. Bode, H. Kranz, A. Fivez, F. Siepmann, J. Siepmann, Often neglected: PLGA/PLA swelling orchestrates drug release: HME implants, *Journal of Controlled Release*. 306 (2019) 97–107. <https://doi.org/10.1016/j.jconrel.2019.05.039>.
- [60] R.B. Miles, W.R. Lempert, J.N. Forkey, Laser Rayleigh scattering, *Meas Sci Technol*. 12 (2001) R33. <https://doi.org/10.1088/0957-0233/12/5/201>.
- [61] A.R. Jones, Light scattering for particle characterization, *Prog Energy Combust Sci*. 25 (1999) 1–53. [https://doi.org/10.1016/S0360-1285\(98\)00017-3](https://doi.org/10.1016/S0360-1285(98)00017-3).
- [62] R. Fakhrullin, L. Nigamatzyanova, G. Fakhrullina, Dark-field/hyperspectral microscopy for detecting nanoscale particles in environmental nanotoxicology research, *Science of The Total Environment*. 772 (2021) 145478. <https://doi.org/10.1016/j.scitotenv.2021.145478>.

Chapter 6

Summary and outlook

6.1 Particle preparation

The great drawback of a shortage of available amounts of novel drug substances in early development stages was successfully averted by making use of a microfluidic setup. By improving the initial setup based on syringe pumps and implementing an air pressure driven pumping device a process was developed providing a high precision in feeding rates regarding the different utilized fluids. By calculating the volumetric flow rates for all involved capillaries and combining the respective equations to one calculation for the entire system, pressures to be applied for a desired flow rate ratio could be calculated to a precision range of 10 mbar. Furthermore, the addition of the mentioned light microscope to the setup increased the reliability of the microfluidic particle production even more. Agglomerates or blocked capillaries could be detected immediately ensuring a reliable particle production. Utilizing this improved microfluidic setup highly diluted nanosuspensions were produced. Batch sizes of a few microliters were made possible while maintaining a high precision in particle manufacturing. This ensured carrying out formulation experiments in minimal scales receiving very early information about possible drug delivery systems for a respective drug substance.

By implementing the particle purification technique based on the Centriscart system especially highly diluted nanosuspensions could be harvested. The particle loss could be lowered to roughly 1% of the total particle mass which perfectly fits to the original aim to avoid waste of expensive materials during early formulation experiments.

Relying on microfluidic production and an effective and sustainable purification process different particle types could be successfully screened for their potential in acting as a drug delivery system. As a very hydrophobic system (suitable for carrying hydrophobic substances) PLGA particles were produced. In contrast to this, as a very hydrophilic system (suitable for carrying hydrophilic substances) gelatin particles were manufactured. The production of both particle systems was carried out precisely in a reduced scale of few microliters pointing out the ability of the microfluidic setup to act as a platform technology for screening drug delivery systems as carriers for a wide range of physicochemically different drug substances.

By expanding the range of different particle options, the focus was shifted to particles composed of polymers providing opposite charges. Positively charged DEAE-dextran and negatively charged dextran sulfate were effectively used for forming nanoparticles. Utilizing the precise mixing possibilities of the microfluidic setup both polymers could be mixed in a way achieving a specific and aspired particle charge. This option was also exploited developing a delivery system for dsRNA [1,2]. By aiming for a specific mixing ratio combining the negatively charged dsRNA with positively charged DEAE-dextran positively charged nanoparticles could be produced. This positive particle charge led to an effective binding of particles to cell surfaces of *E. coli* being a suitable vehicle for transferring the dsRNA loaded particles into *Paramecium tetraurelia*. The used dsRNA represented a great model drug substance highlighting the potential of the developed delivery system to carry genetic information into the respective cell line.

As a future perspective, this microfluidic particle production setup can be utilized for manufacturing a large variety of particle types. Since, it could be shown that nanoprecipitation could be carried out under highly controlled conditions other polymers could be used in this context as well. As long as solvents and nonsolvents can be found enabling this precipitation process, the possibilities are countless. Depending on the physicochemical properties of the utilized particle material the manufactured systems can be specifically selected for a drug substance to be delivered. Especially hydrophilic polymers like the already employed gelatin or dextrans are suitable for incorporating large hydrophilic molecules [3–5]. Regarding proteins or nucleic acids showing this hydrophilicity the developed manufacturing procedure represents a platform technology for developing suited drug delivery systems for a vast variety of molecules from these groups.

As an alternative to nanoprecipitation, the improved microfluidic system could be considered for the production of emulsions. Referring to literature, mixing liquids which are not soluble in each other could be processed into precisely planed emulsions by exploiting the precision of the system. With this ability very fine emulsions could result acting as a drug delivery system themselves or could be utilized for particle manufacturing with regard to the solvent evaporation technique [6,7].

6.2 Improvement of drug loading

Quantifying the drug loading of curcumin on PLGA particles revealed that all stabilizers showed a concentration dependent influence on the overall curcumin loading. Although the type of stabilizer was not of importance the molar stabilizer concentration was much more decisive. Stabilizer concentrations below $2 \cdot 10^{-4} \text{ mol L}^{-1}$ showed no larger influence on curcumin loading for most of the stabilizer types. From this information it can be concluded that a changing number of stabilizer molecules on the particle surface does not significantly affect the loading. However, by increasing all molar stabilizer concentrations above a common value of $2 \cdot 10^{-4} \text{ mol L}^{-1}$ the curcumin loading started to decrease significantly. This raises the question if this specific molar concentration represents the stabilizer concentration covering the entire surface of particles with stabilizer molecules. Consequently, a higher stabilizer concentration led to micelle formation in the dispersant and a possible drug incorporation into the micelles. This would explain a decrease in drug loading by increasing the stabilizer concentration.

Information about critical micelle concentrations (CMC) regarding the utilized stabilizers would help to detect a correlation between a sudden micelle formation and a decrease in drug loading. To gain a deeper understanding regarding the process CMC measurements are highly recommended and should be carried out in future works following this investigation.

Furthermore, this loading behavior should be investigated for other model drug substances as well. As curcumin is a highly lipophilic substance, the influence of previously utilized stabilizer molecules is comprehensible. Due to lipophilic molecules tend to be incorporated into the lipophilic cores of micelles (in aqueous media) [8,9] a loading competition between micelles and particles is occurring. This trend must not hold true when hydrophilic drug substances are utilized. It would be worth investigating if formed micelles would show any competition regarding drug loading while using hydrophilic substances. In case an influence on drug loading can be detected a further investigation would be desirable if this behavior is transferable to all utilized stabilizers or just to specific types.

6.3 Particle quantification

Focusing on particle quantification it could be verified that the developed single-particle tracking approach features a highly accurate and sensitive quantification method for fluorescently labelled nanosuspensions. This developed quantification approach is providing information about the number of contained particles especially in highly diluted samples.

In comparison to commercially available particle quantification techniques as MADLS the range for measurements could be extended to much lower concentrations. This extension is ensured by a higher sensitivity of measurements. Furthermore, the single-particle tracking quantification approach shows smaller fluctuations in determined particle numbers compared to MADLS.

Nevertheless, by measuring different diluted samples (originating from the same particle suspension) with MADLS and single-particle tracking both quantification approaches delivered similar results for the stock suspension after recalculating respective dilution factors. Additionally, using a gravimetric concentration analysis investigating the original suspension the measured average particle concentration (obtained by single-particle tracking and MADLS) could be verified.

By further comparing the developed single-particle tracking based quantification approach to methods like tunable resistive pulse sensing (TRPS) or nanoparticle tracking analysis (NTA) the benefit of quantifying particles in high precision in extremely low concentrations stands out. Comparing NTA and TRPS directly to single-particle tracking it becomes clear that NTA is not able to determine the lowest particle concentrations obtained by single-particle tracking as mentioned previously, and TRPS is more challenging in terms of sample preparation and analysis. The manufacturing of the utilized microfluidic devices is cost-efficient and easy. Also, an arbitrary fluorescent microscope is simple to equip with the developed device for extending its capabilities regarding particle quantification.

However, the previously shown setup was not capable of capturing nanoparticles (~110 nm) by just relying on light scattering and excluding fluorescence detection. The

scattering originated from the developed microfluidic counting device was too high in intensity while particle scattering was too low. Nevertheless, a possible quantification relying on light scattering would be highly desirable especially for particles lacking fluorescence activity. By facilitating a particle detection based on light scattering a preceding fluorescence labeling could be skipped. For detecting the weak scattering signal of such small particles, the scattering of the quantification device must be reduced to a minimum. Aiming for a reliable single-particle tracking-based quantification approach a quantification device providing identical channel dimensions but consisting of an alternative material would be desirable. Glass could be a suitable material for this purpose. Microscopic cracks and scratches in the previously used PDMS based device, which scatter large amounts of light, could be avoided utilizing glass. By refining the quantification device with an alternative material, the single-particle tracking based quantification could be transferred to light scattering as a particle detection method finally enabling the quantification of non-fluorescent nanoparticles.

6.4 References

- [1] T. Gulick, Transfection Using DEAE-Dextran, *Curr Protoc Mol Biol.* 40 (2001) 9.2.1-9.2.10. <https://doi.org/10.1002/0471142727.MB0902S40>.
- [2] C. Siewert, H. Haas, T. Nawroth, A. Ziller, S.S. Nogueira, M.A. Schroer, C.E. Blanchet, D.I. Svergun, A. Radulescu, F. Bates, Y. Huesemann, M.P. Radsak, U. Sahin, P. Langguth, Investigation of charge ratio variation in mRNA – DEAE-dextran polyplex delivery systems, *Biomaterials.* 192 (2019) 612–620. <https://doi.org/10.1016/J.BIOMATERIALS.2018.10.020>.
- [3] N. Sahoo, R.K. Sahoo, N. Biswas, A. Guha, K. Kuotsu, Recent advancement of gelatin nanoparticles in drug and vaccine delivery, *Int J Biol Macromol.* 81 (2015) 317–331. <https://doi.org/10.1016/J.IJBIOMAC.2015.08.006>.
- [4] Q. Hu, Y. Lu, Y. Luo, Recent advances in dextran-based drug delivery systems: From fabrication strategies to applications, *Carbohydr Polym.* 264 (2021) 117999. <https://doi.org/10.1016/J.CARBPOL.2021.117999>.
- [5] S. Jamwal, B. Ram, S. Ranote, R. Dharela, G.S. Chauhan, New glucose oxidase-immobilized stimuli-responsive dextran nanoparticles for insulin delivery, *Int J Biol Macromol.* 123 (2019) 968–978. <https://doi.org/10.1016/J.IJBIOMAC.2018.11.147>.
- [6] M. G. Nava-Arzaluz, E. Pinon-Segundo, A. Ganem-Rondero, D. Lechuga-Ballesteros, Single Emulsion-Solvent Evaporation Technique and Modifications for the Preparation of Pharmaceutical Polymeric Nanoparticles, *Recent Pat Drug Deliv Formul.* 6 (2012) 209–223. <https://doi.org/10.2174/187221112802652633>.
- [7] K. Kizilbey, Optimization of Rutin-Loaded PLGA Nanoparticles Synthesized by Single-Emulsion Solvent Evaporation Method, *ACS Omega.* 4 (2019) 555–562. <https://doi.org/10.1021/ACSOMEGA.8B02767>.
- [8] M.S. Haider, M.M. Lübtow, S. Endres, S. Forster, V.J. Flegler, B. Böttcher, V. Aseyev, A.C. Pöppler, R. Luxenhofer, Think beyond the Core: Impact of the Hydrophilic Corona on Drug Solubilization Using Polymer Micelles, *ACS Appl Mater Interfaces.* 12 (2020) 24531–24543. <https://doi.org/10.1021/ACSAMI.9B22495>.

- [9] A. Fahr, Voigt Pharmazeutische Technologie, Voigt Pharmazeutische Technologie. (2022).
<https://doi.org/10.52777/9783769277487>.

Publication report

Research paper:

“A precise nanoparticle quantification approach using microfluidics and single-particle tracking” by Johannes Buescher, Thomas John, Anna K. Boehm, Louis Weber, Salma M. Abdel-Hafez, Christian Wagner, Tobias Kraus, Markus Gallei, and Marc Schneider.

The manuscript was submitted to *Journal of Drug Delivery Science and Technology*
<https://doi.org/10.1016/j.jddst.2022.103579>

Book chapter:

“PLGA-based nanoparticles for treatment of infectious diseases” by Johannes Buescher*, Armin Walter Novak*, Saeed Ahmed Khan, Agnes-Valencia Weiss, Sangeun Lee, and Marc Schneider in “Poly(lactic-co-glycolic acid) (PLGA) Nanoparticles for Drug Delivery”, Elsevier, edited by Prashant Kersharwani.

(*shared first authorship)

<https://doi.org/10.1016/B978-0-323-91215-0.00014-5>

Poster:

“Layer-by-Layer Stabilization of Cylindrical Microparticles Using DNA” by Michael Möhwald, Marcel Poursghar, Johannes Büscher, and Marc Schneider.

DPhG Annual Meeting, October 2016, Munich, Germany

“Preparation and Characterization of PLGA Nanoparticles in low Numbers” by Johannes Büscher, Thomas John, and Marc Schneider.

CRS 24th Annual Meeting, February 2020, Munich, Germany

“Preparation and Characterization of PLGA Nanoparticles in low Numbers” by Johannes Büscher, Thomas John, and Marc Schneider.

DPhG Annual Meeting, September 2021, remote

“Amplification of exogenous RNA trigger by RNA dependent RNA polymerases” by Marcello Pirritano, Johannes Büscher, Kristela Shehu, Gilles Gasparoni, Marc Schneider, and Martin Simon.

ECOP-ISOP Joint Meeting, July 2023, Vienna

Acknowledgements

First of all, I want to thank my doctoral father Prof. Dr. Marc Schneider for giving me the opportunity to work on this project in his research group and to finalize my work in this thesis. Thank you very much, Marc, for your support, your ideas, and your time to make this possible. Thanks as well, for the nice and funny talks about soccer, Star Trek, and fantasy literature. Serving with you has been an honor, captain!

As well, I want to thank Prof. Dr. Tobias Kraus for taking over the scientific participation in this project. Thank you very much for all the good ideas and contributions to this work resulting in a fantastic collaboration making many positive outcomes possible.

Furthermore, I want to express my huge gratefulness to Dr. Thomas John. Dear Thomas, without you this project would never have turned out as positive as this, and I am so glad that we both met at the right time. Thank you very much for your inspiring ideas, your never-ending support, and your huge contribution in terms of *in silico* data analysis. Thanks for giving the quantification part of the project a solid base to stand on.

Microfluidics in the way they were performed, would not have been possible without the expertise of Oliver Brieger. Dear Olli, what a fantastic coincidence to meet someone like you by chance on an excursion. Thank you so much for being such a good friend to me. Thanks as well for all the “Herrenabende” together with great discussions about life and other important things. And in addition to that, thank you for your scientific contribution to the microfluidic setup. You are a real friend everyone deserves in one’s life!

I want to thank Anna Boehm and Louis Weber for their support in evaluating the particle quantification process. Dear Anna and Louis, thank you both so much for your help by providing nanosuspensions and performing density measurements. It may be just a small expense for you, but for me your help was priceless.

To all my colleagues from AG Schneider, thank you for the fantastic time together. Thank you for all the great memories, which I will keep forever. Also, you were a great support in bad times, which means a lot to me. At this point I want to highlight Alex, Karola, Tom, and Thorben. I feel blessed to have had a working environment with you all by my side.

Furthermore, I want to thank my masters students and interns. Dear Taha, Lukas, Christof, and Matthias thank you for your fantastic work in the lab and your contribution to this project. Lots of the data you produced helped to create this thesis, and I am very grateful to have had coworkers like you.

Finally, I like to thank my family for their unconditional and never-ending support during my path to this very moment. Dear Mama, Papa, Thes, and Onkel Bernd, thank you for everything.

Curriculum vitae

Personal information Johannes Clemens Büscher
Date of birth: September 12, 1993 in Neuss
Nationality: German
Contact: johannesbuescher1@gmx.de

Doctoral thesis

Jan 2019 – Dec 2022 Institute of Biopharmaceutics and Pharmaceutical
Technology, Department of Pharmacy,
Saarland University, Saarbrücken
Group of Prof. Dr. Marc Schneider

Professional experience

Feb 2021 – present Lecturer at Ravati Seminare GmbH, Augsburg

Jan 2019 – present Pharmacist at Apotheke am Bahnhof, Erkelenz

Professional training

May 2018 – Oct 2018 Pharmaceutical training at Sebastian Apotheke, Nettetal

Nov 2017 – Apr 2018 Pharmaceutical training in the division Formulation
Development pre D3 at Bayer AG, Wuppertal

Sep 2015, Mar 2016,
and Sep 2016 Assistant scientist at Institute of Biopharmaceutics and
Pharmaceutical Technology, Department of Pharmacy,
Saarland University, Saarbrücken
Group of Prof. Dr. Marc Schneider

Educational background

Dec 2018 Licensed pharmacist (Approbation)

Apr 2013 – Oct 2017 Pharmaceutical studies at Philipps-Universität Marburg

Sep 2003 – Jun 2012 Abitur at Erasmus Gymnasium, Grevenbroich